Summer 2019

Morphological Study of Voids in Ultra-Large Models of Amorphous Silicon

Durga Prasad Paudel
University of Southern Mississippi

MORPHOLOGICAL STUDY OF VOIDS IN ULTRA-LARGE MODELS OF AMORPHOUS SILICON

by

Durga Prasad Paudel

A Dissertation
Submitted to the Graduate School,
the College of Arts and Sciences
and the School of Mathematics and Natural Sciences
at The University of Southern Mississippi
in Partial Fulfillment of the Requirements
for the Degree of Doctor of Philosophy

Approved by:

Dr. Parthapratim Biswas, Committee Chair
Dr. Chris Winstead
Dr. Khin Maung Maung
Dr. Ras B. Pandey
Dr. Gopinath Subramanian

Dr. Parthapratim Biswas	Dr. Bernd Schroeder	Dr. Karen S. Coats
Committee Chair	Director of School	Dean of the Graduate School

August 2019

ABSTRACT

The microstructure of voids in pure and hydrogen-rich amorphous silicon (*a*:Si) network was studied in ultra-large models of amorphous silicon, using classical and quantum-mechanical simulations, on the nanometer length scale. The nanostructure, particularly voids of device grade ultra-large models of *a*:Si was studied, in which observed three-dimensional realistic voids were extended using geometrical approach within the experimental limit of void-volume fractions. In device-grade simulated models, the effect of void morphology; size, shape, number density and distribution on simulated scattering intensities in small-angle region were investigated. The evolution of voids on annealing below the crystallization temperature ($\leq$ 800 K) were examined, where the extent of the void reconstruction were reported by using high-quality three-dimensional rendering software and calculating an average size and volume of the voids. Additionally, the role of bonded and non-bonded hydrogens near the vicinity of the void's wall in *a*:Si network was observed. Our simulated results suggested that, in extended void structures, X-ray scattering intensities in the small-angle region were sensitive to the number density, size, shape and the distribution of the voids in unequal strength. In both classical and local *ab initio* molecular dynamics models of *a*:Si, the reconstruction of the voids were observed but in later models, with and without present hydrogen reconstruction effect was observed greater. The distribution and dynamics of bonded and non-bonded hydrogen in heavily hydrogenated ($\geq$ 14 at.%) ultra-large models of *a*:Si suggested that, void's wall were decorated with more silicon dihydride (SiH_2) bonds and 9-13% of the total H were realized as molecular hydrogen (H_2) respectively from 300 K-800 K annealing temperature.This work suggested that, *a*:Si sample with $\geq$ 14 at.% H and $\leq$ 0.2% volume-fraction of voids, may be appropriate for interface hydrogenated amorphous silicon/crystalline silicon (*a*:Si:H/*c*-Si) material used in heterojunction silicon solar cell to obtain the better-passivated surface due to presence of mobile non-bonded hydrogens.

ACKNOWLEDGMENTS

I would sincerely like to thank my advisor and committee chair Prof. Parthapratim Biswas for his continuous guidance, tireless support and excellent mentorship for successful completion of my P.hD. at the University of Southern Mississippi. I would especially like to thank Prof. Chris Winstead who also has remarkable influence on my academic as being my MS research project advisor and Ph.D. dissertation committee member. Also, I would like to thank other committee members Prof. Ras B. Pandey, Prof. Khin Maung Maung and Prof. Gopinath Subramanian, who have provided valuable suggestion and comments for completion of my P.hD. Most importantly, I would like to thank my collaborators Dr. Raymond Atta-Fynn for providing Texas supercomputing facility, Prof. David Drabold and Prof. Stephen Elliott for their continuous feedback and valuable correction of my work.

Also, I would like to extend my acknowledgement to the School of Mathematics and Natural Sciences, all physics faculties and staffs for providing me the opportunity to be a student and pursue my graduate study in this institution. I would like to thank National Science Foundation for partially funding financial support during my P.hD.

It will not be enough without thanking my beloved parents Lilawoti Paudel (Grandmother), Nanda Lal Paudel (Father) and Ranjti Paudel (Mother) for their moral and financial support, love and care and faith and wishes on me. And, I would also like to thank my brother Dr. Trilochan Paudel for his effort to motivate me in Physics and my spouse Sunita Subedi Paudel for family support, unconditional love and inspiration for working hard. I would like to thank my little son Denish Paudel for his understanding in every situation during P.hD. on his age. Finally, I would like to thank my friend Dil Limbu and his family for their great help during my stay. Finally, I would like to extend my gratitude to my other family members, sisters and brother in law who have always been on my side during my P.hD. journey.

TABLE OF CONTENTS

LIST OF ILLUSTRATIONS

Figure

LIST OF TABLES

Table

LIST OF ABBREVIATIONS

***a*-Si**	-	Amorphous Silicon
***a*-Ge**	-	Amorphous Germanium
SRO	-	Short Range Ordering
LRO	-	Long Range Ordering
DVD	-	Digital Video Versatile Disk
DSC	-	Differential Scanning Calorimetry
ESR	-	Electron Spin Resonance
RDF	-	Radial Distribution Function
***a*-Si:H**	-	Hydrogenated Amorphous Silicon
NMR	-	Nuclear Magnetic Resonance
IR	-	Infrared
PECVD	-	Plasma Enhanced Chemical Vapor Deposition
DB	-	Dangling Bond
FB	-	Floating Bond
MC	-	Monte Carlo
MD	-	Molecular Dynamics
CRN	-	Continuous Random Network
RMC	-	Reverse Monte Carlo
DFT	-	Density Functional Theory
PCF	-	Pair Correlation Function
DOS	-	Density of States
EDOS	-	Electronic Density of States
HWCVD	-	Hot Wire Chemical Vapor Deposition
GD	-	Glow Discharge
LDA	-	Local Density Approximation
GGA	-	General Gradient Approximation
SIESTA	-	Spanish Initiative of Electronic Simulation with Thousands of Atoms
SAXS	-	Small-Angle X-ray Scattering
DZP	-	Double Zeta Polarization
SZ	-	Single Zeta Polarization
Si	-	Silicon
H	-	Hydrogen
SiH	-	Silcon hydride
WWW	-	Wooten, Winer and Weaire
RMS	-	Root Mean Square
FID	-	Free Induction Decay
SEM	-	Scaning Electron Microscopy

Chapter 1

INTRODUCTION

1.1 Amorphous Semiconductors

Amorphous semiconductors are very important electronic materials. They have wide range of industrial applications such as solar cells, thin-film transistors, light sensors, optical memory devices, electrophoto-graphic devices, X-ray image sensors, optical-fiber amplifiers, etc [4–7]. They are divided into three groups: (i) covalent amorphous semiconductors, such as amorphous; silicon (*a*-Si), germanium (*a*-Ge), indium antimonide (*a*-InSb) and Galium Arsenide (*a*-GaAs), (ii) chalcogenide glasses such as germanium-antimony-tellurium (GeSbTe) and Silver-Indium-Antimony-Tellurium (AsGeSeTe), oxide glasses such as vanadium glass (V_2O_5–P_2O_5) and (iii) dielectric films such as silicon oxide (SiO_x), Aluminium oxide (Al_2O_3) and Silicon nitride (Si_3N_4). Particularly, hydrogenated amorphous silicon *a*-Si:H is used in solar cells, thin-film transistors and X-ray image sensors, and chalcogenide glasses for optical memory devices, including digital video-versatile disk (DVD). They posses mainly two types of disorders; compositional and topological disorders. The topological disorder is characterized by missing of close-pack atoms and long-range ordering [8, 9]. In covalent amorphous semiconductors, atoms are bonded covalently and correlation can be extend up to the third or fourth nearest neighbors such that in the atomic scale, they are not a completely disordered. Amorphous-nanocrystalinity may also exist [10] in the system. Thus, a especial feature of the covalent amorphous semiconductors is the presence of short-range order (SRO) and the absence of long-range oder (LRO) [5, 11].

Pure crystalline and amorphous semiconductors are different in terms of their their X-ray diffraction patters and melting or glass transition temperature. Pure crystalline semiconductors have well defined melting temperature where as missing of regular atomic ordering in amorphous semiconductors, they exhibit a glass transition temperature. The X-ray diffraction patterns; the board and diffuse holes are observed in amorphous semiconductors but the sharp Braggs spot and rings are observed in the single and poly-crystals. To distinguish whether a sample is a amorphous or microcrystalline or nanocrystalline, X-ray diffraction experiment only is not sufficient. Differential Scanning Calorimetry (DSC) measure the melting temperature and glass transition temperature which distinguishes the sample whether it is amorphous or crystalline [12]. The amorphous and microcrystalline semiconductor

has a fundamental difference which is, crystallization of amorphous semiconductor occurs by means of nucleation and growth of crystallites whereas microcrystalline semiconductor experience overall grain growth of crystallites [13].

There are two major techniques to prepare amorphous semiconductors experimentally [14, 15] and they are (i) cooling from the melt (rapid quenching) and (ii) deposition on the substrate. But theoretically, it is comparatively difficult to prepare amorphous semiconductors [16, 17]. Some of the amorphous semiconductors, e.g., chalcogenide glasses are prepared by rapid cooling (quenching) to a temperature below the glass transition temperature but some semiconductors like Si and group IV cannot be done by this approach. Those amorphous semiconductors which cannot be prepared directly from the melt-quench are usually fabricated in the form of the thin films by deposition procedures such as evaporation, sputtering, chemical vapor deposition, plasma decomposition of gases electroplating, ion bombardment, etc.

In Amorphous semiconductors, topological disorder arises due to fluctuations in the bond lengths, bond angles, and dihedral angles which enhance the missing of atoms from the network. which is called structural defect such that tail states in the band gap region below the edge of the conduction band and above the edge of the valence band appeared [18]. The valence and conduction band edges are called mobility edge, which acts as the boundaries caused by disorder between delocalized and localized states [9], and such boundaries are called Anderson localization. Due to the absence translational symmetry in amorphous semiconductors, the Bloch theory is not applicable, but the tight-binding model, the Hartree-Fock approximation and the density functional method can be applied to understand the electronic properties of amorphous semiconductors.

The desirable and measurable quantities like optical absorption edges, activated electrical conductivities are directly affected by the short-range ordering (SRO) in amorphous semiconductors. The band tail and the structural defect affect the optical properties of amorphous semiconductors [9]. The electronic structure of these localized states can be understood from electron spin resonance (ESR) experiment, where their symmetry is determined from a g-value measurement. However, the principal axes of symmetry are randomly oriented in an amorphous network, and that it makes more difficult to identify defects in amorphous semiconductors than in crystals [19]. Defects in amorphous semiconductors result from a strain-relief mechanism and from bonding misfits during the growth process. They are primarily coordination or bonding defects [20].

Among all covalent amorphous semiconductors, Si is the most popular in technological application because it is abundantly available, easy to fabricate, and it is environmentally friendly. An advantages of *a*-Si over *c*-Si are, (i) Relatively easy to prepare (large area & low

cost), (ii) Amorphous phase can be formed in a wide range of mixed composition such that physical properties of such materials varied continuously simply by varying the composition (ability to grow film over wide areas) and (iii) Amorphous material has a wide range of intrinsic optical properties (optical band gap). As compared to crystalline materials, only a few fundamental physics aspects of amorphous materials are studied and clearly understood. Growing industrial applications attracted material research community to investigate the micro and nanostructure of amorphous semiconductors.

1.2 Amorphous Silicon

Atoms in *a*-Si are very likely to have 4 nearest neighbors, any deviation from the optimal coordination would cause a large increase in the total energy which we called defects. The density of the *a*-Si at room temperature is $1.8\pm0.1\%$ lesser than the *c*-Si [21]. In ideal *a*-Si in reality, there are under coordinated (isolated, two folded, three folded) and over coordinated (five folded) Si atoms. Three fold coordinated silicon atoms are called dangling bonds where as five fold coordinated Si atoms are called floating bonds. Defects in amorphous semiconductors arise from bonding misfits during the growth process [22]. The key defect in *a*-Si are the dangling-bond, which are detected in the experiment electron spin resonance (ESR) measurement and simulations [23–25]. Under coordinated defects (dangling bonds) are the origin of the ESR signal and paramagnetic defects are due to the over coordinated defects (floating bonds) [26].

Defects in *a*-Si in the static network are broadly characterized as geometrical defects and electronic defects. Geometrical defects are defined in terms of the coordination and bond order whereas the electronic defects are defined as a structural irregularity that produces sufficiently localized electronic eigenstates. Missing of single Si atom in the network is called mono-vacancy and that of two bonded Si atoms is called divacancy. Collection of such vacancies form an empty region covered with different members rings. An extended vacancy or defects owing larger member rings are called void.The boarded first few peaks in radial distribution function (RDF) and disappearing of later peaks as observed in crystals and smoothed and broadened band gap instead of sharp value are the signature of extended defects in *a*-Si.

The structural properties of amorphous semiconductors have been studied by a series of surface science tools and techniques; auger electron spectroscopy (AES), electron stimulated deposition (ESD), ion scattering scattering (ISS), secondary ion mass spectroscopy (SIMS), Rutherford backscattering spectroscopy (RBS), X-ray photoelectron spectroscopy (XPS), scanning tunneling microscopy (STM), ultraviolet photoelectron spectroscopy (UPS), atomic

force microscopy (AFM), X-ray electron and neutron diffraction, transmission electron microscope (TEM) and scanning electron microscope (SEM), extended x-ray absorption fine structure (EXAFS), small-angle X-ray scattering (SAXS), Raman scattering, infrared absorption (IR) and nuclear magnetic resonance (NMR).

1.3 Hydrogenated amorphous Silicon

Defect density in pure *a*-Si are higher than the hydrogenated amorphous silicon *a*-Si:H which deteriorate the desired semiconductor properties such as photoconductivity. By doping H in *a*-Si defect density can be reduced such that photoconductivity is significantly improved [27]. H in *a*-Si:H appeared in different bonding configurations; monohydride (Si:H), dihydride (SiH_2), trihydride (SiH_3) but the majority of bonds appeared in monohydride form. The added H appeared in the isolated and interconnected form. Isolated H passivates the dangling bonds but interconnected H form H clusters where H_2 molecules also can form. H are weakly bound to Si and can diffuse easily across the surface. H bonding configurations are dependent on the deposition conditions and they determine the electronic and optical properties [5] of the material. Infrared absorption measurement provides the Si-H bonding information [28]. Hydrogens are light atoms, so their mobility change significantly with a slight increase in the temperature of the system. At a suitable temperature, with sufficient H, defects can be removed but the perfect matching of the at. % H and suitable deposition temperature is a challenging problem in the experiment. So, the simulation methods are introduced for the study of *a*-Si:H and their properties. There are three vibration modes in *a*-Si:H. They are stretching modes; low stretching mode near (1980-2130) cm^{-1} and high stretching mode near (2060-2160) cm^{-1}, bending scissor mode near (800-900) cm^{-1} and wagging modes near 630 cm^{-1} [29].

The major role of hydrogen in *a*-Si:H was first investigated by Paul's group at Harvard by using sputtered *a*-Si and *a*:Ge in 1960 and they noticed that high defect density in *a*-Si and *a*:Ge were not friendly for electronic devices [5, 30]. While trying to eliminate the defects in *a*-Si:H in 1969, *a*-Si:H was first fabricated by Chittick, Alexander, and Sterling by deposition using silane gas (SiH_4). Before that time there was research on amorphous silicon without hydrogen, which was prepared by sputtering or by thermal evaporation. LeComber and Spear identified that in glow discharge *a*-Si:H good electrical transport properties, high career mobility and strong photoconductivity in 1974 resulting from low defect density [31]. The Harvard group demonstrated that the hydrogen concentration in the films was about 10 at. %, by observing its characteristic IR vibration, which has a frequency close to 2000 cm^{-1} for Si-H bonds and 1800 cm^{-1} for Ge-H bonds. At that time it was identified that,

sputtering methods for preparing *a*-Si:H was superior than glow discharge method in terms of material quality.

Application of *a*-Si:H in photovoltaic device technology was started in 1976 by Carlson and Wronski [32,33] at Root Cause Analysis (RCA) laboratory which was 2-3 % conversion efficiency. RCA group continued that research and able to grow efficiency up to 12-14% in 1989 but Japanese company Sanyo was the first company to introduce solar cell in the market in 1979. Board electronic device applications were started after 1981 and in the market, more than 10^6 individual devices are in use nowadays.

Now a days, it is well known that, hydrogenation can reduce the density of dangling bonds to 10^{15}-10^{16} cm^{-3}, in *a*-Si which is appropriate for a device applications but the distribution of H near the vicinity of extended vacancies and their role for micro and nanostructure of voids are still unknown.

1.4 Vacancies and Voids

Vacancies in *a*-Si are defined based on the number of missing atoms. Missing of one atom in the network creates mono-vacancy and that of two atoms create divacancy [29]. Once, Si atom bonded with other four nearby Si atoms is missed then it creates 4 defects and 4 H are needed to passivate those defects. Such that mono- vacancy is surrounded by four silicon mono-hydrides. Divacancy is surrounded by six silicon monohydrides. In the network, if the distance between two missing Si atoms lies in the Si-Si bond length, ≤ 2.8 Å the divacancy is stable otherwise it is unstable. The unstable divacancy can be split into mono-vacancies or converted to other stable divacancies [34]. Presence of vacancies and voids in pure and hydrogenated amorphous silicon is the characteristic properties in microscopic scale [29] which depends on the concentration of H. At low concentration micro-structures are dominated by mono-vacancies and divacancies and at high concentration they are dominated by voids. Voids are defined as the accumulation of multi-vacancy in amorphous network. A cartoon representation of the void is shown in Fig. 1.1. where over coordinated Si atoms are represented by green color and under coordinate Si atom are represented by blue, and red colors. At the center of the network, several Si atoms are missing leaving an empty space which is the void. Added H represented with red color bonded with Si at dangling bond site and after hydrogenation, an isolated and interconnected H remains in the network.

Small-angle scattering of neutrons [35,36], electrons [37] and X-rays [38] studies were identified that the larger features of vacancies were nothing other the voids. Experimental studies, SAXS [38–41], Infrared (IR) spectroscopy [29,42,43], Nuclear magnetic resonance (NMR)[44–47] and calorimetric measurements [48, 49] have identified that voids are a

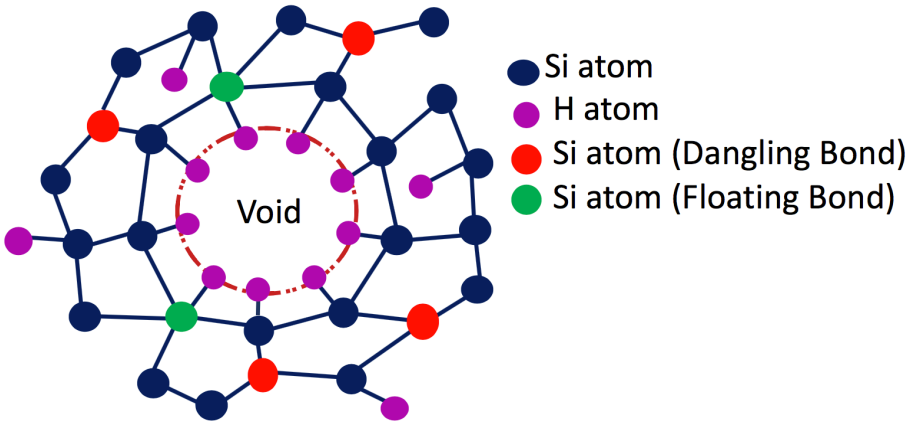

Figure 1.1: A schematic diagram of void in *a*-Si:H.

characteristic feature of the network morphology at high concentrations of hydrogen 14 at.%. Recent studies have shown that in *a*-Si:H nanovoids present even at low concentration of H [50–52] and the size of nanovoids depends on the method of sample preparation [38, 39, 53]. Only in ideal *a*-Si, the void is assumed to be absent but in reality, voids structure exist in pure and hydrogenated amorphous silicon samples which are used in device applications. Electronic and optical properties of materials and hence the device performance are fluctuating because of the fluctuation in the void morphology in *a*-Si and *a*-Si:H.

1.5 Structure of Voids

However, the structure of voids in pure and hydrogenated amorphous silicon has been tried to study by surface techniques mention earlier, only a few of them like small-angle X-ray scattering (SAXS), nuclear magnetic resonance (NMR) and infrared (IR) spectroscopy are sensitive to detect H. To investigate the surface structure of *a*-Si, and *a*-Si:H, non-destructive techniques of surface characterization are required. In situ spectro-ellipsometry analysis suggest that columnar microstructures are developed on the surface of deposited hydrogenated amorphous silicon. The surface texture of *a*-Si:H is dependent of the H content. Mathe *et al.* have shown that surface roughness of *a*-Si:H sample are almost twice greater than that of *a*-Si:H due to the movement of H_2 molecules [54]. In experiments, usually X-ray diffraction (XRD) and scanning electron microscopy (SEM) and atomic force microscopy (AFM) techniques are used to investigate the surface texture and Fourier transform infrared spectroscopy (FTIR) and infrared (IR) spectroscopy is used to measured the hydrogen concentration. Natural voids in the real sample can be appeared on surface also. In laser irradiated *a*-Si:H sample surface voids are observed using SEM [55]. Also,

highly irregular and unequal height and distribution of spikes have observed in *a*-Si:H using atomic force microscopy (AFM) [56].

1.6 Size of Voids

The length scale of the void ranges from the several angstroms to few nanometer. We have an array of experimental studies who have given tentative size of the void ranges from 5 Å to 100 Å. In experimental small-angle X-ray scattering (SAXS) [38, 39, 57] measurement, an estimated typical size of the voids ranges from 5 Å-20 Å where as in NMR [58] measurements it ranges from 20 Å-40 Å. The small-angle neutron (SAN) scattering [53] also reported the size of the void 10 Å-12 Å. Infrared (IR) spectroscopy [59] and calorimetric [48,49,60] studies provide the same measurement up to 40 Å where as Positron-annihilation Spectroscopy (PAS) [61] data suggest their size up to 20 Å. So, there is huge ambiguity in measurement of actual size of nano voids in pure and hydrogenated amorphous silicon. Additionally, the nanostructure evolution around the void due to temperature and H microstructure near the vicinity of void are not quite clear till date. My work, try to resolve the existing shape and size, distribution ambiguity of realistic voids where, simulation of small-angle X-ray scattering and high quality three-dimensional visualization techniques followed by generation of realistic model of pure and hydrogenated amorphous silicon.

1.7 Simulation Study of Voids

It is difficult to control the void shape and size in the experiment but in simulation, we can feature different characteristic properties of void and study their effect on simulated scattering patterns. A comparison of results from simulated models and the real experimental samples leads better understanding the void morphology. In real material, void length scale ranges from 5 Å to 40 Å as described in an earlier section. So, for the study of the voids in *a*-Si and *a*-Si:H, a bigger computer simulated models are essential where comparable length scale voids can be realized.

Basically, there are two broad methods for computer simulation for *a*-Si and *a*-Si:H. They are Monte Carlo (MC) simulation and molecular dynamics (MD) simulation. Additionally, Reverse Monte Carlo (RMC) method also used for computer simulation for *a*-Si which is based on experimental data [62–65]. There are several theoretical studies available in the literature for the model generation of *a*-Si but only two of them [66, 67] have care about the voids morphology in relation with the SAXS intensity patterns. In one [66] there were 500 atoms in MD quench melt model relaxed with Keating potential and in other CRN [67] model there were 4000 atoms generated with Wooten-Winer-Weaire (WWW) bond-

switching algorithm by Barkema and Mousseau [68]. Two major problems (i) finite size effect in scattering intensity at small wavevector region and (ii) not appropriately fitting of the above mention size void in small simulated model require similar theoretical work but in bigger simulated model. Therefore, the objective of my work is to establish high quality ultra-large ($\geq 10^5$) models of *a*-Si, study the morphology of realistic (comparable length scale) voids and the relation between real space observation three-dimensional voids and reciprocal space observation simulated SAXS intensity. Towards the goal, a high quality almost 98% four fold, ultra-large simulated model consisting of 262400 Si atoms generated by classical molecular dynamics simulation using modified Stillinger-Weber inter-atomic potential [69, 70] is established where reasonable length scale void morphology evolution and their signatures in SAXS patterns upon annealing at low and high temperature with and without the presence of H are discussed in the entire work.

The plan of the dissertation is as follows. In chapter 2, I briefly discussed the historical perspective of voids and commonly used experimental and simulation methodologies for the preparation and model generation of *a*-Si and *a*-Si:H. Additionally, a short description of *ab initio* MD, density functional theorem, SAXS procedure and particularly used some formulae are also discussed briefly in this chapter. In chapter 3, the effect of void size, shape, number density and distribution on the simulated scattering intensity in small-angle region are discussed. Effect of low temperature annealing on the nanostructure of void in classical molecular dynamics models are discussed in chapter 4. The evolution of nanovoid at low and high temperature in *ab initio* models, a comparison between the classical model and the role of hydrogen dynamics are discussed in chapter 5.

Chapter 2

BACKGROUND AND METHODS

2.1 Historical Perspective of Voids

Voids in pure and hydrogenated amorphous silicon/germinium are the extended defects and density deficient region owing an empty space. Based on defect density and material quality voids can be isolated and interconnected. Presence of voids obscure the electronic properties of the materials. So, it is essential to identify the the morphology (concentration, size, shape and distribution) of voids before establishing the materials in actual device application. There are several experimental and theoretical studies over the time addressing for the study of voids, which is briefly discussed in early section of this chapter.

The presence of voids in amorphous silicon (*a*-Si) and amorphous germanium (*a*-Ge) was first postulated by Brodsky and Title in 1969 [25] and the crack-like voids were first observed by Terence and Klaus after two years, with the help of High-Resolution Electron Microscope [71]. In 1971, Galeener have studied the effect of internal roughness on the optical absorption and reported that voids in *a*-Ge were ellipsoidal vacuum spaces of various sizes having identical shapes and they could occupy up to 5% volume fraction in the host material [72]. After three years, Shevchik and Paul used experimental small-angle X-ray scattering (SAXS) technique to investigate the size of the voids in *a*-Si and *a*-Ge prepared by sputtering, evaporation and electro-deposition, where they reported that in evaporated *a*-Si and *a*-Ge, the density deficient can be about 4% and 5% respectively and the sizes of the voids were speculated as 5-50 Å [73] based on the spherical radius as suggested by Lecther and Schmidth [74]. Peter D'Antonio *et al.* [38] in 1979 have observed an extensive scattering form *a*-Si:H and they reported the similar distribution of the void in *a*-Si:H as observed in evaporated *a*-Si.

In 1980, Postal *et al.* have used small-angle neutron (SAN) scattering measurement in pure, hydrogenated, and deuterated samples of amorphous silicon *a*-Si:H and reported that the larger area of the voids were covered by hydrogen. They also reported the partial structure factors in wavevector range 0.007-8.75 $Å^{-1}$ [35]. After half a decade Craven *et al.* [37] have reported a small effect of hydrogenation on the void dimension in *a*-Si by small-angle scattering (SAS) measurement. Immediately, in 1986, Chenevas-Paul *et al.* [36] reported the intense SAN Scattering from the *a*-Si and *a*-Si:H. Biswas *et al.* [66]

in 1989 reported that, presence of voids produced strong SAXS patterns in small-angle region and lowered the vibrational density of states in *a*-Si. In the same year, Mahan *et al.* [40] have used SAXS study and showed that the presence of micro-voids in device-quality *a*-Si:H where the volume fraction of microvoids was found to be dependent on the substrate temperature. Also, by doing tilting SAXS experiment, Mahan *et al.* [40] have reported that microvoids in *a*-SiC:H was non-oriented or spherical and oriented or columnar in non-device quality *a*-Si:H. Williamson *et al.* [57] in the same time, studied device-quality glow discharge deposited *a*-Si:H by using SAXS and reported that interior surface of microvoids contain 4-9 bonded H atoms in cluster form.

In 1992, Muramatsu *et al.* [39] have studied *a*-Si:H, *a*-Ge and *a*-$Si_{1-x}Ge_x$:H alloy prepared from plasma enhance chemical vapor deposition (PCVD) method using SAXS and concluded that the scattering characteristics are related to the deposition and composition condition. After two years, the same group have measured the size of microvoids 50 $Å^3$ and 60 $Å^3$ in *a*-Si:H and *a*-SiGe:H alloy by positron-annihilation spectroscopy (PAS) method [75]. Again, in 1995, Williamson *et al.* [76] have studied as-implanted and thermally annealed *a*-Si and reported that scattering signals decreased on increasing annealing temperature, where they also introduced nanostructural information of *a*-Si by arguing that 1.8% lower density of *a*-Si compared to *c*-Si was not from the presence of the void.

Zou *et al.* [77] in 2000, have studied *a*-Si again using PAS measurement and reported that trapped H inside the void or vacancy become mobile in the network with the exposure of light [77]. Beyer in 2004 [78], have reported that void-related microstructures in *a*-Si:H depended on deposition, substrate temperature, annealing, doping, and alloying methods *a*-Si:H. In their work, an isolated void was observed in radio-frequency (RF) plasma-grown *a*-Si:H sample. After five years, Chakrabarty and Drabold have studied structure and dynamics of voids in simulated *ab initio a*-Si model where the dynamics of diffusive H were discussed [79].

Beyer *et al.* [80] in 2012, have reported the the distribution of voids where they observed interconnected voids at $\geq$ 15 at.% H. In the same work, the density of isolated void in plasma-grown and in hot-wire grown device-quality *a*-Si:H were estimated as 10^{18} cm^{-3} and and 10^{21} cm^{-3} respectively. Biwas *et al.* [81] in 2014, have observed theoretically highly irregular voids in simulated *a*-Si:H with 16% -18% at. H and they have reported the formation of molecular H inside the microvoids [81]. The same group after a year have reported the distribution of H in device quality model of *a*-Si:H and they also have observed theoretically 3-4 at.% of total H are distributed in isolated phase [82]. Sekimoto *et al.* [83] in 2016, have reported that the non bonded H in *a*-Si:H change the vacancy size distribution and small vacancies changes to nanovoids. Back in two years P. Biswas *et al.* [84] have

reported the number density of microvoids as a function of H concentration. In 2018, Paudel *et al.* [85] have studied the effect of shape, size, number density and distribution of voids in simulated SAXS patterns in ultra-large model of *a*-Si. Again, Sekimoto *et al.* [86] in 2018, have shown the dense restructuring vacancies by non-bonded H and their consequences on measurement of optical band gap. Recently, Beyer *et al.* [87] have measured the the hydrogen diffusion length by using laser scanning technique for annealed *a*-Si:H which is very helpful in my work to estimate the effect non-bonded and diffusing H in nanostructure evolution in pure and H rich *a*-Si.

However, void related microstructures in *a*-Si and *a*-Si:H have studied since 1969, there are few counts of experimental and theoretical works addressing the voids morphology. In our work, we have try to explore some hidden information of voids like shape reconstruction. To the end, the shape parameter sphericity Φ_s is evaluated to explain the degree of reconstruction via annealing samples and methods of simulation.

2.2 Experimental Sample Preparation

Pure and hydrogenated amorphous silicon model can be simulate and prepare experimentally. The general preparation of *a*-Si:H involve non-equilibrium processes such that their properties depend on the method of preparation [5]. Common experimental methods are; sputtering, quenching, annealing, as-implantation, chemical vapor deposition (CVD) and plasma enhance chemical vapor deposition (PECVD). To characterize the structure of the experimental sample, X-ray scattering [40] and neutron diffraction [88] methods are generally used. NMR [44, 89] and IR experimental [42, 90–92] methods are used for Si-H bonding configurations. This work is theoretical and computational, so the entire work is based on computer generated model.

2.3 Computer Model Generation

Experimental methods mention in above paragraph for the characterization of structural aspects of pure and hydrogenated amorphous silicon are not quite enough, so the computer simulation and modeling of *a*-Si and *a*-Si:H are essential where a comparison of the simulated results with the experimental results leads to a better understanding of the nanostructure in *a*-Si and *a*-Si:H. Initially, the structure of *a*-Si was believed to be continuous random network (CRN). Polk[93] in 1971, built first CRN model of *a*-Si by hand but nowadays models are generated on computer. Wooten, Winer and Weaire [94] in 1984, first developed a computer algorithm (bond transpositions) and applied to generate a realistic model of *a*-Si where radial distribution function (RDF) was in good agreement with the experiment.

Computer simulations for *a*-Si model generation are divided into two board methods. They are stochastic and deterministic methods, where two powerful computer simulations Monte Carlo (MC) and molecular dynamics (MD) are well established for many-body systems. In MC methods, the best model is considered the lowest energy configuration which used to search by displacing atomic positions, changing bond angles and bond length, etc. On searching minimum energy configuration, an empirical or semi-empirical potential like Keating [95], Stillinger-Weber [69] and Tersoff [96] etc are often used. Improve WWW algorithm by Barkema and Mousseau is capable of producing amorphous silicon model [68], which is considered as high-quality model. For very large model of *a*-Si WWW algorithm is not well suited because because of high computation cost for energy and force calculations associated with the purposed bond transposition. Therefore, alternative method or model generations scheme with different interaction potentials are in used.

2.4 Molecular Dynamics Simulation

In molecular dynamics (MD) simulation, the potential energy or interaction model is essential. Initial guess position and velocity of atoms are updated by using a finite difference scheme, where Newton's equation of motion are integrated for all atoms and force is derived from potential energy [97]. Generally the total simulation time of 10 ps to 1μs are used depending upon the model. The sequence of the MD move are collected in phase space where the trajectory can be drawn as a function of time. Time average and other properties are calculated from the trajectory. Thermodynamic quantities like pressure, temperature or the number of particles are controlled by choosing the statistical ensemble usually microcanonical (NVE) and canonical (NVT) in some cases. For the study of voids in a large simulated model of *a*-Si we have used classical MD simulations in a canonical ensemble where trajectory of atom are determined by integrating the equation of motion using the velocity Verlet algorithm. The interaction potential used is the modified Stillinger-Weber potential.

2.4.1 Stillinger-Weber Potential

For system of N identical atom total interaction is the sum of all possible interactions. In *a*-Si there is no long-range order. So, Modified Stillinger-Weber (SW) potential is estimated by considering the pair-interaction term (two-body and three-body) as[69, 98],

$$\phi(1,.....,N) = \sum_{i<j} v_2(i,j) + \sum_{i<j<k} v_3(i,j,k) \tag{2.1}$$

where,

$$\begin{cases} v_2(r_{ij}) = \varepsilon f_2(r_{ij}/\sigma) \\ v_3(\boldsymbol{r}_i, \boldsymbol{r}_i, \boldsymbol{r}_i) = \varepsilon f_3(\boldsymbol{r}_i/\sigma, \boldsymbol{r}_j/\sigma, \boldsymbol{r}_k/\sigma) \end{cases} \tag{2.2}$$

In the above equation, ε and σ are chosen to have f_2 (depth) value -1 and minimum at $r = |\boldsymbol{r}_i - \boldsymbol{r}_j| = 2^{1/6}$. Functions, f_2 and f_3 are defined as,

$$\begin{cases} f_2(r) = A(Br^{-p} - r^{-q}) \exp[\delta/(r-b)], r < b \\ f_2(r) = 0, r >= b \end{cases} \tag{2.3}$$

and

$$f_3(\boldsymbol{r}_i, \boldsymbol{r}_j, \boldsymbol{r}_k) = h(r_{ij}, r_{jk}, \theta_{jik}) + h(r_{ji}, r_{jk}, \theta_{ijk}) + h(r_{ki}, r_{kj}, \theta_{ikj}) \tag{2.4}$$

where,

θ_{ijk} is the angle subtended by $\boldsymbol{r}_{ij}$ and $\boldsymbol{r}_{ik}$ at vertex i. And,

$$h(r_{ij}, r_{jk}, \theta_{jik}) = \lambda \exp[\gamma(r_{ij} - b)^{-1} + \gamma(r_{ik} - b)^{-1}] \times [\cos\theta_{jik} + \frac{1}{3}]^2, \lambda > 0 \tag{2.5}$$

In the above equations, λ, A, B, p, q, γ, δ are SW parameters. They have different value for Si and Ge. Parameter b (cut off) is chosen between the first and second nearest-neighbor.

2.5 *Ab initio* Molecular Dynamics

The first-principle or *ab initio* MD simulation is based on quantum mechanics, where electronic structures are calculated by solving electronic Schrodinger's equation providing the position of nuclei and the number of electrons. Using *ab initio* method, better quality of *a*-Si model has been simulated [99–102]. A protocol of *ab initio* MD is shown in Fig. 2.1. An *ab initio* MD methods [101, 103] treat both atomic and electronic states of the system self-consistently. Car and Parrinello [104] introduced a powerful *ab initio* MD method which is MD combined with density functional theory (DFT). Their approach extends beyond usual pair-potential approximation and allows the simulation of the covalently-bonded and metallic system. The results from the first-principle or *ab initio* and DFT methods are very close to the experiments so, they are widely used in simulation research for amorphous silicon [94, 104].

2.6 Density Functional Theory

Density functional theory was first given by Thomas and Fermi and they purposed that the knowledge of electron density $n(\boldsymbol{r})$ is a fundamental variable for the determination

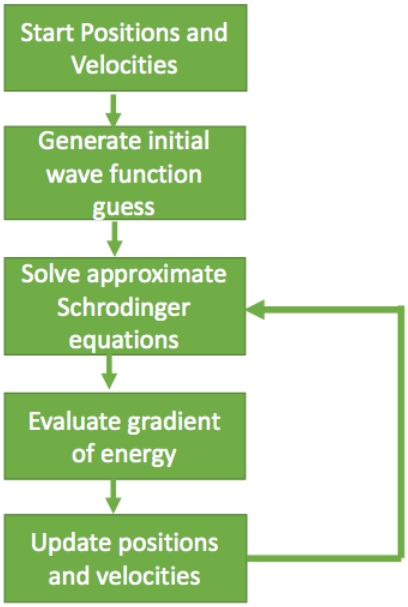

Figure 2.1: Flowchart for *ab initio* MD method.

of the ground state and other properties of the atomic system [105, 106]. The electron-electron interaction energy can be determined from the classical Coulomb potential. Hartree developed a method for calculating the wave function of an atom by introducing the self-consistent field (SCF) approach [107, 108]. Dirac introduced an exchange energy for homogeneous electron gas and recast the Hartree-Fock theory in terms of density function [109]. In SCF approach, the wave function of N-electron system can be written as;

$$\Psi(\boldsymbol{r}_1,\boldsymbol{r}_2,\boldsymbol{r}_3....\boldsymbol{r}_N) = \psi_1(\boldsymbol{r}_1)\psi_2(\boldsymbol{r}_2)\psi_3(\boldsymbol{r}_3)...\psi_N(\boldsymbol{r}_N) \tag{2.6}$$

where, $\psi_i(\boldsymbol{r}_i)$ is the wave function of electron. The ground state density $n(\boldsymbol{r})$ for N atoms is,

$$n(\boldsymbol{r}) = N\int d\boldsymbol{r}_2....d\boldsymbol{r}_N|\Psi(\boldsymbol{r}_1,\boldsymbol{r}_2,\boldsymbol{r}_3....\boldsymbol{r}_N)|^2 \tag{2.7}$$

Hohenberg and Kohn (HK) functional [110] with the electron-electron interaction classical Coulomb potential (V_{ee}) and is the kinetic energy of noninteracting electron gas (T_s) is,

$$F[n(\boldsymbol{r})] =< \Psi|T_s + V_{ee}|\Psi > \tag{2.8}$$

The ground state energy is approximated [111] as,

$$E[n(\boldsymbol{r}),V_{ext}] = \int d\boldsymbol{r}V_{ext}(\boldsymbol{r})n(\boldsymbol{r}) + F[n(\boldsymbol{r})] \tag{2.9}$$

Here, V_{ext} is the external potential of the electron-ion interactions. Kohn and Sham decompose energy functional [110] in terms of exchange correlation energy (E_{xc}).

$$F[n(\boldsymbol{r})] = T_s[n(\boldsymbol{r})] + \frac{e^2}{2}\int\int\frac{n(\boldsymbol{r})n(\boldsymbol{r\prime})}{(\boldsymbol{r}-\boldsymbol{r\prime})}d\boldsymbol{r}d\boldsymbol{r\prime} + E_{xc}[n(\boldsymbol{r})] \tag{2.10}$$

Effective potential

$$V_{eff}(\boldsymbol{r}) = V_{ext}(\boldsymbol{r}) + \int \frac{n(\boldsymbol{r\prime})}{|\boldsymbol{r}-\boldsymbol{r\prime}|} + \frac{\delta E_{xc} n(\boldsymbol{r})}{\delta n(\boldsymbol{r})} \tag{2.11}$$

With the variational principle and Kohn-Sham single-particle orbitals $\phi_i(\boldsymbol{r})$, Schrodinger-like Khon-Sham equation is written as,

$$\left[-\frac{1}{2}\nabla^2 + V_{eff}(\boldsymbol{r})\right]\phi_i(\boldsymbol{r}) = \varepsilon_i \phi_i(\boldsymbol{r}) \tag{2.12}$$

Solving this equation, electronic density of all electronic state are obtained in terms of Khon-Sham orbitals and the occupation numbers f_i as,

$$n(\boldsymbol{r}) = \sum_{i=1}^{N} f_i |\phi_i(\boldsymbol{r})|^2 \tag{2.13}$$

E_{xc} can be calculated using local density approximation (LDA) [110]

$$E_{xc}^{LD} = \int d\boldsymbol{r} n(\boldsymbol{r}) \varepsilon_{xc}[n(\boldsymbol{r})] \tag{2.14}$$

where, $\varepsilon_{xc}[n(\boldsymbol{r})]$ is the exchange and correlation energy per particle. This is a good approximation for almost constant density. For varying density, generalized gradient approximation (GGA) is used which assume $\varepsilon_{xc}[n(\boldsymbol{r})]$ is a function of electron density as well as the gradient of the density at each point [112, 113]. In that case, $E_{xc}^{LD}[n(\boldsymbol{r})] \rightarrow E_{xc}^{LD}[n(\boldsymbol{r}), \nabla n(\boldsymbol{r})]$.

Likewise in the experiment, a realistic simulated model is characterized by calculating radial distribution functions (RDF) [114] or pair correlation functions (PCF) [5], bond angle distribution functions [94], reducible and irreducible ring statistics [115]. Based on the research problem, electronic density of states (EDOS) and vibrational density of states (VDOS) are also calculated for the electronic [116] and vibrational [117, 118] properties of the models respectively. In addition, simulated SAXS patterns are also analyzed for the characterization of the network morphology.

2.7 Characterization of Simulated Models

To characterize the simulated models, we examine the two and three-body correlations. In *a*-Si and *a*-Si:H radial distribution function (RDF) and bond angle distribution provide the two-body and three-body correlation respectively. Generally, RDF and average bond angle and its mean square (RMS) fluctuation are examined for all simulated models before further analysis. Additionally, coordination defect, dihedral angle and ring statistics are also calculate to characterize the simulated models. Characteristic properties of the simulated model include number of atoms, simulation length, density, average bond lengths, average

bond angle and RMS deviation in bond angles. In my work, the primary interest is the characteristic features of the voids, where I used simulated SAXS method to examine the morphology of voids in pure and hydrogenated amorphous silicon.

2.8 Small-Angle X-Ray Scattering Simulation

Small-angle X-ray scattering is a widely used analytical method for the structure of materials in terms of average particle sizes and shapes. SAXS method can be used in solid, liquid and gaseous or any other mixed materials. Generally, the X-ray beam incident on sample in the transmission mode and every particle in the sample sent out its signal such that an average structure of all illuminated particles in the bulk sample is measured. If X-rays incident almost parallel to the surface then scattering signals are in reflection mode, which is variant of SAXS called grazing incident (GI)-SAXS. GI-SAXS measure the average structure and relative positional order on surface. SAXS method is non-destructive and it requires minimal sample preparation. So that its application extended to biological materials, polymers, colloids, chemicals, nanocomposites, disorder materials, metals and minerals research.

In SAXS, X-ray incident with small angle 2θ ranging from 0.1° - 10° on the sample and scatter elastically. The wavelength of X-radiations usually in the order of particle spacing. Advance feature of SAXS is the ability to analyze the internal structure of the disorder systems with random arrangement of density inhomogeneities of colloid size 10^1-10^4 Å. SAXS is better technique as compared to microscopy in terms average representative structure. However, SAXS measurement was started in 1938 after the Guinier work, it is still refining with the advancement in experiment and computer simulation [119–121]. When X-rays incident on atom, they interacts with electrons and and nucleus. But nuclei are 10^3 heavier than electron and as a result nuclear scattering is negligible. If the particles in the sample are all identical in shape and size they are called mono-disperse, otherwise the sample is poly-disperse. If the particles are far away form each other, then it is called dilute sample. In many particle system, diffuse scattering was first implemented by R. Lazzari in simulation [122]. In the entire work, disorder material particularly *a*-Si and *a*-Si:H are used as the sample.

SAXS analysis in the simulation used spherical averaging to produce one or two dimensional structural informations. In SAXS intensity profile, three regions; Guinier, Fourier and Porod are definced based on wavevector ($k = 4\pi sin\theta/\lambda$) range.The SAXS intensity provide the size, shape, and general structure of the sample through direct calculations of the radius of gyration in the Guinier region. The pair distribution function are extracted from indirect

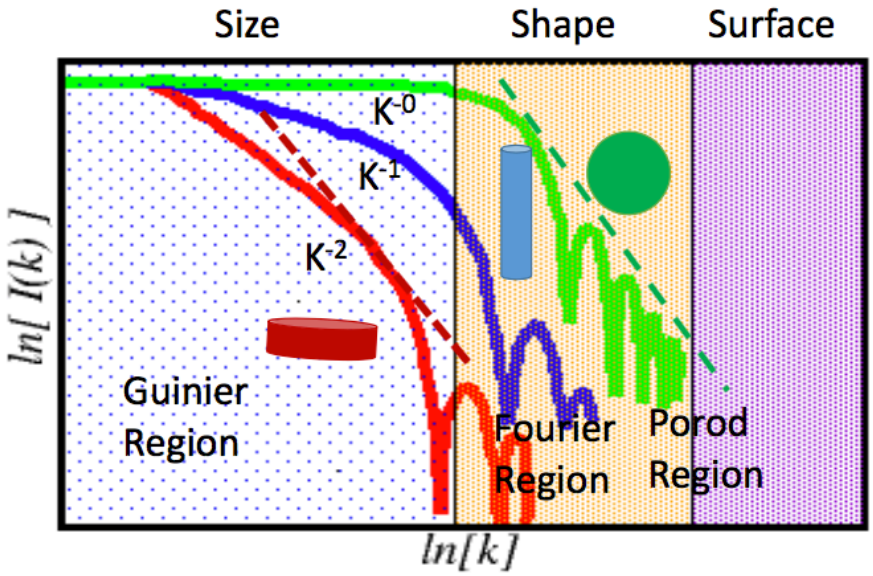

Figure 2.2: Regions in SAXS patterns

Fourier transformation in Fourier region and volume of correlation and the Porod invariant are estimated in the Porod region as shown below. Common SAXS methods are; Debye formula, static structure factor, Cubature formula, Zernike polynomials, multipole expansion, numerical or spherical quadrature, Monte-Carlo sampling and grid or course-grained models of the structure [123, 124]. In my work, SAXS simulation is done based on the static structure factor which involve atomic form factors.

2.8.1 Atomic form factor

Atomic form factor per electron is given by,

$$f_e = \int e^{\frac{2\pi i}{\lambda}(\boldsymbol{k}-\boldsymbol{k}_0).\boldsymbol{kr}} \rho(\boldsymbol{r}) d\boldsymbol{r} \tag{2.15}$$

With the spherical symmetry, above equation simplifies as,

$$f_e = \int_0^\infty 4\pi r^2 \rho(r) \frac{\sin(kr)}{kr} dr \tag{2.16}$$

Then the atomic form factor is the sum of the form factor of all electrons. i.e.

$$f = \sum_n f_{en} = \sum_n \int_0^\infty 4\pi r^2 \rho_n(r) \frac{\sin(kr)}{kr} dr \tag{2.17}$$

Here, $\sum_n \int_0^\infty 4\pi r^2 \rho_n(r)$ is the total number of the electron in an atom. The atomic form factor calculation follow the spherically symmetric atom using self-consistent Hartree-Forck

Table 2.1: Cromer-Mann coefficients for Si.

Atom	a_1	a_2	a_3	a_4	b_1	b_2	b_3	b_4	c
Si	6.292	3.035	1.989	1.541	2.439	32.334	0.678	81.694	1.141
H	0.493	0.323	0.14	0.041	10.511	26.126	3.142	57.8	0.003

wave functions calculated by Don and Cromer using 9 fitting suggested parameter [125]. The atomic form factor of each atom at any given scattering angle is written in terms if fitting parameters a_i, b_i and $c$which are listed in table 2.1 below.

$$f(k) = \sum_{i=1}^{4} a_i \exp(-b_i k^2) + c \tag{2.18}$$

The sum of the Cromer-Mann coefficients as k $\rightarrow 0$ is the atomic number of atom.

2.8.2 Scattering Intensity

Scattering intensity for an assembly of atoms in electron unit is written as [126, 127],

$$I = ff^* \tag{2.19}$$

where, $f = \sum_m f_m = \sum_m e^{\frac{2\pi i}{\lambda}(\boldsymbol{k}-\boldsymbol{k}_0).\boldsymbol{r}_m}$ and $f^* = \sum_n f_n = \sum_n e^{\frac{2\pi i}{\lambda}(\boldsymbol{k}-\boldsymbol{k}_0).\boldsymbol{r}_n}$

$$I = \sum_m \sum_n f_m f_n e^{\frac{2\pi i}{\lambda}(\boldsymbol{k}-\boldsymbol{k}_0).\boldsymbol{k}\boldsymbol{r}_{mn}} \tag{2.20}$$

In this equation an exponential term with spherical symmetry gives $\frac{\sin kr_{mn}}{kr_{mn}}$ such that,

$$I(k) = \sum_m \sum_n f_m f_n \frac{\sin(kr_{mn})}{kr_{mn}} \tag{2.21}$$

This Debye formula for scattering intensity. As $kr_{mn} \rightarrow 0$, $\frac{\sin kr_{mn}}{kr_{mn}} \rightarrow 1$. It simplifies as, $I(k) = \sum_m \sum_n f_m f_n$ Assuming the m atoms at the origin, the above equation can be split as,

$$I(k) = \sum_m f^2 + \sum_m \sum_{m \neq n} f^2 \frac{\sin(kr_{mn})}{kr_{mn}} \tag{2.22}$$

Introducing local density ρ_0 and using the spherically symmetric scattering factor above equation can be split as,

$$I(k) = \sum_m f^2 + \sum_m f^2 \int 4\pi r^2 [\rho(r) - \rho_0] \frac{\sin kr}{kr} dr + \sum_m f^2 \int 4\pi r^2 \rho_0 \frac{\sin kr}{kr} dr \tag{2.23}$$

In amorphous network, no long range order exit such that density function $\rho r \to \rho_0$ for large r. Third term is extremely small and can be negligible. So, scattering intensity in medium range order is written as,

$$I(k) = Nf^2[1 + \int_0^\infty 4\pi r^2(\rho(r) - \rho_0)\frac{\sin(kr)}{kr}dr] \tag{2.24}$$

With the definition of radial distribution function $g(r) = \frac{\rho(r)}{\rho_0}$, reduced radial distribution function $G(r)$ defined as,

$$G(r) = 4\pi\rho_0 r[g(r) - 1] \tag{2.25}$$

and structure factor monoatomic system defined as,

$$S(k) = 1 + \int_0^\infty rG(r)\frac{\sin(kr)}{kr}dr \tag{2.26}$$

the scattering intensity is simplified as,

$$\frac{I(k)}{N} = f^2 S(k) \tag{2.27}$$

Above equations 2.19- 2.27 work for the monoatomic system. For diatomic system the scattering intensity is calculated based on the partial structure factors as [126, 127],

$$\frac{I(k)}{N} = f_\alpha^2(x_\alpha x_\beta + x_\alpha^2 S_{\alpha\alpha}(k)) + f_\beta^2(x_\alpha X_\beta + x_\alpha^2 S_{\beta\beta}(k)) + 2f_\alpha f_\beta x_\alpha x_\beta(S_{\alpha\beta}(k) - 1) \tag{2.28}$$

where,

$$S_{\alpha\beta}(k) = 1 + \int_0^\infty rG_{\alpha\beta}(r)\frac{\sin(kr)}{kr}dr \tag{2.29}$$

$x_\alpha = \frac{N_\alpha}{N}$, $x_\beta = \frac{N_\beta}{N}$ are atomic fractions and f_α and f_β are form factors of α and β atoms. Once the scattering intensity is calculated then the average radii of gyration of the inhomogeneities is calculated using Guinier's approximation [119]. The asymptotic behavior of scattering intensity in small wavevector (k).

$$I(k) = I(0)exp(\frac{-k^2 r_g^2}{3}) \tag{2.30}$$

where, r_g is the Guinier radius. In my work, scattering intensity is calculated based on the static structure factor, where the integral is calculated by using Fillon's method [128].

2.8.3 Oscillatory Integral

For an oscillatory function Felon's integration method applied to estimate the accurate integral value. In our static structure factor, the second term contains an oscillatory function

$G(r)$. Felon's method uses every three consecutive polynomials and calculate the integral value. In an interval $[0, r_c]$ with n-value of $G(r)$ there will be $n' = n/2 - 1$ polynomials. For every value of wavevectors k there will be three polynomials jj, $jj+1$ and $jj+2$ such that, integral

$$\int_{jj}^{jj+2} \sin\{k(ii)rG(r)\}dr = h[\alpha(G(2jj)\cos\{k(ii)r(jj)\} - G(2jj+2)\cos\{k(ii)r(2jj+2)\}) + \beta(\frac{1}{2}G(2jj)\sin\{k(ii)r(2jj)\} + \frac{1}{2}G(2jj+2)\sin\{k(ii)r(2jj+2)) + \gamma(G(2jj+1)\sin\{k(ii)r(2jj+1)\})] \tag{2.31}$$

where $h = r_{ii+1} - r_{ii}$ and α, β and γ are defined based on the value of $\theta = hk$. For $\theta < 0.1$

$$\begin{cases} \alpha = \frac{2}{45}\theta^3 - \frac{2}{315}\theta^5 + \frac{2}{4725}\theta^7 \\ \beta = \frac{2}{3} + \frac{2}{15}\theta^2 - \frac{4}{105}\theta^4 + \frac{2}{567}\theta^6 - \frac{4}{22275}\theta^8 \\ \gamma = \frac{4}{3} - \frac{2}{15}\theta^2 + \frac{1}{270}\theta^4 - \frac{1}{11340}\theta^6 + \frac{1}{997920}\theta^8 \end{cases} \tag{2.32}$$

If $\theta > 0.1$ then

$$\begin{cases} \alpha = \frac{1}{\theta} + \frac{1}{\theta^2}\sin\theta\cos\theta - \frac{2}{\theta^3}\sin^2\theta \\ \beta = \frac{2}{\theta^2} + \frac{2}{\theta^2}\cos^2\theta - \frac{4}{\theta^3}\sin\theta\cos\theta \\ \gamma = \frac{4}{\theta^3}\sin\theta - \frac{4}{\theta^2}\cos\theta \end{cases} \tag{2.33}$$

The structure factor and hence scattering intensity in desired k range are obtained by summing all integral value for all k.

Chapter 3

SMALL-ANGLE X-RAY SCATTERING SIMULATION

In this chapter nanostructural inhomogeneities in ultra-large model of amorphous silicon are studied by using simulated small-angle X-ray scattering. The outline of this chapter is as follows. Introduction of the small-angle X-ray scattering and it capability in solid and condensed phase system are discussed in section 3.1. Simulation method for generating high-quality ultra-large model of *a*-Si, characteristic properties, model validation and SAXS analysis methods are discussed in section. 3.2. The effect on simulating SASX patterns due to the morphology; size, shape, concentration and distribution of voids are the key results of this work which are discussed in section 3.3. Finally, the results are summarized in section 3.4. The work presented in this chapter, is elaborated from the published results by Durga Paudel, Raymond Atta-Fynn, David A. Drabold, Stephen R. Elliott and Parthapratim Biswas in *Physical Review B* 97, 184202 (2018).

3.1 Introduction

Small angle x-ray scattering (SAXS) technique has been used in experiment as well as in simulation for perfect ordered, disordered, particularly ordered and randomly oriented systems in material science, molecular biology, biophysics, polymer science in all phases. Importance of SAXS initially identified by Guinier in late 1930s, after that it has been considerably used in probing structural properties of various non-crystalline materials such as nanocomposites, alloys, glasses, ceramics, and polymers [121, 129, 130]. It provides the inner topology and direct structural informations on such systems with inhomogeneities ranging from 10^1-10^4 Å [121,131,132]. So, the SAXS is a well established extensive method for studying extended length scale of structural inhomogeneities in amorphous solids and condense-phase systems. SAXS is particularly useful in identifying low-resolution structural characteristics of disordered and partially-ordered objects in the nanometer (nm) length scale, which is often complemented with the results from X-ray diffraction and NMR measurements [133].

Nowadays, the refinement of SAXS method via advance instruments and the availability sources of high-brilliance X-rays have led to the advancement and emergence of the SAXS as a primary tool in structural biology for the study of an array of biological objects such as

large macromolecules [134], biopolymers, RNA folding [135, 136] multi-domain proteins with flexible linkers [137] and intrinsically disordered proteins [138]. Despite the huge progress and the well-known applications of SAXS in probing structural information on the morphology and compactness of the scattering objects (e.g. macromolecules/proteins in a solution or voids in an amorphous environment), it is impossible to determine the direct three-dimensional structure of scatterers primarily based on the content information of given dataset unless an extra information is available to complement the SAXS data. In SAXS, the distribution of the scatterers in real space produces a rotational averaging of the scattering intensity in the reciprocal space, the missing of directional (or phase) information between the scatterers makes it very difficult to to extract the three-dimensional shape of a mono-disperse scattering objects from one-dimensional scattering intensities. For poly-dispersed objects in bimolecular system, probing structural information is further more acute, so high-resolution X-ray crystallography and NMR data are providing additional information for structure of the constituents or sub-units of the scattering objects in order to form a three-dimensional structural model [139] along with the analysis of SAXS data. There is also a complications arise in interpreting and translating experimental SAXS data from the reciprocal-space to the real-space having the finite size of the collected data set, at some specific points in the reciprocal space. Moore [140] in an authoritative treatment has simplified this problem by introducing an idea based on the sampling theorem of Shannon, which provides an elegent ansatz to extract the full information contained in a given dataset and to estimate the errors (of the parameters) associated with the analysis.

Given the complexity involved in the analysis of experimental SAXS data and the subsequent determination of a three-dimensional model of the scattering objects, a natural approach to address the problem is to study the relationship between the SAXS intensity and the structure of scattering objects by directly simulating the scattering intensity from realistic model configurations, obtained from independent calculations. In the context of studying extended-scale inhomogeneities in non-crystalline solids, namely voids in amorphous silicon (*a*-Si), such an approach would be particularly convenient provided that high-quality structural models of an appropriate size, which are necessary to simulate the scattering intensity in the small-angle region, are available for the intensity calculations.To this end, in this work, we address the macrostructural properties of voids in *a*-Si with particular emphasis on the relationship between the (simulated) intensity from SAXS and the shape, size, density, and the spatial distribution of the voids in amorphous silicon. While the problem has been studied extensively using experimental SAXS data from pure and hydrogenated amorphous silicon, there exist only a few computational studies [66, 67] that have attempted to address the problem using relatively small-size models of *a*-Si. Since

the intensity in the small-angle region of the reciprocal space is connected to the real space through Fourier transformations, one requires a significantly large model to ensure that any structural correlations that originate from the distant atoms are properly incorporated to produce the correct long-wavelength behavior the scattering intensity. Accurate simulations of SAXS were particularly hampered in the past by the lack of appropriately large structural models of *a*-Si, with a linear size of several tens of angstroms, which are necessary for reliable computation of the scattering intensity in the small-angle region. Recently, de Graff and Thorpe [141] have studied the long-wavelength limit of the structure factor of *a*-Si, using a 10^5-atom model, and have examined the behavior of $S(k)$ in the small-angle region. Likewise, Xie *et al.* [1] have reported a high-resolution structure factor of as-implanted and annealed samples of *a*-Si, using transmission X-ray scattering measurements, to examine the degree of hyper-uniformity in *a*-Si by extrapolating the measured structure factor in the infinite-wavelength limit. In work work, we are addressing the behavior of the structure factor in the small-angle region using ultra-large models of *a*-Si containing as high as 2.624×10^5 atoms.

3.2 Computational Methods

3.2.1 Ultra-large model of *a*-Si

The objective of this work is to study the structure of extended-scale inhomogeneities in the nanometer length scale and present their statistical properties by simulating small-angle X-ray scattering. Here, we are primarily interested in small wave vector region in the range of 0–1 Å^{-1}. To study the void or inhomogeneities with a typical linear size (diameter) of $l \approx 10$–20 Å, it requires the appropriate structural models. The corresponding scattering vector $k = 2\pi/l$ lies in the range ≈ 0.6–0.3 Å^{-1}. Towards the goal, we generated two atomistic models M1 and M2 of amorphous silicon, which comprised 262400 Si atoms. The model was generated using classical molecular-dynamics (MD) simulations in the canonical ensemble with the Stillinger-Weber interatomic potential [69, 70]. The MD time step was 1 fs and Nose-Hoover thermostat [142–144] was used to control the simulation temperature. The simulations proceeded as follows. First, the initial random configurations were generated by randomly placing Si atoms in a cubic box at a density of 2.25 g/cm^3. Then, each configurations was equilibrated a temperature of 1800 K for 10 ps. After equilibration at 1800 K, each configuration was cooled to 300 K over a time period of 50 ps. Finally, the total energy of each output configuration at the end of the 300 K dynamics was minimized using the limited-memory BFGS algorithm [145,146] to obtain the equilibrium configuration. We refer to the equilibrium configurations as M-1 and M-2; these configurations were used

for the SAXS simulations and analysis.

3.2.2 Simulation of SAXS intensity of amorphous Silicon

The scattering intensity of *a*-Si depends on the distribution of Si atoms in the system. For the scattering intensity for an ensemble consisting of N Si atoms [Ref. Eq.(2.20)],

$$I(\mathbf{k}) = \sum_{m}^{N}\sum_{n}^{N} f_m(\mathbf{k}) f_n(\mathbf{k}) \exp[i\mathbf{k}.\mathbf{r}_{mn}], \tag{3.1}$$

all individual atom contribute to atomic form factor $f_i(\mathbf{k})$ and the structural information follows from the (position) distribution of the constituent atoms in the system. Here, the wavevector $\mathbf{k}$ is the difference between the scattered ($\mathbf{k}_f$) and incident ($\mathbf{k}_i$) wave vectors, and its magnitude is given by $k = |\mathbf{k}_f - \mathbf{k}_i| = 4\pi \sin\theta/\lambda$, where 2θ and λ are the scattering angle and the wavelength of the incident X-ray radiation (e.g.,1.54 Å for Cu K_α line), respectively. While Eq. (3.1) can be evaluated directly for small systems, it is computationally very demanding and infeasible to compute the intensity for large models with hundreds of thousands of atoms. Since it is necessary to minimize the surface effects by taking into account the periodic boundary conditions, one needs to evaluate the double summation in Eq. (3.1) in order to compute the intensity values. Further, the computation of configurational-average values of the intensity, for a given k, requires averaging over all possible directions of $\mathbf{k}$ over a solid angle of 4π. Finally, using the well-known sampling theorem of Shannon and Weaver [147] Moore has shown in an authoritative work that in order to extract the full information content of SAXS signal, one must compute or measure the scattering intensity at equally spaced points, also known as Shannon channels, k_i such that $\Delta k \leq \pi/l$, where l is maximum linear size of the particles or inhomogeneities dispersed in the system.[140, 148] These considerations lead to the conclusion that for a system with 10^5 atoms, one requires to compute approximately 10^{15} operations in order to obtain the intensity plot from Eq. (3.1). The conventional approach is to carry out the averaging procedure analytically by introducing a pair-correlation function $g(r)$, which is associated with the probability of finding an atom at a distance r, given that there is an atom at $r = 0$. By invoking the assumptions that the system is homogeneous and isotropic, and that the strong peak near k=0, originating from a constant density term, does not provide any structural information and thus can be removed from consideration, one arrives at the same expression as in chapter 2 Eq. (2.27). So the scattering intensity for our mono-dispersed system is,

$$F(k) = \frac{I(k)}{N} = f^2(k)\, S(k), \tag{3.2}$$

where

$$S(k) = 1 + \frac{4\pi\rho_0}{k}\int_0^\infty r(g(r)-1)\sin kr\,dr$$
$$\approx 1 + \int_0^R rG(r)\frac{\sin kr}{kr}dr. \quad (3.3)$$

In Eq. (3.2), we have introduced the reduced distribution function $G(r) = 4\pi\rho_0 r(g(r)-1)$. For computational purposes, it is also necessary to replace the upper limit of the integral by a large but finite cutoff distance R beyond which $(g(r)-1)$ is expected to vanish. The cutoff distance R is generally, but not necessarily, chosen to be the half of the box length for a cubic model of linear size L. Equation (3.2) can be readily employed to compute the structure factor reliably in the wide-angle limit but the difficulty remains for very small values of k. It has been shown by Levashov *et al.*[149], that $g(r)$ converges to unity very slowly and at finite temperature there exists small but intrinsic fluctuations even for a very large value of R. In the small-angle limit, the term $\sin(kr)/kr$ in Eq. (3.3) changes very slowly but the fluctuations in $(g(r)-1)$ grow considerably beyond a certain radial distance R_c due to the presence of r^2 term in the integrand. Thus, R_c must be as large as possible to extract structural information for small k values. It is often convenient to write Eq. (3.3) in two parts by introducing a damping factor $\gamma(r)$ in the region $r > R_c$. The resulting equation now reads,

$$S(k) \approx 1 + \int_0^{R_c} rG(r)\frac{\sin kr}{kr}dr + \int_{R_c}^R \gamma(r)rG(r)\frac{\sin kr}{kr}dr. \quad (3.4)$$

Computational studies on $G(r)$ in a-Si, using large simulated models, indicate that the optimum value of R_c is of the order of 30–40 Å. Beyond this distance, it is difficult to distinguish $g(r)$ from numerical noise and the accuracy of the integral in Eq. (3.3) is found to be affected by the presence of growing oscillations in $rG(r)$. To mitigate the effect of the truncation of the upper limit of the integral at small k values, we have used an exponential damping factor, $\gamma(r) = \exp[-(r-R_c)/\sigma]$, in the region $r > R_c$. Numerical experiments indicate that a choice of R_c = 35–40 Å and σ = 1 Å is appropriate for our models. Since structural information on extended-scale inhomogeneities generally resides beyond the first few neighboring shells, this observation implies that even with very large models one must be careful to interpret the simulated values of the scattering intensity below $k = 2\pi/R_c \approx 0.1$ Å. Once the structure factor is available, the reduced scattering intensity, $F(k)$, can be obtained from Eq. (3.2), where the atomic-form factor can be obtained from the International Tables for Crystallography[150] or from a suitable approximated from of $f(k)$ [151, 152]. At a finite temperature T, the expression for the reduced intensity in Eq. (3.2) is multiplied by the Debye-Waller (DW) factor, $\exp(-2M)$, where $M = (8\pi^2\sin^2\theta/\lambda^2)(u^2/3)$ and $u^2(T)$ is the

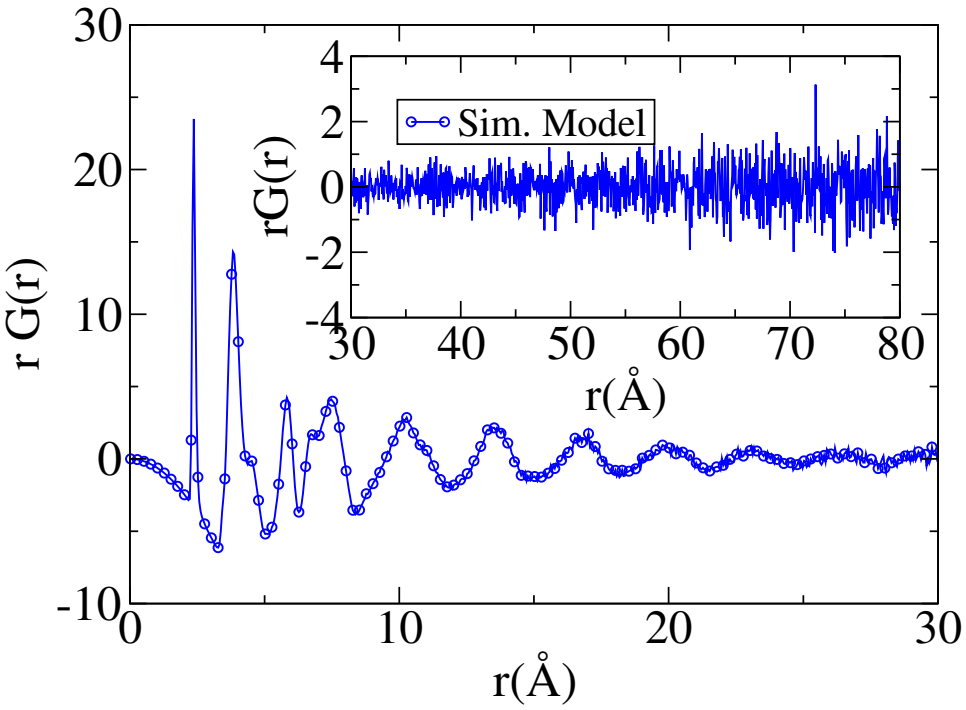

Figure 3.1: The variation of $rG(r)$ with r for M-1 model (262400 atoms) of a-Si. Growing fluctuations in $rG(r)$ beyond 30 Å is shown in inset figure, this fluctuation affect the evaluation of integral in Eq. (3.4).

mean-square displacement of Si atoms in the amorphous state. The Debye-Waller-corrected reduced intensity can be stated as,

$$F_{DW}(k,T) = \exp(-2M)\,F(k). \tag{3.5}$$

The calculation of the Debye-Waller factor for the amorphous state is by itself an interesting problem and it is related to the vibrational dynamics of the atoms at a given temperature. The factor plays an important role in extracting structural information from X-ray scattering data by reducing and redistributing the scattering intensity at high temperature. At room temperature, the DW factor affects the intensity values only marginally for small values of k and it can be replaced by unity for computation of scattering intensity in the region $k < 1.0$ Å^{-1}.

3.2.3 Geometry of voids in a-Si for SAXS simulation

In order to examine the relationship between the morphology of voids and the intensity of small-angle X-ray scattering in a-Si, it is necessary to construct a variety of void distributions in a-Si networks, characterized by different shapes, sizes, and number densities of voids. Since experimental data from infrared (IR) [42, 153] nuclear magnetic resonance (NMR)

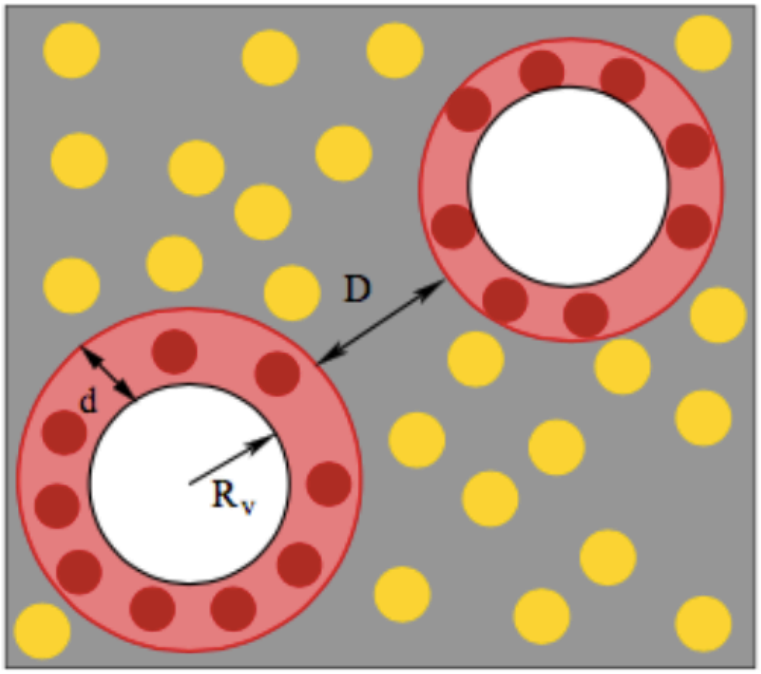

Figure 3.2: A schematic representation of the voids, where the length scales included R_v, d and D are void size, interface width, and the surface to surface distance between two voids respectively.

[46, 58, 89, 154] positron annihilation spectroscopy (PAS) [75, 155, 156] and implanted helium-effusion measurements [78, 80] suggest that the percentage of void-volume fraction (f_v) in a-Si varies from 0.1% to 0.3% of total volume of the samples, and the typical size or radius (R_v) of the voids ranges from 5 Å to 10 Å, we restricted ourselves to generate structural models of a-Si with voids that simultaneously satisfy both the requirement of void-volume fraction and the size of the voids. Toward that end, we have introduced voids with spherical, ellipsoidal, and cylindrical shapes by randomly generating void centers in two model networks, M-1 to M-2, consisting of 262400 Si atoms with a linear size of 176.12 Å.

To ensure that the randomly-generated void distributions in the networks are as realistic as observed in experiments, we have introduced two additional parameters d and D, which define the surface/interface width of the voids and the distance between the outer boundaries of the voids, respectively. This implies that the center-to-center distance, r_{ij}, between two spherical voids at sites i and j satisfies the constraint $r_{ij} \geq 2(R_v + d) + D$. Figure 3.2, shows a schematic representation of two voids in two dimensions illustrating the relevant length scales and the geometry of void construction. The inner and outer radii of the circles correspond to void and void+interface regions with a radius of R_v and $R_v + d$, respectively.

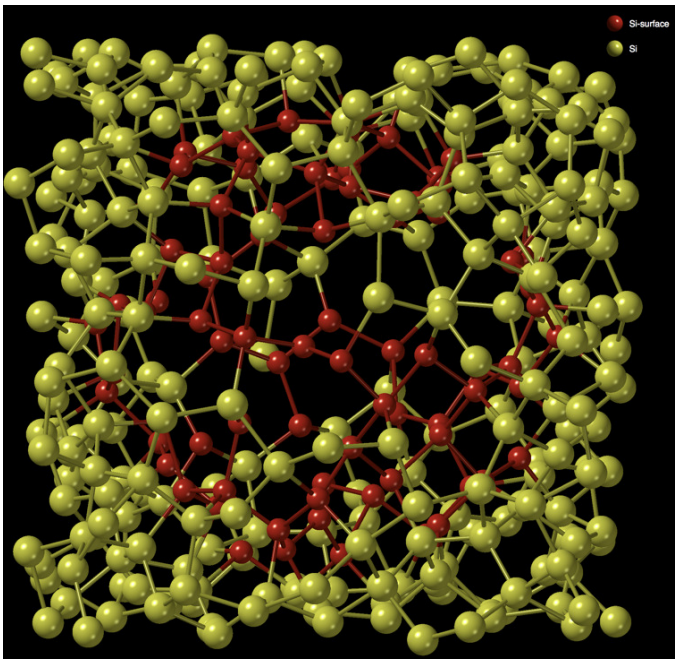

Figure 3.3: Spherical void in a network of size 10 Å, where void radius (R_v) and interface width (d) are 6 Å and 2.8 Å respectively. The bulk and interface region are represented in yellow and red colors respectively.

The outer surface-to-surface distance, D, between the two voids is also shown in Fig.3.2. By choosing appropriate values of f_v, R_v, and D, one can produce a variety of void distributions, which are consistent with experimental results as far as the void volume fraction and the size of the voids are concerned.

For example, by choosing a large (or small) value of D, one can construct a sparse (or interconnected) distribution of voids. The surface or interface width of a void d defines the interface atoms on the void surface. Throughout the study, we have used d = 2.8 Å that corresponds to the maximum nearest-neighbor distance between two silicon atoms in a-Si. For a given set of f_v, R_v, D, and the shape of the voids, one can compute the number of voids $n_v = f_v V/\nu$, where ν and V are the volumes associated with an individual void and the simulation cell, respectively. An example of a spherical void of radius R_v = 6 Å and interface width of $d = 2.8$Å is shown in Fig. 3.3, which is embedded in a region of the network of linear dimension 10 Å.

Table 3.2, lists some characteristic features of voids and the resulting models obtained by incorporating voids of different shapes, sizes, numbers, and void-volume fractions. In order to produce a statistically-significant number of voids for a given volume fraction of voids, the radii of the voids were restricted to 5-8 Å. For f_v = 0.1%, 0.2%, and 0.3%, spherical, ellipsoidal and cylindrical voids of different sizes were generated randomly within

Table 3.1: Characteristic properties of ultra-large model of *a*-Si used in this dissertation. Here L, ρ, c, d_{Si}, θ_{avg}, and $\Delta\theta_{\mathrm{RMS}}$ are simulation box length in Å, mass density in g.cm^{-3}, number density of coordination defect in %, average Si-Si bond length in Å), average bond angle, and root-mean-square deviation in $^\circ$ respectively.

Model	N	L (Å)	ρ (g.cm^{-3})	c	d_{Si} (Å)	θ_{avg}	$\Delta\theta_{\mathrm{rms}}$
M-1	262400	176.12	2.24	2.6	2.39	109.23°	9.26°
M-2	262400	176.12	2.24	2.6	2.39	109.23°	9.20°

the networks in such a way that none of voids was too close to the boundary of the networks.

Ellipsoidal voids were generated by constructing triaxial ellipsoids with the axes ratio $a : b : c = 0.5{:}1{:}2$ so that the geometric mean radius R_v^e $(=(abc)^{\frac{1}{3}}R_v)$ is equal to the radius R_v of a spherical void for a given f_v. For cylindrical voids, the radius of the cylinder was chosen to be the same as R_v but the ratio of radius to cylindrical height was taken to be 1:3. To produce realistic distributions of voids, the orientations of the voids for ellipsoidal and cylindrical cases were generated by constructing a three-dimensional unit random vector from the center of each void. In this work, we have studied a total of 21 models that are indicated in column 1 of Table 3.2. Each of the models is indicated by its shape, size, and the number of voids present in the network. For example, EL6-R6 indicates a model with 6 ellipsoidal voids of radius 6 Å. Similarly, SP6-D12-R6 implies a model with 6 spherical voids of radius 6 Å, which are separated by the surface-to-surface distance of at least 12 Å. The total number of bulk atoms (N_b), surface atoms (N_s), and void atoms (N_v), along with the corresponding void-volume fraction (f_v), number density of voids per cm^3 (n_ρ), and the average radii of gyration (R_g) of the voids for each model after total-energy relaxation are listed in Table 3.2.

3.3 Results and Discussion

For extended length scales structure we rely on the small-angle scattering region of wave vectors $k \leq 1.0$ Å^{-1}. In smaller models as observed by structure is hard to believe in small wave vector region. So, we ultra-large model, where we are calculating structure in small-angle region. This is different than earlier other works where the structure factor are affected by finite-size effects. Because of size of the model high oscillations are appeared in static structure factor at small angle region in reciprocal space and in $rG(r)$ at large r in real space.

Table 3.2: Characteristic properties of *a*-Si models with void distributions used in this work. N_b, N_s, and N_v, f_v, n_ρ, R_g, R, R_{pg} and r_g are, the total number of bulk atoms, surface atoms, void atoms, void-volume fraction, number density, calculated average radius of gyration, actual radius of the void, pseudo-Guinier radius of gyration and Guinier radius of gyration respectively.

Model	N_b	N_v	N_s	f_v%	n_ρ (cm^{-3})	$R_g(R)$ (Å)	$R_{pg}(\mathrm{r}_g)$ (Å)
			Sphere				
SP6-R6	261584	259	557	0.1	0.11×10^{19}	6.13(6.0)	5.3(3.6)
SP3-R8	261634	306	460	0.1	0.05×10^{19}	8.09(8.0)	5.8(5.1)
SP12-R6	260761	533	1106	0.2	0.22×10^{19}	6.13(6.0)	5.3(3.9)
SP5-R8	261126	508	766	0.2	0.09×10^{19}	8.09(8.0)	5.3(4.5)
SP18-R6	259936	801	1663	0.3	0.33×10^{19}	6.13(6.0)	5.3(3.9)
SP8-R8	260371	819	1210	0.3	0.15×10^{19}	8.09(8.0)	5.8(5.9)
			Ellipsoid				
EL6-R6	261491	260	649	0.1	0.11×10^{19}	7.3(6.0)	4.9(3.5)
EL3-R8	261563	302	535	0.1	0.05×10^{19}	9.66(8.0)	5.3(5.0)
EL12-R6	260578	502	1320	0.2	0.22×10^{19}	7.31(6.0)	5.3(3.8)
EL5-R8	261005	513	882	0.2	0.09×10^{19}	9.66(8.0)	5.8(5.1)
EL18-R6	259666	763	1971	0.3	0.33×10^{19}	6.15(6.0)	5.8(4.5)
EL8-R8	260173	825	1402	0.3	0.15×10^{19}	9.66(8.0)	5.8(5.5)
			Cylinder				
CY6-R5	261731	260	409	0.1	0.11×10^{19}	5.83(4.58)	4.6(3.2)
CY3-R6	261752	298	350	0.1	0.05×10^{19}	7.73(6.10)	5.3(4.1)
CY12-R5	261065	511	824	0.2	0.22×10^{19}	5.78(4.58)	5.3(4.9)
CY5-R6	261327	494	579	0.2	0.09×10^{19}	7.74(6.10)	5.8(5.4)
CY18-R4	260389	774	1237	0.3	0.33×10^{19}	5.8(4.58)	5.8(4.9)
CY8-R6	260696	792	912	0.3	0.15×10^{19}	7.75(6.10)	6.3(5.8)
			Disribution				
SP6-D1-R6	261587	256	557	0.1	0.11×10^{19}	6.13(6.0)	5.3(4.6)
SP6-D8-R6	261584	258	558	0.1	0.11×10^{19}	6.13(6.0)	5.3(4.0)
SP6-D14-R6	261588	257	555	0.1	0.11×10^{19}	6.09(6.0)	5.3(3.8)
SP18-D6-R6	259939	790	1671	0.3	0.33×10^{19}	6.13(6.0)	5.3(3.8)
SP18-D12-R6	259948	785	1667	0.3	0.33×10^{19}	6.13(6.0)	5.8(3.6)
SP18-D18-R6	259949	795	1656	0.3	0.33×10^{19}	6.09(6.0)	5.3(3.3)

3.3.1 Structure factor of *a*-Si in the small-angle scattering region

In Table 3.2, we have listed the characteristic structural properties of two models of *a*-Si, M-1 and M-2, as mentioned earlier in section 3.2. Each of the models consists of 262400 atoms in a cubic simulation cell of length 176.12 Å, which translates into an average mass density of 2.24 gram/cm^3. The average bond angle 109.23° between the nearest-neighbor

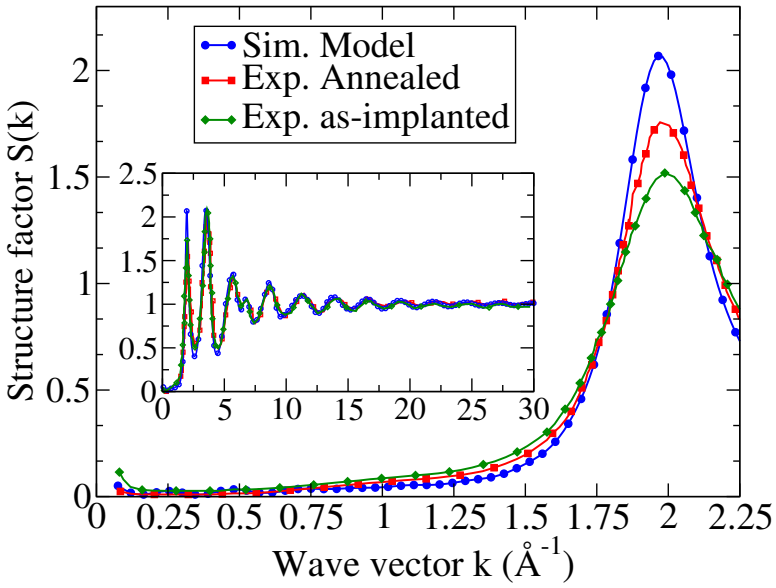

Figure 3.4: The static structure factors of *a*-Si for both experiments [1]; annealed and as-implanted samples and the simulation data. Red and green color curve represent experimental data for annealed and as-implanted samples where as blue curve represent the simulated data. The static structure factors in wide angle region are included in the inset for the wave vector up to 30 Å^{-1}.

atoms is found to be very close to the ideal tetrahedral value of 109.47°, with a root-mean-square deviation of 9.2°. The average Si-Si bond distance is observed to be about 2.39 Å, which is slightly higher (0.8%) than the equilibrium value of 2.37 Å reported from *ab initio* calculations [157]. This observation suggests that the networks have a high degree of tetrahedral character with minimal strain in the system. The number of coordination defects is found to be somewhat higher (2.6%) than the values observed in high-quality WWW[94] or ART [158] models obtained from event-based Monte Carlo simulations. However, the observed defect density is significantly lower than the results obtained from MD simulations, which tend to produce a high density of structural defects in the form of floating and dangling bonds [99, 159]. We will see later in this section that the presence of such additional coordination defects at low density, which are sparsely distributed on the atomistic length scale of 2–3 Å, do not affect the scattering region of interest (i.e., small-angle) in the present study. To address the structural properties of the models, we examine the structure factor ($S(k)$), of *a*-Si in the small-k region. The computed $S(k)$ of simulated ultra-large model of *a*-Si is compare with the same from high-resolution experimental structure-factor data of *a*-Si reported in the literature [3]. Fig.3.4, presents $S(k)$ obtained by averaging the results from two model M-1 and M-2. The corresponding experimental data from as-implanted and annealed samples of *a*-Si, are extracted from Ref.[1]. Here,

following observation are noticed. (a) The simulated structure factor matches very well with the experimental data obtained from the annealed and as-implanted samples for k values up to 30 Å^{-1}, Ref. inset of Fig. 3.4. (b) A careful observation in the vicinity of 1–2 Å^{-1} of the simulated and experimental data revealed that the simulated is closer to the annealed data than to the as-implanted data which is consistent with the expectation that *a*-Si models from MD simulations should be structurally and energetically closer to annealed samples than to as-implanted samples. Annealing of as-implanted samples at low to moderate temperature (400–500 K) reduces the network imperfection locally and thereby improves the local ordering, which typically reflects in the first peak of $S(k)$. (c) In the small-k region, $0.15 \leq k \leq 1$ Å,$^{-1}$ $S(k)$ is quite accurate despite the presence of an artificial damping term in Eq. (3.4) that imposes an effective cutoff length of $R_c + 5\,\sigma$ ($\approx$ 35-40 Å) on the reduced radial distribution function.

However, a direct comparison of the simulated and it counterpart experimental $S(k)$ establishes the effectiveness of the numerical approach and the reliability of the simulated models used in the work, a more precise measurement to examine the accuracy of structure-factor data in the small-k region following the behavior of $S(k)$ in the limit $k = 0$. Graff and Thorpe[160] also recently addressed the this behavior $S(0)$ computationally by analyzing $S(k)$ as $k \to 0$. They reported the $S(0)$ of the order of 0.035 by studying large *a*-Si models containing 10^5 atoms. Similarly, Xie *et al.*[1] reported $S(0) \approx 0.0075$ with the analysis of high-resolution experimental structure-factor data in the small-angle limit. Although a full analysis of the behavior of $S(k)$ near $k = 0$ is outside the scope of the our work, an extrapolation of $S(k)$ at k = 0, by employing a second-degree polynomial in k in the region 0.15-1.0 Å^{-1}, yields a value of 0.0154 ± 0.0017. This value is comparable to the computed [160]/experimental [1] values. It is an impression of the fact that our models produce accurate structure-factor data in the small-angle scattering region than any other simulated models.

3.3.2 Reconstruction of Voids Surfaces

Recent theoretical studies on hydrogenated *a*-Si, using *ab initio* density-functional simulations [81, 82, 84] and experimental data from SAXS [57, 161], IR [40, 153] and helium-effusion measurements [78, 80] indicate that the shape of the voids in *a*-Si:H can be rather complex and that it depends on a number of factors, such as the (a) size, (b) number density, (c) the volume fraction of voids, and (d) the method of preparation and conditions of the samples/models.

Experimental methods can provide considerable structural information on voids, it is

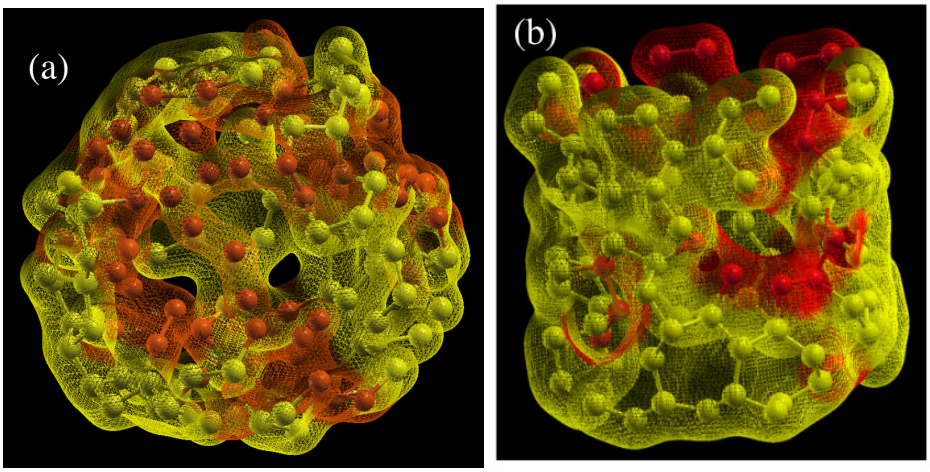

Figure 3.5: Reconstruction of a void surfaces after total-energy relaxation in (a) SP18-R6 model and (b) CY8-R6 model. The void surface are drawn with surface atoms lying in a spherical shell of width 2.8 Å. The red and yellow patches on the surfaces indicate the regions which are reconstructed via displacement of Si atoms by $>10\%$ and $\leq 10\%$ of the average Si-Si bond length respectively.

highly nontrivial to infer the three-dimensional structure of voids from scattering measurements only. Observed X-ray or neutron scattering data More importantly, experimental data include general contributions from an array of inhomogeneities with varying shapes and sizes. So, it is hard to make sure the role of the individual factors in determining the shape and strength of the measured scattering intensity in small-angle scattering region. But simulation studies are free from such constraints and they are capable of addressing systematically the effect of different shapes, sizes, number densities and the nature of the distributions (e.g., isolated vs. interconnected) of voids or extended-scale inhomogeneities on scattering intensities. Before addressing these important issues, we examine the restructuring of a spherical void surface and the resulting changes of its shape due to atomic rearrangements during total energy relaxation of the surface atoms.

Figures 3.5(a) and (b) represent the reconstructed void surface of a spherical void of radius 6Å, and cylinder void of radius 6Å which are indicated as SP18-R6 and CY8-R6 in Table 3.2. As stated in section 3.2, voids are an empty cavity of radius r (6 Å for SP18-R6 & CY8-R6) with an interface width d (2.8Å). Atoms within the region of radii r and $r+d$ are defined as surface/interface atoms which is vulnerable region due to energy relation. The calculated radii of gyrations of this assembly of surface atoms before and after total-energy relaxation determine the degree of the void surface reconstruction and the shape of the void. For SP18-R6 and CY8-R6, it is observed that $\approx 50\%$ of total surface atoms displaced from their original position by more than 0.36 Å. This indicates a significant reconstruction of the

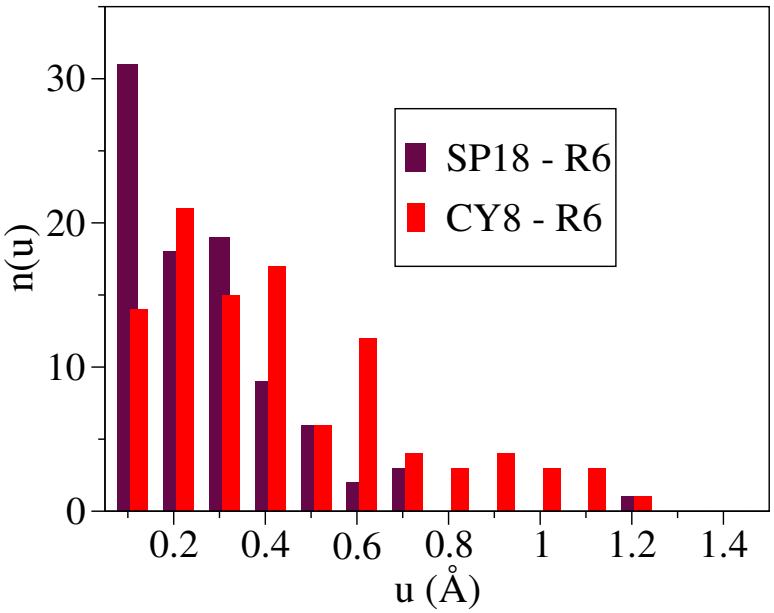

Figure 3.6: Atomic displacements distribution ($n(u)$ vs u) of the void interface atoms in model SP18-R6 and CY8-R6 after total-energy relaxation. The corresponding reconstructed surface due to displacement of interface atoms are shown in Fig. 3.5(a) and Fig. 3.5(b) in red color. In the displacement calculation, displacement $u < 0.1$ Å are neglected and only $u \geq 0.1$ Å are included.

void surface. These atoms are shown in Fig.3.5(a) and Fig.3.5(b) in red colors, along with the reconstructed regions of the surfaces with red patches. In Fig.3.6 the atomic displacement values of the corresponding atoms from their original position are presented.

The reconstruction of void surfaces due to total energy relaxation lower the local strain in the network and as a result the atomic coordination number via topological rearrangements occur. In Fig. 3.7 the same void in SP18-R6 model is shown where it has been found that several atoms on the surface of void change their coordination number from 2/3-3/4. Those atoms are shown with light blue color.

The scattering intensity of the SP18-R6 model, before and after relaxation are compared in Fig.3.8, where the effect of total energy relaxation on the three-dimensional void-surface reflective on the scattering intensity is depicted. It is observed that, scattering intensity varies significantly upon total-energy relaxation. One-dimensional scattering intensity variation, however it carry limited information associated with three-dimensional restructuring effect as observed in Fig.3.7.

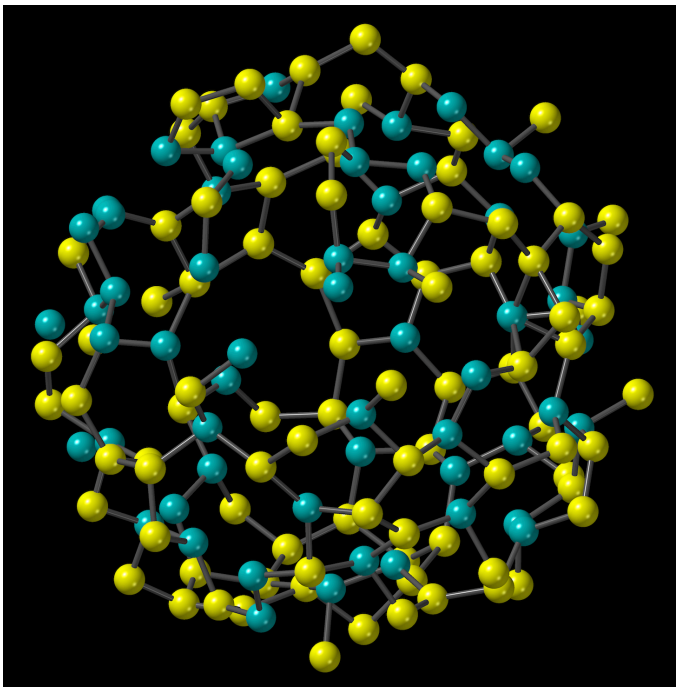

Figure 3.7: Void network in SP18-R6 model showing the local topological restructuring by changing coordination number after total energy relaxation. Light blue color represent the Si atoms of which coordination number increased during the process.

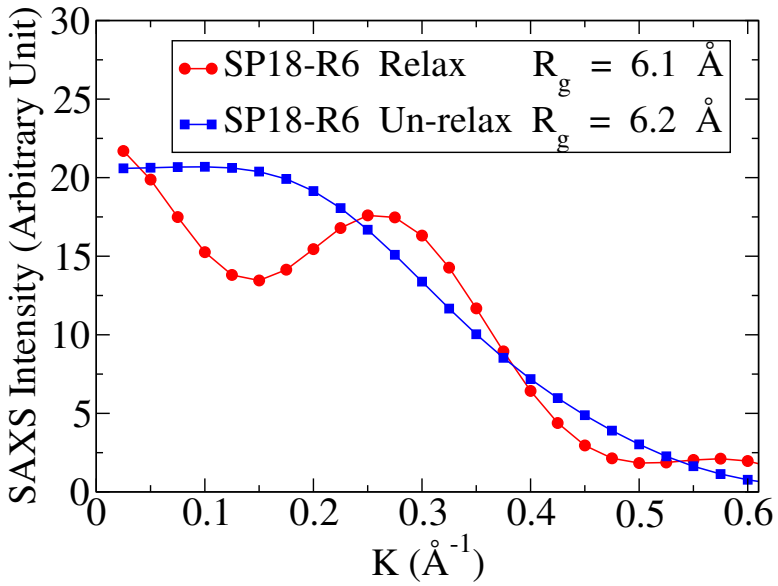

Figure 3.8: The variation of the scattering intensity due to three-dimensional restructuring of spherical void surface as shown in Fig.3.7 from SP18-R6 model after the total energy relaxation. The corresponding intensity from the unrelaxed structure is also included to examine the effect of relaxation.

3.3.3 Dependence of SAXS intensity on the volume-fraction of voids

Experimental data on *a*-Si from SAXS indicates that the scattering intensity in the small-angle limit is sensitive to the size and the total void-volume fraction of the voids present in the samples [2, 40, 57, 76, 162]. The variation of the scattering intensity with the volume fraction of the voids is clearly evident from simulations. By introducing nanosized spherical, ellipsoidal, and cylindrical shapes in ultra-large model of *a*-Si the dependence of the scattering intensity for different volume fractions of voids are studied. In this study, we choose an identical volume of spherical/ellipsoidal/cylindrical voids to ensure that any variation of the scattering intensity can be solely attributed to the total volume fraction or concentration of the voids. Following experimental observation [75, 78] we chose the void-volume fraction in the range 0.1-0.3% by adding different number of voids of identical volumes and shapes. Figures 3.9(a), 3.9(b) and 3.9(c) show the intensity variation for three different values of the void-volume fraction for spherical ellipsoidal and cylindrical shapes respectively. The actual radius for a given shape of the voids was kept same but with different concentration the numbers of voids in the models were different. The simulated data in Fig.3.9(a), 3.9(b) and 3.9(c) clearly show that there exist the variation of the intensity with respect to the total void volumes. For small values of k, the scattering intensity strongly depends on the volume fraction of the voids and it increases steadily with increasing values of the void-volume fraction from 0.1% to 0.3%.

3.3.4 Dependence of SAXS intensity on the size of voids

Likewise, the effect of void-volume faction, the effect of the void size on the scattering-intensity in *a*-Si are addressed by introducing voids of different sizes at a given volume-fraction of voids. The results for spherical, ellipsoidal and cylindrical voids for 0.3% are presented in Figs.3.10(a), 3.10(b), 3.10(c) respectively where a noticeable variation in the scattering intensity in the small-k region (below 0.4 Å^{-1}) observed in all cases. From this observation, it is concluded that, simulated scattering intensities of larger void is stronger in all cases. Two different effective of sizes 6 & 8 Å in spherical voids and ellipsoidal voids and 5 & 6 Å in cylindrical voids are shown in Figs.3.10(a) and 3.10(b), and 3.10(c) respectively where scattering intensity of 8 Å in spherical and ellipsoidal void and 6 Å in cylindrical void appeared stronger in small k region.

3.3.5 Effect of void shape on SAXS intensity

In this section, we examine the effect of the void shape on the scattering intensity in the small-angle region for *a*-Si. For this purpose, we are comparing the scattering intensity and

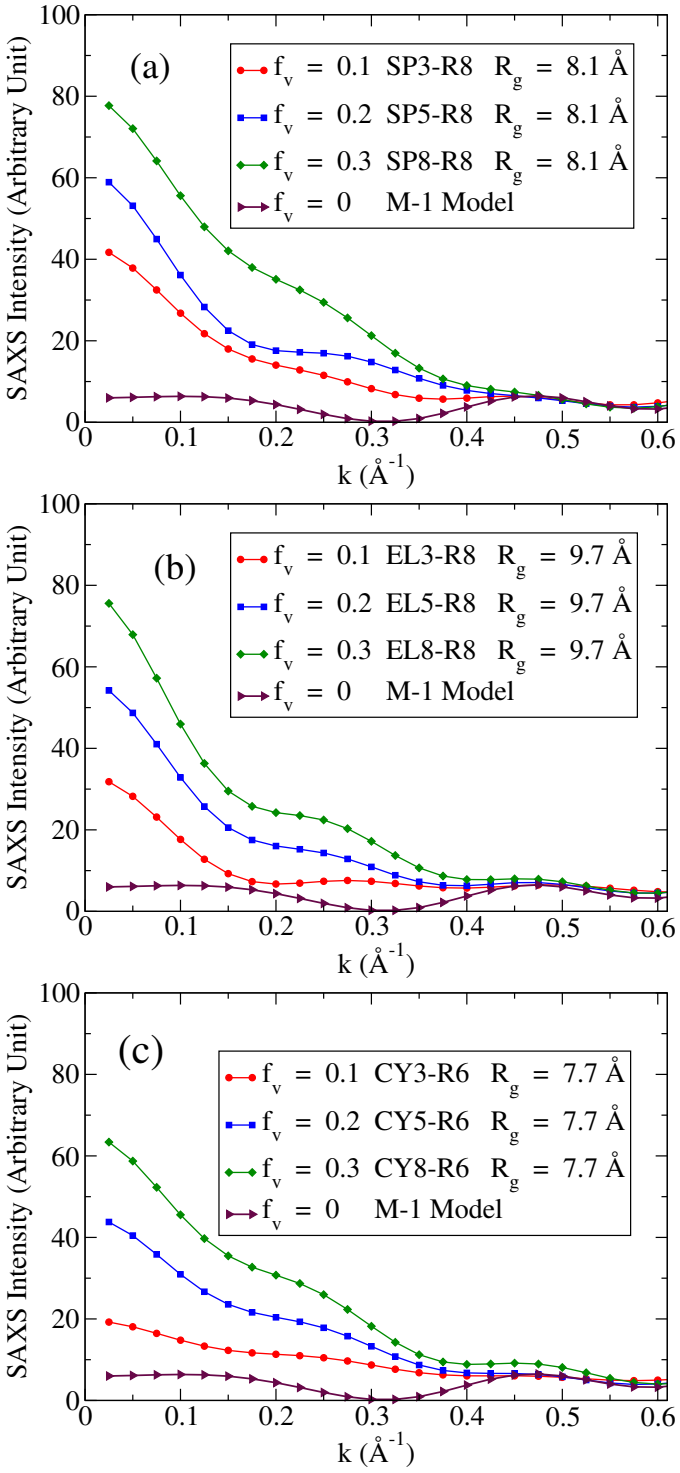

Figure 3.9: The variation of the scattering intensity of three void geometries (a) Sphere, (b) Ellipsoid, and (c) Cylinder, at three different void-volume fractions or void concentrations. SAXS intensity in the absence of geometrical void is included in each plot for comparison purpose.

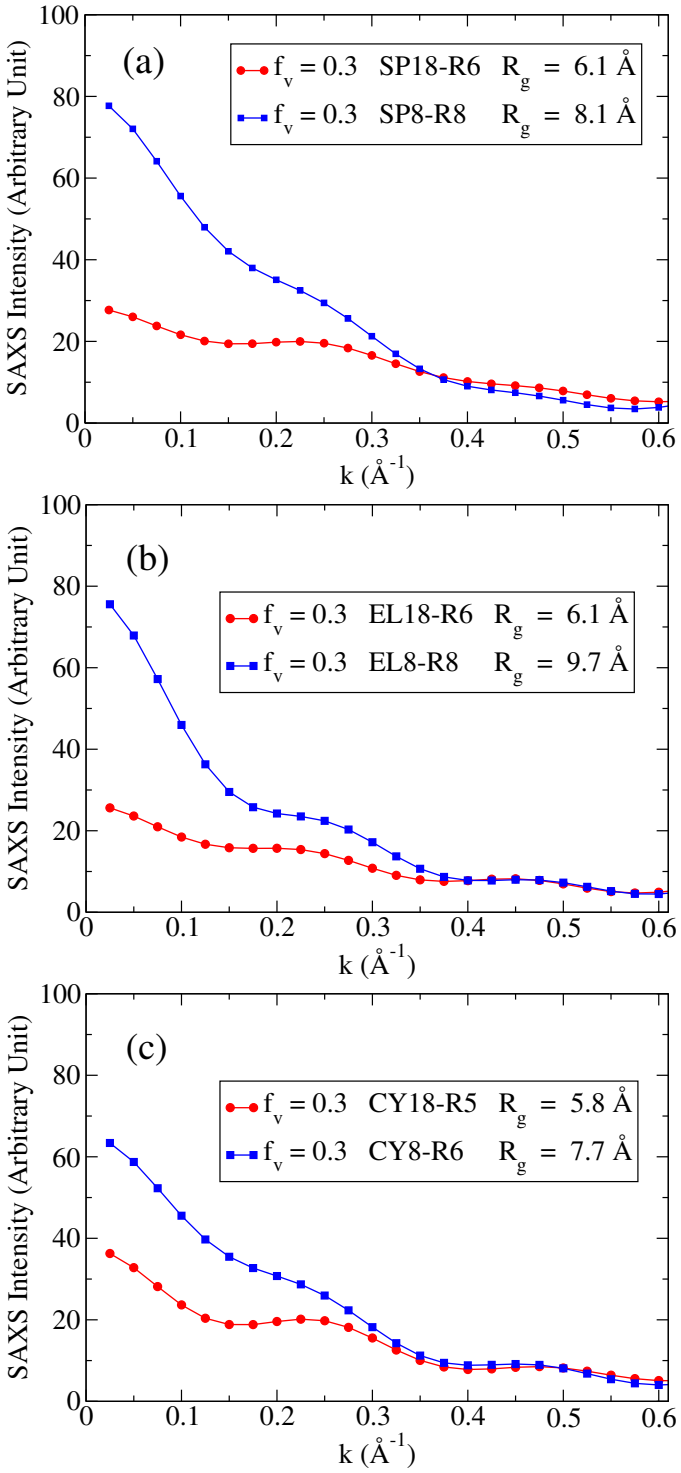

Figure 3.10: The scattering intensities for two different void sizes at 0.3% volume-fraction of voids for spherical, ellipsoidal and cylindrical voids are represented in (a), (b), and (c) respectively. The total volume-fraction of the voids (f_v) and average radii of gyration (R_g) are also included in the plots.

corresponding Kratky plots for three known geometries voids named Spherical, ellipsoidal and cylindrical. To observe the shape effect, we are considering the voids of all three shapes having almost the same individual volume, void concentration and the total volume. Any difference in SAXS intensity under examination with constraints; total void volume, individual void volume and void concentration as observed in As in Figs. 3.11(a), 3.11(b), 3.11(c) are purely from the void shape shape. At low void concentration (0.1%), the effect appear more as compared to high concentrations 0.2% and 0.3%. As, compared to the size and concentration effect of the scattering intensity of shape effect is appeared less but a deeply sincere observation shows that, scattering intensity form model with spherical voids is comparatively stronger than ellipsoidal and cylindrical void at constant individual void volume, total void volume and void concentration.

The Kratky plot [120] are used to examine the relationship between the shape of voids and scattering intensities. Where, the variation of $k^2I_c(k)$ with k are plotted in small k region. The background-corrected intensity I_c is obtained by subtracting the scattering intensity contribution from the amorphous-silicon matrix with no voids. The real and reciprocal space information are extracted by comparing the quantity $k^2I_c(k)$ which can analog of $rG(r)$. Variation of $k^2I_c(k)$ is more sensitive than the conventional intensity $I(k)$, which is the same as $rG(r)$ is more sensitive to structural ordering than the radial $g(r)$ only. Kratky plots are very popular and hugely used in probing the structure of biological macromolecules in solution. In the Kratky plot analysis, the variation of $k^2I_c(k)$ with k for the compact and globular (i.e., spherical) proteins are distinctly different and stronger than that of partially disordered and/or unfolded proteins [163, 164]. Specifically, an approximate semicircular variation of $k^2I_c(k)$ with k observed for a globular protein in the folded state and it gradually weakens or flattens out becoming partially disordered or unfolded state with the increasing the degree of structural disorder. In our amorphous network, this observation, we may expect that the shape dependence of the scattering intensity on a Kratky plot would be more pronounced for spherical voids than that for long cylindrical or highly elongated ellipsoidal voids (see Ref.[133]). Figures 3.12(a), 3.12(b) and 3.12(c) show the variation of $k^2I_c(k)$ for SP, EL, and CY voids at 0.1%, 0.2% and 0.3% concentration respectively. The quantitative understanding of the results are extracted following Deschamps and De Geuser [165], where k value corresponding to maximum $k^2I_c(k)$ value used to estimate the pseudo-Guinier radius as $R_{pg} = \sqrt{(}3)/k_{max}$. Claudio *et al.* [166] has been recently adopted this approach to estimate the size of silicon nanocrystals in bulk nanocrystalline (*nc*) doped silicon from small-angle neutron- scattering data in order to study the effect of nano structuring on the lattice dynamics of *nc*doped silicon. Similarly, Diaz *et al.* [167] also used in situ SAXS for the detection of globular Si nanoclusters of size 20–30 Å during

silicon film deposition by mesoplasma chemical vapor deposition(MPCVD). Our SAXS intensity profile are more or less identical to the same obtained by other authors for spherical void, so the similar observations can be extend to the study of other void geometries in their regular and inhomogeneous structures. The value of R_{pg} obtained from the peak positions in the scattering intensity for SP,EL and CY voids are indicated in 3.12(a), 3.12(b), and 3.12(c), which ranges from 5.3 Å- 6.3 Å. The presence of multiple peaks in a Kratky plot is suspected as an indicative of a nonspherical shape of scattering objects. The R_{pg} radii for all models are calculated and tabulated in Table 3.2. In all case corresponding R_{pg} values are lesser than the radius of gyration obtained from a conventional Guinier approximation and the average radii of gyration computed from the spatial distribution of the interface atoms in the vicinity of voids in a model.

3.3.6 Effect of void spatial distribution on SAXS

This observation is consistent with the earlier experimental studies by Mahanetal [40] and Leadbetter *et al.* [168], and the recent study by Young [169], where a weak dependence of the nature of the scattering curve on the shape of the voids or inhomogeneities was reported via tilting experiments. It may noted that accurate simulation studies, based on large *a*-Si models, are particularly important in studying the dependence of the scattering intensity on the shape of the voids as it is extremely difficult to control the void shape in experiments while maintaining the size and total volume fraction of the voids. The effect of the spatial distribution of the voids on the scattering intensity can be studied conveniently by generating a number of suitable isolated and clustered distributions of voids in real space. Since the microstructure of thin-film amorphous silicon is characterized by voids or inhomogeneities with a varying mass distribution, it is important to examine to what extent a sparse or clustered distribution of voids/inhomogeneities can affect in the scattering intensity in *a*-Si.

Experimentally, it has been observed that helium-effusion measurements can determine the existence of isolated and interconnected voids in thin-film amorphous silicon. Beyer *et al.* [78, 80, 170] have shown that the presence He-effusion peaks at low and high temperatures are associated with the diffusion of He atoms through an interconnected void region and the trapping of He atoms in a network of isolated voids, respectively. These authors have further noted that hydrogenated samples of *a*-Si prepared by the vacuum evaporation technique can have a high concentration of isolated voids.To examine this, we have studied a number of models with different spatial distribution of voids. Scattering intensity of six void distributions with surface-to-surface distance D, 6 Å, 12Å and 18Å at 0.1% volume-fraction and 1Å, 8Å and 14Å at 0.3% are presented. Figure 3.13(a) and 3.13(b) show the scattering

intensity value depends on the of the surface-to-surface distance D. Higher values of D correspond to more sparse distribution of voids which gives weaker scattering.

3.3.7 Guinier's law and the size of the inhomogeneities from SAXS

In deriving Eq.(3.4) we have noted that a peak in $S(k)$, represented by a delta function, at $k = 0$ was excluded explicitly to arrive at the expression for the static structure factor. Such an exclusion can be readily justified in experiments by recognizing that the central peak, being dependent on the external shape of the sample, is extremely narrow and thus it practically coincides with the direct (or incident) beam. Analogously, one may invoke a similar assumption in computer simulation of SAXS by employing a large but finite-size model of amorphous solids so that the computed values of the intensity at small k values are minimally affected. Guinier has shown that for a homogeneous distribution of particles (e.g., voids) in the dilute limit, the intensity of scattering for small value of k can be approximated as in Eq.(2.30). provided that the particles are distributed randomly with all possible orientations and $kr_g < 1$. In Eq.(2.30), r_g is the radius of gyration of the particles and the inter-particle interaction is neglected owing to the dilute nature of their distribution. This relationship between the intensity and the wavevector in the small-angle limit is popularly known as the Guinier's law and it is frequently employed in experimental determination of the size of nano-size particles or extended inhomogeneities using SAXS. In the context of the present work, this suggests that as long as the voids are distributed randomly (within a large model) in a dilute environment, one should be able to estimate the size of the voids from the shape of the intensity curve for small values of k. In practice, the calculation of the scattering intensity from Eq.(2.30) in the small-angle limit is constrained by the effective cutoff distance (R_c) of the reduced pair-correlation function and the size (D) of the inhomogeneities, which determine the lower and upper limits of k, respectively. For the present simulations, these values correspond to an approximate k-range of 0.1 Å^{-1} to 0.4 Å^{-1}.

Figure 3.14(a) shows the comparison of the experimental data from Ref.[2] with the results obtained from our simulations for a void-volume fraction of 0.3% on a Guinier plot, where, following Eq. (2.30), the scattering intensity is expressed in the natural log-scale as a function k^2. The simulated values of the intensity match closely with the experimental data, except for very small values of k^2 below 0.05 Å^{-2}. The deviation for small values of k is not unexpected, and can be attributed partly to the difficulty in extracting information beyond R_c from the reduced pair-correlation function and in part to the intrinsic differences between simulated models and experimental samples. Since the latter generally include, depending

upon the method of preparation and experimental conditions, voids of sizes from 5Å to 15Å, it is difficult to compare simulated data with experimental results at a quantitative level for very small values of k. The Guinier's law in Eq.(2.30), suggests that the approximate size of the voids/inhomogeneities can be obtained from the slope of the $\ln I(k)$ vs. k^2 plot. Since the slope of the intensity curve is directly proportional to the square of the radius of gyration, it is possible to compare the Guinier's radius (of gyration) with the actual size of the voids used to generate the void distributions in the models. In Fig.3.14(b), we have plotted $\ln I(k)$ as a function k^2, for spherical, ellipsoidal, and cylindrical voids. Since the values of the are close to each other for three different shapes, the results for the ellipsoidal and cylindrical voids are shifted downward by 5 units for the clarity of presentation. The radii of gyration obtained from the slopes of the fitted plots are indicated as r_g, where as R_g reflects the average value of the gyration radius computed from the real-space distribution of the interface atoms that surround a void. Evidently, the latter is larger than the actual size of the void. For the purpose of comparison, we have subtracted 1.4 Å, a length equal to the half of the interface width d from R_g and have listed the corresponding corrected values for each model in the plots and in Table 3.2. Thus, R_g provides an upper bound of the average radius of gyration of voids.

3.4 Conclusions

In this chapter, we have shown structural detail of computer generated 262400 atoms models of a:Si. In our method smoother and experimentally closer static structure factor of the a:Si is observed than any other finite size simulated models, where the hidden structure for small k regions have been estimated by extrapolation from higher k regions. In our 262400 atoms model, structure below 0.07 Å^{-1} are theoretically unpredictable, so extrapolation of $S(k)$ at $k = 0$, by using a second-degree polynomial in k in the region $0.15 - 1.0$ Å^{-1}, gives a value of 0.0154 ± 0.0017. During relaxation of void surfaces, the surface reconstruction in terms of the coordination and atomic displacement are observed different for different shaped of voids. The geometrical aspect to understand the effect of existing voids in a:Si by analyzing simulated SAXS patterns conclude that SAXS patterns highly depend on void concentrations and the sizes of the voids. An intense SXAS patterns can be associated primarily either with higher void concentrations or with lager sizes of voids. SAXS patterns are less sensitive to the shape and distribution of the voids as compared to concentration and size of the voids. If the same number density of voids and same individual voids volume leading the same total void volume, then almost identical SAXS patterns can be obtained for different shapes for $k > 2$ Å^{-1} and vey little shape dependence can be observed for $k \leq$

2Å^{-1}. If the voids are distributed in a:Si network then strong and smooth SAXS patterns corresponds to compactly and sparsely distributed voids respectively. In conclusion, at fixed f_v the clearly observed size and concentration effect on SAXS patterns are independent of method of void generation.

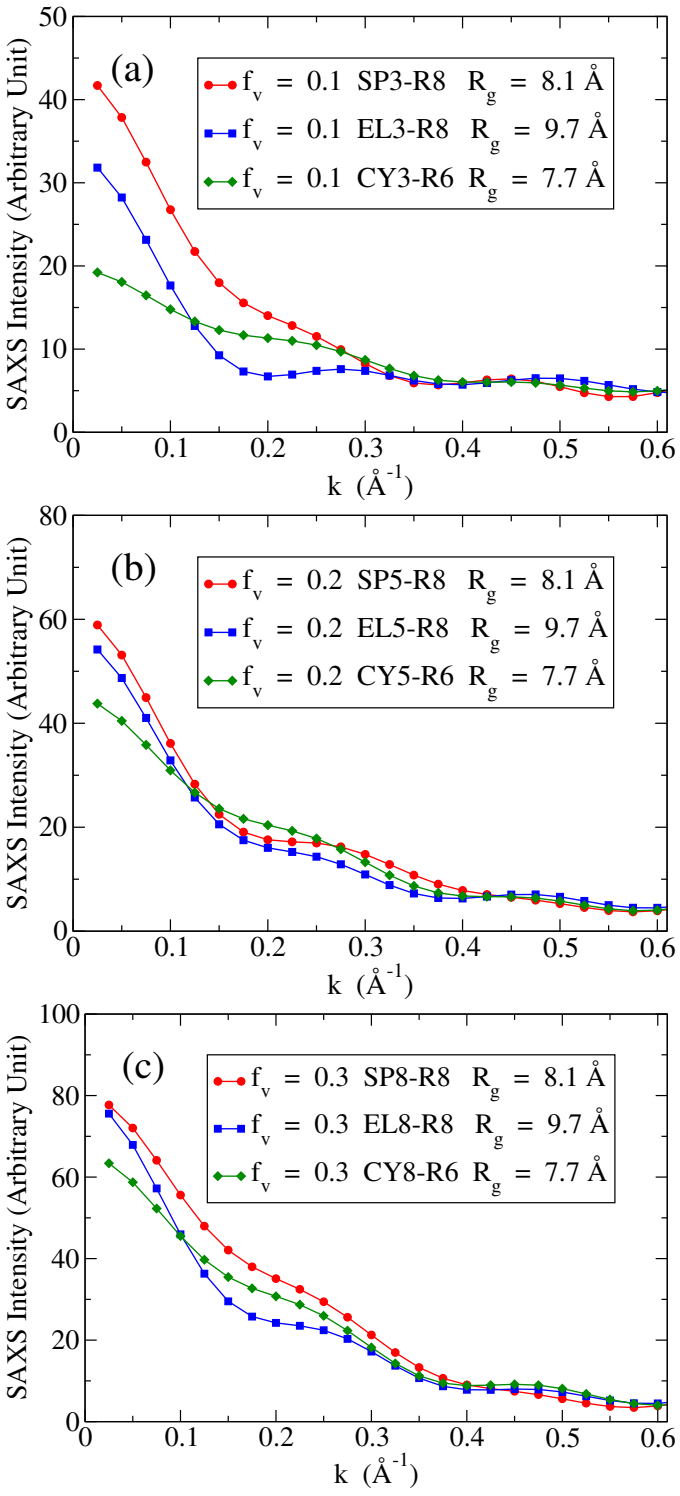

Figure 3.11: The scattering intensity variation with the shape of the voids at fixed void concentration in *a*-Si. For the comparison purpose, the total and individual volumes of all three shapes; spherical (SP), ellipsoidal (EL), and cylindrical (CY) and the concentration of the voids are kept identical.

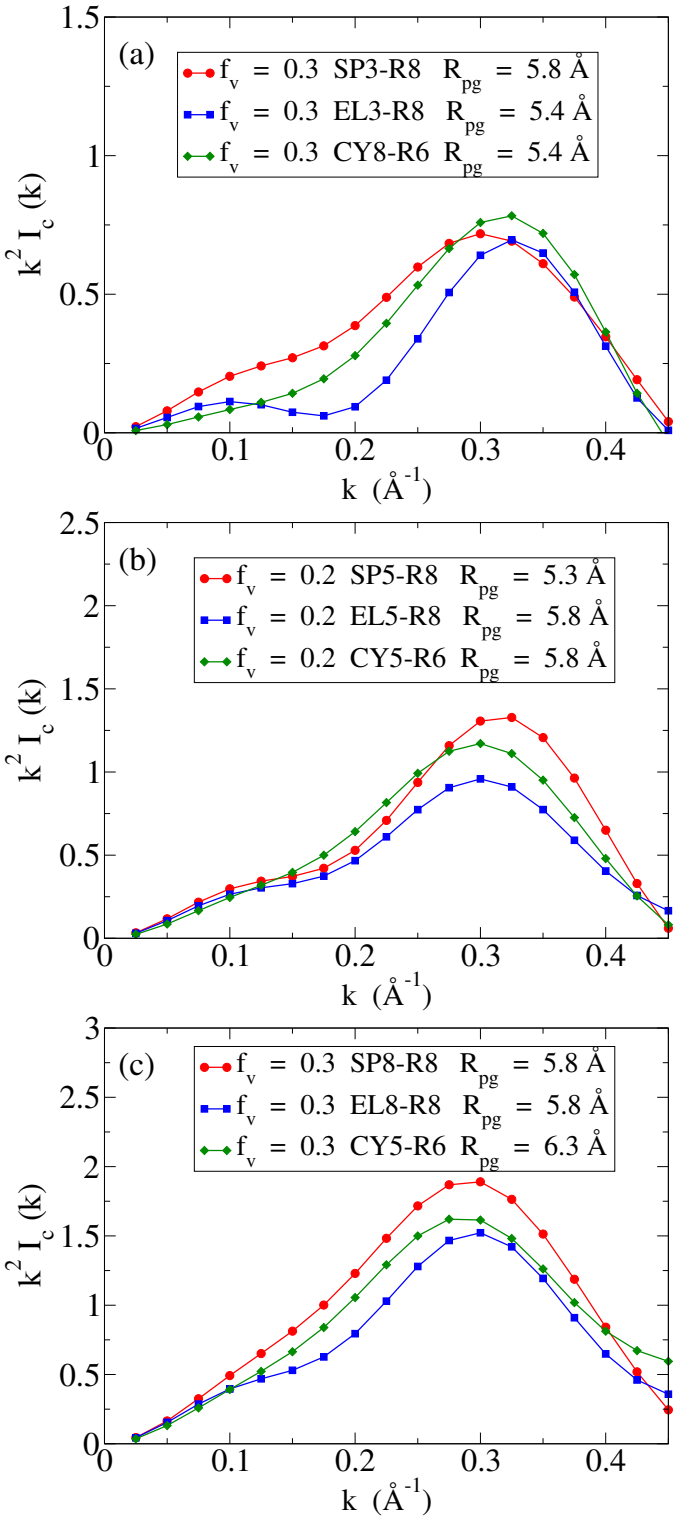

Figure 3.12: Kratky plots showing the variation of the $k^2 I_c(k)$ with k for SP, EL, and CY voids of identical individual and total volume. Where, $I_c(k)$ and R_{pg} corresponds to the background corrected intensity and pseudo-Guinier radii.

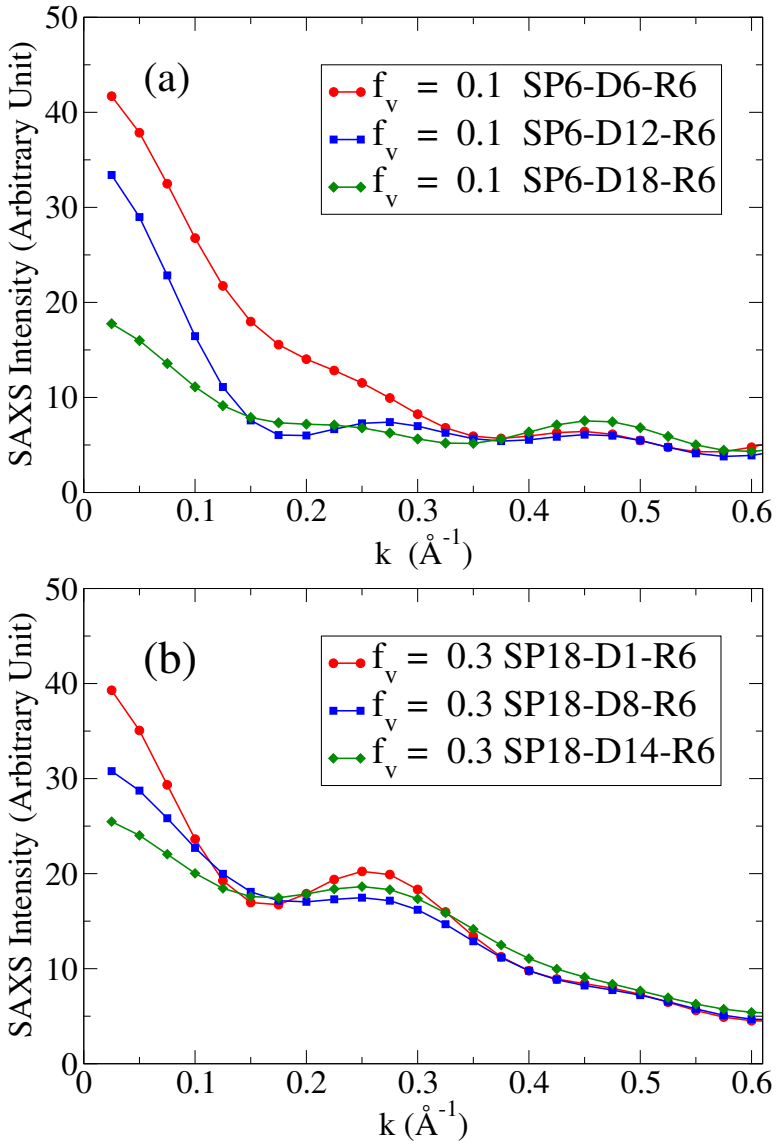

Figure 3.13: The variation of the scattering intensity due to the spatial distribution of the voids in ultra-large model of *a*-Si at fix volume fraction, and size of the voids. The the degree of sparseness of the void distribution is characterized by indicated surface-to-surface distance (*D*) between the voids.

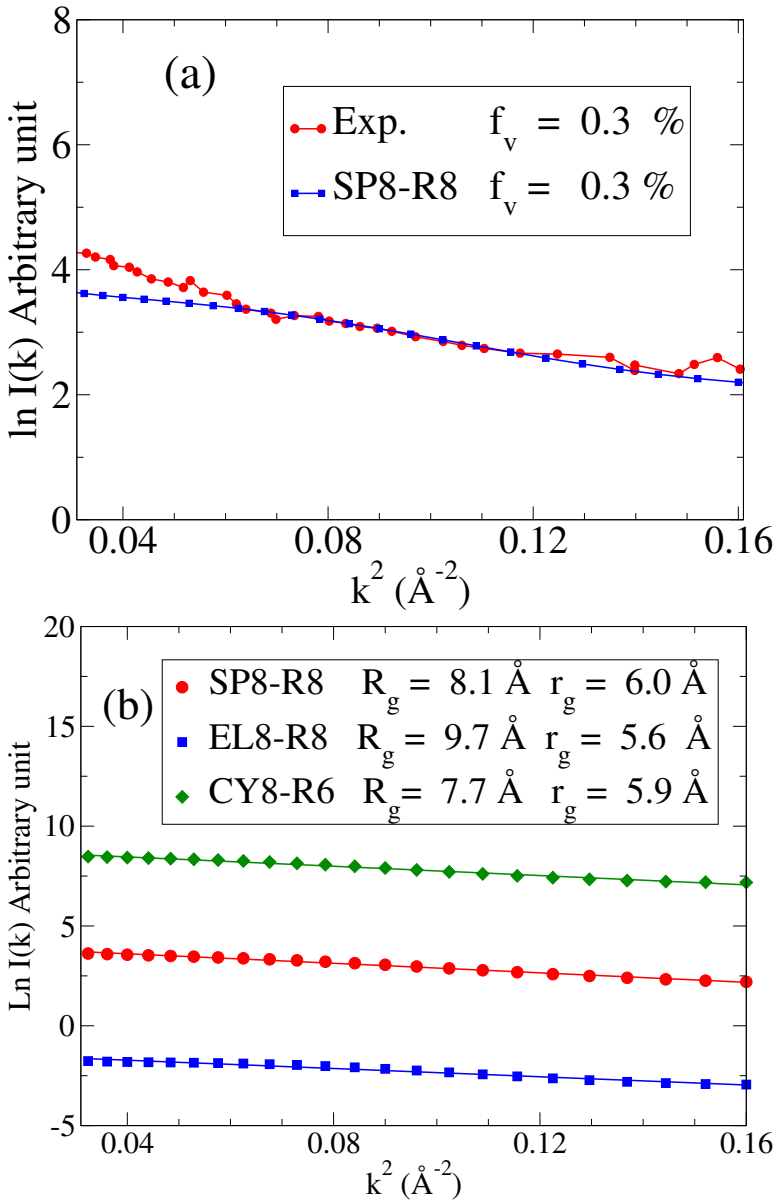

Figure 3.14: (a) A comparison of Guinier's plots for experimental (Ref.[2]) and simulated SAXS data of *a*-Si at volume fraction of void ≈ 0.3%. (b) Simulated Guinier's plots for SP, EL, and CY voids models at 0.3% volume fraction of voids. The calculated radii of gyration (R_g), from the real-space distribution of void interface atoms and the Guinier's plots are indicated in plots.

Chapter 4

EFFECT OF LOW-TEMPERATURE ANNEALING ON VOID-RELATED MICROSTRUCTURE

In the previous chapter, we have seen that, there exit a little shape dependence on SAXS intensity at void volume fraction of $\geq 0.2\%$ in small angle region. So, it is important to study, the SAXS intensity dependance for a particular shape at constant void concentration. In this chapter, we are addressing the void surface reconstruction at low-temperature annealing and the corresponding SAXS intensity profile related with restructured void. The work presented here is elaborated from the accepted conference paper by Durga Paudel, Raymond Atta-Fynn, David A. Drabold, and Parthapratim Biswas in Journal of Physics Conference Series.The outline of this chapter is as follows. Introduction of the void microstructures is discussed in section 4.1. Low temperature annealing of ultra-large model of *a*-Si and methods of reconstruction measurement of void are discussed in section 4.2. The effect reconstruction due to annealing on void surface and on simulation SASX intensity are discussed in result section 4.3. Finally, the results are summarized in section 4.4.

4.1 Introduction

However the existence of voids in amorphous silicon (*a*-Si) is well known with the help of the electron spin resonance (ESR) [25], high-resolution electron diffraction and electron microscopy [72] experiment since couple of decades, but the shape of the voids and related microstructral informations are not quite enough till date. An experimental and theoretical study of the void shapes and their reconstruction due to annealing at low temperature is important to establish the *a*-Si material before they use in actual electronic device applications; like solar cell, liquid-crystal display, thin-film and several other semi-conducting devices. The small change in void structure can be studied in theoretical model which will be pure structural information of void. Three-dimensional visualization of void in real space and corresponding change in small-angle X-ray scattering in reciprocal space provide useful informations which are obscure and difficult to extract in experiment. In this behavior is addressed using simulated ultra-large models of *a*-Si annealed at low temperatures.The effect of total energy relaxation on the shapes are also presented. To the end, we have

examine carefully the internal surfaces of void at void volume concentration $f_v = 0.3\%$ at 300 K– 600 K during annealing and total energy relaxation.

4.2 Computational Method

4.2.1 Model-Generation

In this chapter, the same atomistic models are used as in chapter 3. Here, we examine only ellipsoidal voids and annealed them classically to 300 K- 600 K. Annealed configurations named Ann-300K, Ann-400K, Ann-500K and Ann-600K corresponds to four different temperatures 300 K, 400 K, 500 K and 600 K were collected independently. In addition to the annealed configurations, we collect the relaxed configurations of corresponding annealed models and they are named as, Rel-300K, Rel-400K, Rel-500K, Rel-600K. As, the models under study were ultra-large, the total energy was minimized using the limited-memory Broyden-Fletcher-Goldfarb-Shanno (BFGS) algorithm [145] to obtain an equilibrium configuration. The summary of the structural properties of equilibrium configurations were tabulated in table 3.1.

4.2.2 Ellipsoidal Voids

In ulra-large models RM1 and RM2, ellipsoidal voids were randomly introduced with an imposed constraint 'no-one of voids surface overlap'. In oder to study void surface evolution of isolated voids upon thermal and energy treatment, we chose void parameters on the basis of experimentally guided nanometers inhomogeneity (denoted by R) in the range 5–10 Å [57] and skin width (d) of 2.8 Å around the void. With provided skin width, reconstructed void surface domain ranges $R \pm d$ for each void. The effect of temperature and relaxation on void surface were examined by plotting QuickSurf with the help of VMD software [171]. The correlation between the simulated SAXS patterns from voided models and void surfaces of corresponding temperatures before and after relaxation were examined. In this work, only tri-axial ellipsoidal voids surface at 300 K -600 K and SAXS patterns of corresponding temperature at annealed and relaxed stage are presented. Under void generation, axes ratio for ellipsoidal void was chosen $\alpha : \beta : \gamma = 0.5R_v : R_v : 2R_v$, where of void radius $R_v = 6$ Å. Parameters α, β and γ were defined in terms of the components R_{gi}, $i = x, y, z$ values as,

$$\begin{cases} \alpha = R_{gx}/(R_{gx}R_{gy}R_{gz})^{1/3} \\ \beta = R_{gy}/(R_{gx}R_{gy}R_{gz})^{1/3} \\ \gamma = R_{gz}/(R_{gx}R_{gy}R_{gz})^{1/3} \end{cases} \tag{4.1}$$

Normalized aspect ratios:

$$\begin{cases} \alpha' = \alpha/\alpha \\ \beta' = \beta/\alpha \\ \gamma' = \gamma/\alpha \end{cases} \tag{4.2}$$

The thermal effect on SAXS patterns for *a*-Si having ellipsoidal void of effective length 6Å, number density 0.33×10^{19} cm^{-3} and void volume fraction 0.3% are compared before and after total energy relaxation at 300 K–600 K. The corresponding, three-dimensional appearance with the help of calculated normalized aspect ratios are compared at that temperature.

4.2.3 SAXS Analysis

Small-angle X-ray scattering analysis used in this work is based on the calculation of static structure factor ($S(k)$) which is the function of the wavevector ($\vec{k}$). $S(k)$ of desired configuration is calculated by using the reduced radial distribution function $G(r)$ [Ref. Eq. (2.26) and Eq. (2.25)] of that simulated model. The smoothness on the structure factor help to explain the correlated shape change due to thermal annealing and relaxation. For this purpose, we are presenting scattering intensity of the same void model at different temperatures. Also, how the smoothness or hyper-uniformity change with the effect of temperature and relaxation were also presented in this chapter.

4.3 Results and Discussions

4.3.1 Structure factor and Scattering Intensity

In earlier chapter, we have examine the validity of the simulated models by comparing simulated structure factor with same experimental [**?**] data. Long-range, behavior of $S(k)$ in simulation and experiment were observed identical but in small-angle region, there were slight fluctuation. The fluctuation in $S(k)$ due to thermal annealing and total energy relaxation for all other identical conditions are presented in this section by comparing the $S(k\to 0)$ values. The structure fracture of the monoatomic system at small k value can be approximate using the second order polynomial $p(k) = a + bk^2$, where a and b are polynomial coefficients. Coefficient a define the value of $S(k\to 0)$ which is the measure of hyper-uniformity. $S(k\to 0)$ value for all thermally treated models at $f_v = 0.3\%$ before and after total energy relaxation obtained by fitting $p(k)$ polynomial in the range 0.15 –1.2 Å^{-1} are tabulated in Table 4.1. $S(k\to 0)$ value of corresponding models are compared with the same at $f_v = 0\%$ and before the thermal treatment.The value of $S(k\to 0)$ in the range

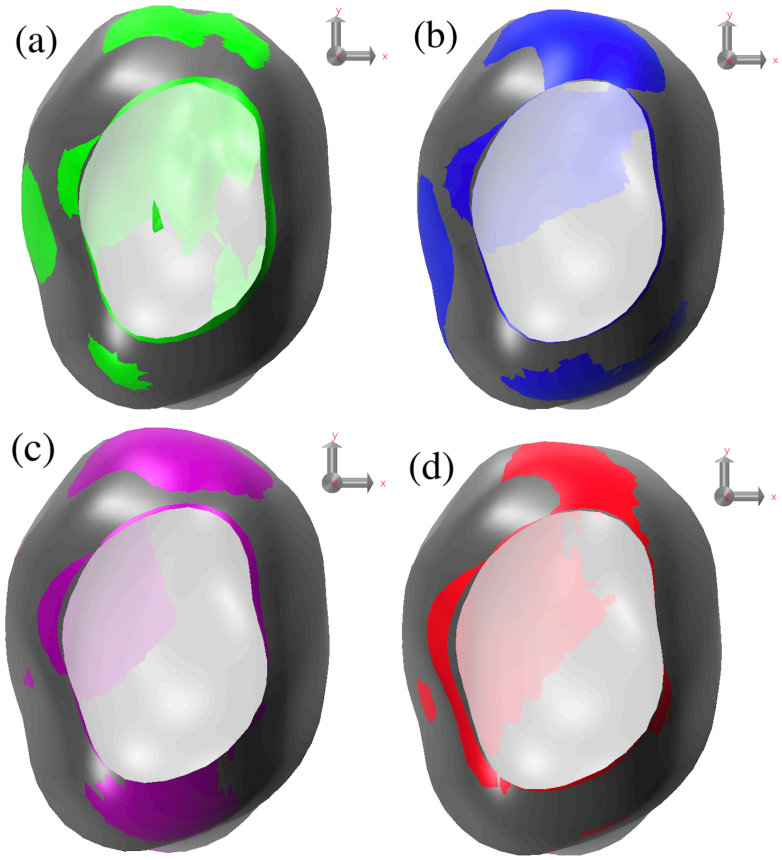

Figure 4.1: Void surfaces of *a*-Si model annealed at (a) 300 K (green) (b) 400 K (blue), (c) 500 K (pink), (d) 600 K (red). All the surfaces are overlapped with their original gray surface for comparison.

[0.15:1.2] $Å^{-1}$ before annealing the model is observed as 0.0502 which was 0.0154 in the same model in the absence of void.

4.3.2 Restructuring of voids during annealing and relaxation

Three-dimensional surface of ellipsoidal voids using Visual Molecular Dynamics (VMD) [171] are shown in Fig.4.1 and Fig.4.2 for annealed and relaxed model respectively. In both annealed and relaxed void structures, the original void surface (gray surface) is used as a reference surface. Green, blue, purple and red color surface in Fig.4.1(a), (b), (c) and (d) represent 300 K, 400 K, 500K ad 600 K respectively. VMD plots were drawn at identical parameters 0.5, 0,1.0,1.0, and 1.0 respectively for resolution, radius scale, density isovalue, grid spacing with the maximum surface quality. Any difference in surface can be predicted with the unequal distribution of the color patches. It is observed that, in Fig.4.1(a), (b), (c) and (d) color patch distribution of all four temperature are different, which means that even

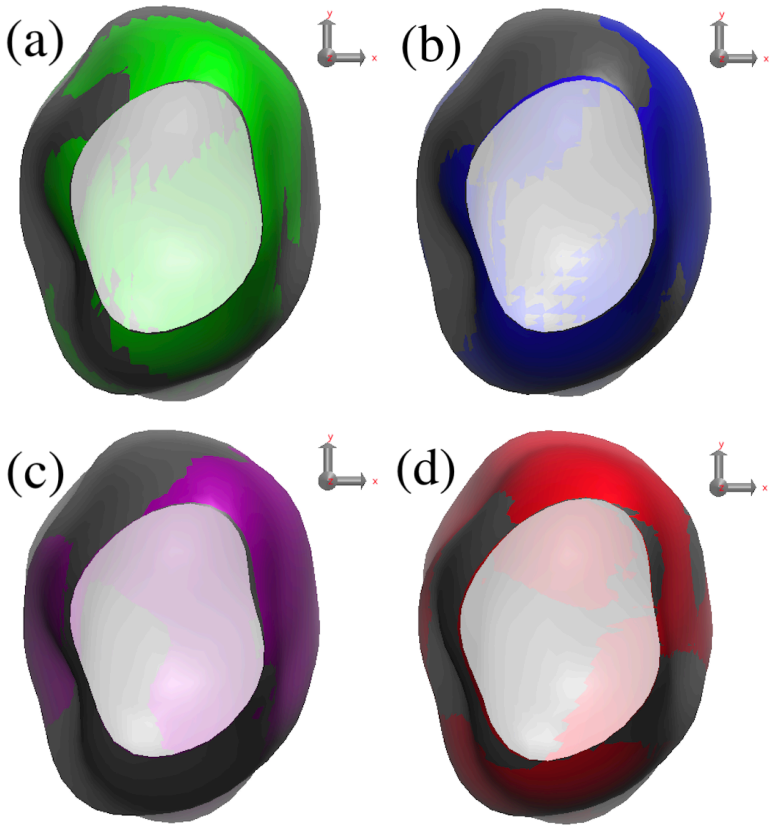

Figure 4.2: Relaxed void surface after annealed at (a) 300 K (green) (b) 400 K (blue), (c) 500 K (pink), (d) 600 K (red). All the surfaces are overlapped with their corresponding annealed surface (gray) for the comparison purpose.

at low temperature (300 K– 600 K) there is restructuring in void characteristic properties which are visible in high-quality three-dimensional surface rendering. This observation is consistent with the radii of gyrations calculated based on the spatial distribution of the void surface atoms. As the original void surface (gray), was featured by surface atoms around ellipsoidal void of effective radius 6 Å with skin width of 2.8Å, non-uniformly distributed green, blue, purple and red colors patches appearing on surface (Ref. Fig. 4.1(a)) signifies that on annealing void, void surface construct non-uniformly and as a result the size and shape of voids changes. This is consistent with the other experimental [172–174] and simulation [175–177] results.

In this observation, we found that the void size drop by 0.71%–1.14% while on annealing the void form 300 K– 600 K. In Fig. 4.2, the void structure of relaxed model are compared with their corresponding annealed structure. This time, gray surface represent the annealed structure at that temperature and green, blue, purple and pink surface represent the void surface of relaxed structure after annealing at 300 K, 400 K, 500 K and 600 K respectively.

Table 4.1: Characteristic properties ellipsoid of void in *a*-Si models.R_g (Å), $R_{gi}, i = x, y, z$, α', β', γ', ΔR (%), r_g and $S(k \to 0)$ respectively indicate the calculated radius of gyration, their x, y and z components, normalized aspect ratio along x, y and z directions, change in radius of gyration, Guinier radius of gyration and structure factor at $k \to 0$.

Models	R_g(Å)	R_{gx}	R_{gy}	R_{gz}	α	β	γ	ΔR(%)	r_g(Å)	$S(k \to 0)$
No void	—	—	—	—	—	—	—	—	—	0.0154
Original	8.62	2.95	4.36	6.82	1	1.48	2.31	0	5.75	0.0502
M1-Ann-300 K	8.55	2.86	4.36	6.77	1	1.52	2.37	0.71	4.53	0.0795
M1-Ann-400 K	8.57	2.84	4.35	6.81	1	1.53	2.40	0.75	3.34	0.0561
M1-Ann-500 K	8.54	2.77	4.38	6.79	1	1.58	2.45	0.75	5.47	0.0588
M1-Ann-600 K	8.55	2.78	4.30	6.85	1	1.55	2.46	1.14	3.39	0.0537
M1-Rel-300 K	8.56	2.83	4.37	6.80	1	1.54	2.40	0.7	4.33	0.0753
M1-Rel-400 K	8.58	2.85	4.36	6.81	1	1.53	2.39	0.46	4.66	0.0677
M1-Rel-500 K	8.53	2.81	4.34	6.78	1	1.54	2.41	1.04	5.27	0.0601
M1-Rel-600 K	8.57	2.79	4.39	6.81	1	1.57	2.44	0.58	4.58	0.0706

In this observation, we have seen that, the total energy relaxation rearrange the atomic distribution of the individual voids which appeared in the 3-dimensional structure with the color patch but there is not a significant different in an average size of the void. In table 4.1, the void size of relaxed structure, the components of radii of gyrations are tabulated. Radii of gyration of original void is bigger than any other annealed and relaxed void. So, at all temperatures, distributed gray color patch identify the bigger size void. On annealing to 300 K– 600 K, the void surface reconstruction happened with different strength.To measure the strength in x, y and z directions, the component of radii of gyrations R_{gx}, R_{gy} and R_{gz} were calculated and they are listed in table 4.1. An observed R_{gi}, $i = x, y, z$ value for annealed and relaxed models are also lesser than that of the original void. Unequal normalized aspect ratios α', β' and γ' at four temperatures before and after relaxation signifies the reconstruction of the voids during annealing at low temperature.

4.3.3 Void displacement distribution

The void displacement distribution provide us the useful information about the dynamics of the void surface atoms during annealing and relaxation. Displacement of all void surface atoms at 300 K–600 K were calculated from their original void position. An observed three-dimensional void surface and lower radius of gyration during annealing up to 600 K temperatures signifies that void surface atoms were moving towards the cavity. During their movement, displacement of void surface wall ranges from 0–1.8 Å. Some of the surface atoms were not displace at all.

In Fig.4.3(a) and (b) only those Si atoms having displacement ≥ 0.1 Å are presented where the displacement of void surface atoms at 300 K & 500 K and 400 K & 600 K are plotted respectively. At all four temperatures, it is observed that, the majority of Si atoms on the void surface wall have displacement up to ≈ 0.8 Å. Very few of them have displace by > 0.8Å. In Fig.4.3(a), there is a significant difference between the number of displaced Si atoms at 300 K and 500 K. For example, 22 Si atoms displace by 10% of Si-Si bond length at 300 K, but only 10 of them have same displacement at 500 K. Similarly, based on the atomic displacement the observed difference in 3D void surface at 400 K and 600 K can be understand form the displacement distribution. At 400 K, 22 Si atoms appeared to displace by 14% of Si-Si bond length but at 600 K only < 10 Si atom have the same displacement.

The void surface in annealed models after total energy relaxation are slightly smaller in size as compared to that surface before relaxation. This information can be clearly observed in 3D void structure in Fig.4.4, where the lesser distribution of green, blue, purple and red colors patched over their corresponding annealed void before relaxation in gray color. Comparing the void restructuring effects in annealed model before and after total energy relaxation, a lesser effect is observed after relaxation. Figures 4.3 and 4.4 show that atomic displacement drop by almost 75% after relaxation in an annealed sample. For example, maximum displacement observed in relaxed model in ≈ 0.5Å which was $\approx$2Å in annealed model.

4.3.4 Effect annealing and relaxation on SAXS

In an annealed system, there is restructuring of nanosized inhomogeneity which may affect the scattering of X-rays. It is difficult to measure precisely the three-dimensional structure of voids from scattering measurement only. But the restructuring of nanosize void as observed in 3D structures are also reflecting on scattering intensity. As we already saw the size and hence volume of the void changes upon annealing and as a result the void surface reconstruction happen. The scattering intensity measurement also provide the average size of reconstructed void with Guinier approximation. In table 4.1 the Guinier radius of gyration before and after relaxation in annealed sample are listed. They are compared with the same for the original void. The asymptotic behavior of above SAXS intensity predict an average size of voids in corresponding sample. In fig.4.5(a) and (b) SAXS patterns at four temperatures are distinctly different in small-angle region, which is due to changed in shape of voids up on thermal treatment.The radius of gyration of reconstructed voids calculated in (i) real space with spatial distribution of void surface atom (R_g) and (ii) reciprocal space with Guinier best fit for SAXS intensities (r_g) are compared in table 4.1. For the real space

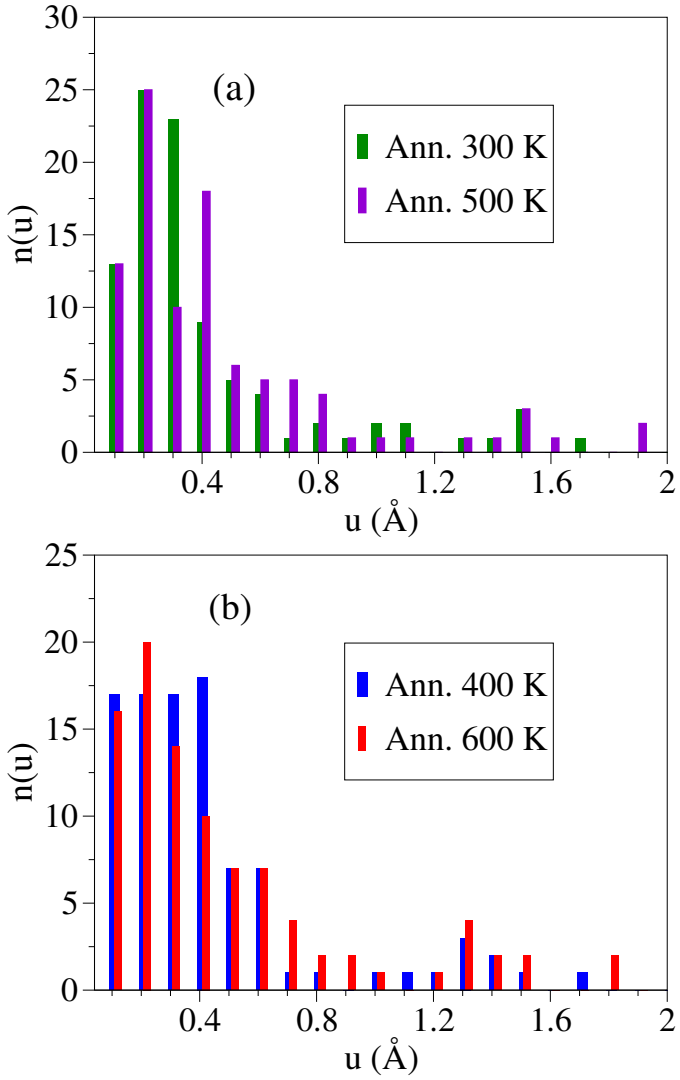

Figure 4.3: Void displacement distribution of annealed models. (a) Green and purple color represent displacement at 300 K and 500 K and (b) blue and red color surface represent the same at 400 K and 600 K. All the displacements are calculated with reference to the original void corresponding to gray surface in 3D voids (Refer Fig. 4.1).

information an additional 2.8 Å is added from the actual void. So, it could be possible to have at most 2.8 Å difference in R_g and r_g values.

4.4 Conclusions

Using simulated SAXS technique in conjunction with geometrical approach of void and high-quality three-dimensional rendering software, a quantitative study of nanoscale inhomogeneities in *a*-Si at four different temperatures are studied. Results shows that, void morphology and corresponding SAXS intensities in small-angle region are dependent of the

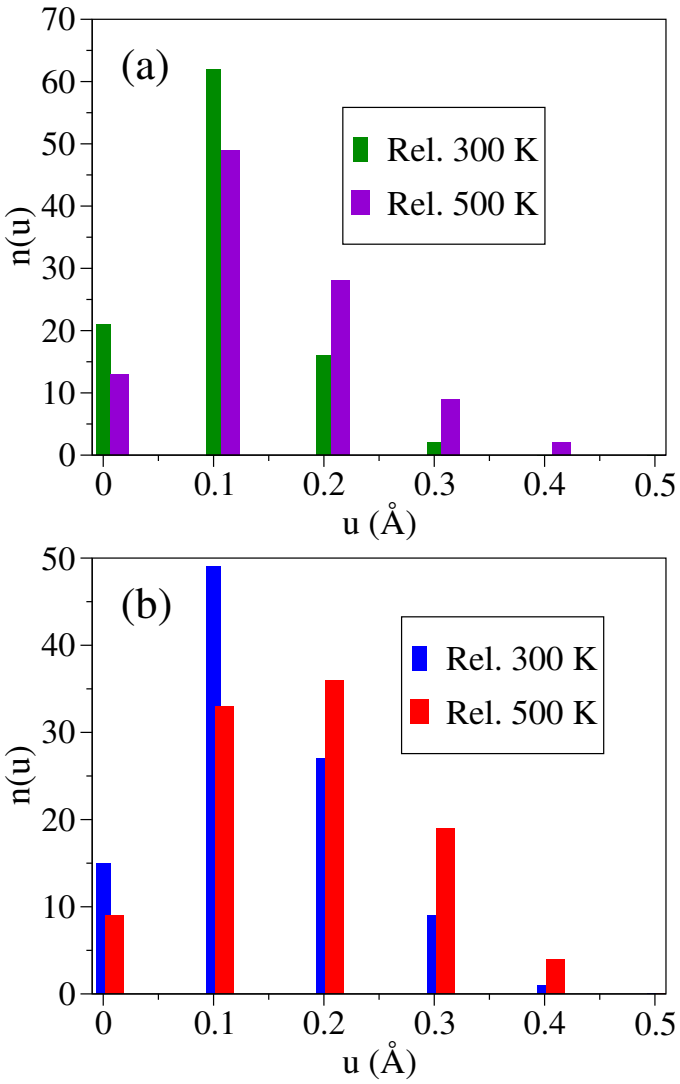

Figure 4.4: Void displacement distribution of relaxed models. (a) Green and purple color represent displacement at 300 K and 500 K and (b) blue and red color surface represent the same at 400 K and 600 K. The displacements are calculated with reference to their own annealed void corresponding to gray surface in 3D voids (Refer Fig.4.2).

annealing temperature($\leq$ 600 K). Upon annealing and relaxation internal void morphology changes and as a result, the SAXS patters of annealed and relaxed samples are observed different. The effect of low temperature annealing and relaxation on restructuring the nanovoid as observed in high-quality 3D surface are also sensitive in 2D information through SAXS. The informations from value of $S(k \to 0)$ and r_g in reciprocal are observed consistent with the information from value of R_g, R_{gi} and α', $\beta'$and γ' in real space along with visualization of 3D void surface. An observed smaller $S(k \to 0)$ value at $f_v = 0\%$ and 0.3% in annealed samples than that of relaxed sample at same temperature suggest that, annealing produce

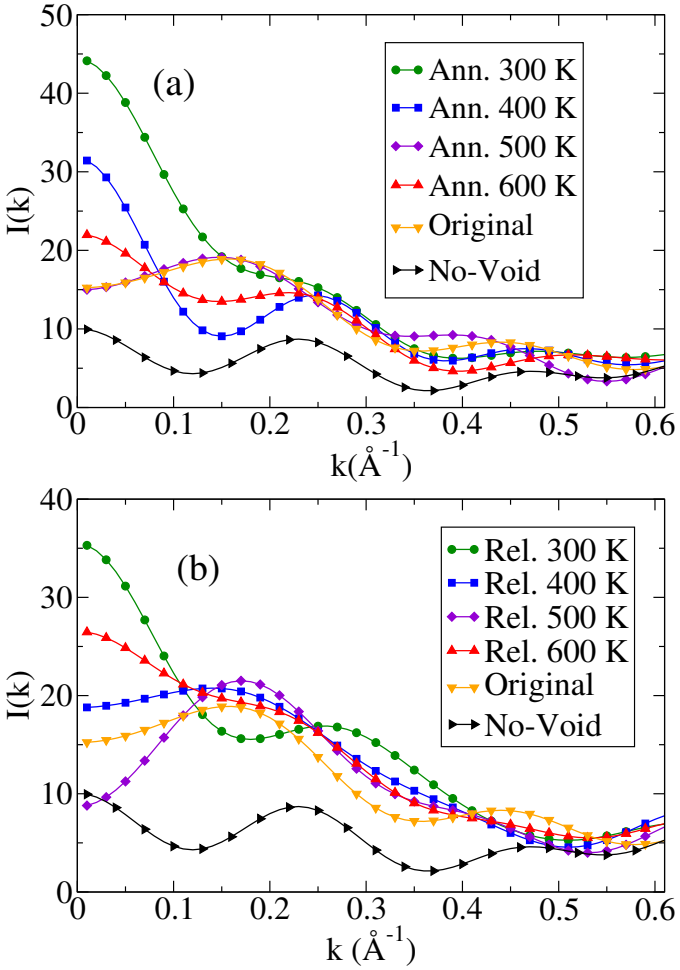

Figure 4.5: SAXS scattering intensity of annealed *a*-Si models (a) before and (b) after relaxation. Green, blue, purple and red color curve represent the corresponding scattering intensity at 300 K, 400 K, 500 K and 600 K respectively. For the comparison purpose, the scattering intensity of the original (yellow) and no void model (black) are also included.

more ordering, which is consistent with other simulation [175] and experimental [174] studies.

Chapter 5

Ab initio STUDY OF TEMPERATURE-INDUCED MICROSTRUCTURAL EVOLUTION OF VOIDS IN HYDROGENATED AMORPHOUS SILICON

In the previous chapter, we have observed the void structural change at low temperature annealing in classical model of *a*-Si. It is important to study how the classical results are changed in quantum mechanical treatment. For this purpose, the evolution of the void in classical molecular dynamics and *ab initio* molecular dynamics simulation are compared at low (300 K) and high (800 K) temperature in the absence of hydrogen. Additionally, the role of hydrogen in restructuring the surface and the hydrogen bonding configuration near the vicinity of void are discussed in hydrogen rich void in *ab initio* models of *a*-Si:H.

5.1 Introduction

Amorphous silicon and its hydrogenated counterpart have a wide range of applications, from photovoltaics to thin-film technology [4, 6]. Thin films of hydrogenated amorphous silicon (*a*-Si) are extensively used for passivation of crystalline silicon (*c*-Si) surfaces, which is essential to produce a high open-circuit voltage in silicon-based heterojunction solar cells [178–180]. Post-deposition annealing is routinely used for structural relaxation of *a*-Si:H samples and incorporation of hydrogen at the *a*-Si:H/*c*-Si interfaces. The presence of hydrogen to an extent thus is often preferred [181] for the preparation of *a*-Si:H samples with good interface properties. Experimental studies, such as spectroscopic ellipsometry [182, 183] and Raman spectroscopy [184] indicate that, although the presence of nanometer-size voids can degrade the electronic quality of the samples, a small concentration of voids can improve the degree of surface passivation. This is generally believed to be due to the presence of mobile H atoms in a void-rich environment, where hydrogen can reach *a*-Si:H/*c*-Si interfaces, via diffusion or other mechanisms, in comparison to dense *a*-Si:H samples.

Heat treatment or post-deposition annealing is an effective tool for nanostructural relaxation of laboratory-grown samples. Annealing at low to medium temperature (400 K-700 K) can considerably improve the quality of *as-deposited* samples by removing unwanted impurities and reducing imperfections (e.g., defects) in the samples [185]. For

amorphous materials, annealing also increases the degree of local ordering in amorphous environment. Earlier studies by small-angle X-ray scattering (SAXS) reported the presence of columnar-like geometric structure [186] and blister formation in annealed *a*-Si:H [187]. Experimental studies on *a*-Si/*a*-Si:H have also indicated that annealing above 673 K can lead to the formation of voids via vacancy cluttering, which affects the macrostructural properties of the network [188]. It has been suggested that at higher temperature, near 800 K, a considerable restructuring can take place near the voids boundary that can modify the shape and size of the voids. Although tilting SAXS [50] can provide some information on the geometrical shape of the voids, a direct experimental determination of annealing effects on the morphology of voids in the amorphous environment is highly nontrivial as scattering experiments generally provide integrated or scaler information on the size and shape of the voids. By contrast, computational modeling can yield reliable structural information on the morphology of voids [82, 84] provided that high-quality ultra-large models of *a*-Si/*a*-Si:H with a linear dimension of several nanometers are readily available and an accurate total-energy functional to describe the atomic dynamics of Si and H atoms is in place. However, despite numerous studies on computational modeling of *a*-Si and *a*-Si:H over the past several decades, there exist only a handful of computational studies 16-20 that attempted to address the structure and morphology of voids on the nanometer length scale in recent years.

The purpose of the work is to conduct *ab initio* MD simulation for void structure in realistic models of *a*-Si with and without the presence of hydrogen inside the voids at varying temperature. Specifically, we address the temperature driven microstructural evolution of the nanometer-size voids in model *a*-Si networks at 300 K and 800 K, which are characterized by a distribution of voids, as observed in small-angle X-ray scattering (SAXS) [39, 57], nuclear magnetic resonance (NMR) [58], infrared (IR) spectroscopy [59, 189], and positron annihilation spectroscopy (PAS) [61]. The three-dimensional shape of the nanometer-size voids are studied by using the convex- hull approximation [190] of the boundary region of the voids upon annealing at 300 K and 800 K. The presence of molecular hydrogen and the statistics of various hydrogen-bonding configurations in the vicinity of void surfaces are studied by introducing hydrogen atoms inside the voids with a density as observed in infrared and NMR measurements [48, 59].

The rest of the chapter is as follows. In section 5.2, a brief description of the simulation of ultra-large models of *a*-Si with a linear dimension of a few tens of nanometers and the generation of nanometer size voids in the resulting models in order to incorporate a realistic distribution of voids, with a void-volume fraction as observed in SAXS and IR measurements is presented. Results of the work, with particular emphasis on the three-

dimensional shape and size of the voids upon annealing at 300 K and 800 K, correlation between the three-dimensional shape and size of the voids with the SAXS intensity and the dynamics of hydrogen in the vicinity of the voids are discussed in section 5.3. In this section a comparison of the results from the positron-annihilation lifetime (PAL) spectroscopy [83] and Doppler-broadening positron-annihilation spectroscopy (DB- PAS) [191] are presented. Finally, conclusion of the work is presented in section 5.4.

5.2 Computational Method

5.2.1 Generation of ultra-large models of *a*-Si

Simulated, high-quality ultra-large model of *a*-Si generated by using classical molecular dynamics (MD) simulation in the canonical ensemble with the Stillinger-Weber inter-atomic potential [69, 70] used in this chapter is the same model as used in previous chapter. The characteristic properties of simulated model are; number of atoms, simulation length, density, an average bond length, an average bond angle, fourfold coordination and RMS fluctuation in bond angle are 262400, 176.1228 Å, 2.39 Å, 109.23°, 97.4 % and 9.26°respectively (Ref. 3.1). To obtain this realistic model, the configuration was annealed to a temperature of 1800 K and equilibrated at 10 *ps* at that temperature and then cooled to 300 K with cooling rate 30 K/*ps*. A equilibrium configuration at 300 K was optimized by total energy relaxation using the limited-memory BFGS algorithm [145, 146]. For the study of internal nanovoids, geometrical approach was used, where any change in characteristic properties were examined at low (300 K) and high (800 K) temperatures with and with out the present of H.

5.2.2 Geometrical approach for void

In this work, the nanosized voids were generated based on experimentally observed void-volume fractions [2, 50, 192, 193]. In NREL technical report, Williamson have reported that void fraction in *a*-Si:H ranges from 0.1%-1% but higher % are not preferable because of lower device quality. In *a*-Si prepared from magnetron sputtering technique and conjunction with the tilting SAXS measurement, University of Illionis group have reported that the corrected void fractions which ranges from ≈0.1% - 0.3% [2]. Our simulated void models were prepared at 0.2% void fractions which was with in experimentally reported value and device grade material.

An array of experimental studies; SAXS [38, 39, 57] 5 Å - 20 Å, NMR [58] 20 Å - 40 Å, SANS [53] 10 Å -12 Å, IR spectroscopy [59] and calorimetry [48, 49, 60] ≈ 40 Å and PAS [61] ≈ 20 Å were referred as the basis for the size of voids. With 0.2% void fraction,

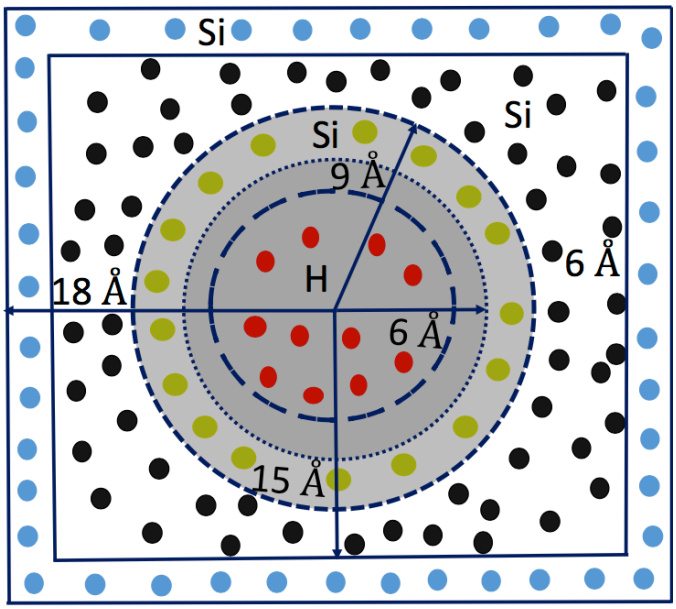

Figure 5.1: A schematic representation of a void (gray region) in two dimensions.The annular region with Si atoms (yellow circles) indicates the void boundary with a few H atoms (red circles) inside the void. The bulk Si atoms shown in black and blue circles are fixed for the purpose of local AIMD simulations, as discussed in the text.

we accommodate 12 artificially constructed void by removing Si atoms from the spherical region of 6 Å radii. The number density of the void in the system was $0.22\times10^{19}\text{cm}^{-3}$ corresponding to 12 representative voids. Individual voids were treated classically and quantum mechanically.

Particularly, we were interested in void shape and size, so the grafting approach help us to investigate an average void restructuring effect in bulk structure by bringing them back into the void network. Characteristic lengths chosen in the small model were shown in Fig. 5.1, where four different regions (i) void (H atom Red) (ii) interface (Si atom Green) (iii) boundary (Si atom black) and (iv) edge (Si atom blue) are shown. In each models, the void surface were characterized by tracking the void surface atoms around the void of 6 Å radii and 3 Å shell width. Such void surfaces were embedded in a cubical box of half-length 15 Å with additional 3 Å rigid edge boundary on either direction. So,12 small models have box length 36 Å and model sizes are ranging from 2180–2210. Having obtained an ultra-large model of *a*-Si, we proceed to generate a realistic distribution of voids. Since computational modeling of void formation in *a*-Si, by mimicking the actual deposition and growth processes, is highly nontrivial, we generated a void distribution using experimental information on the shape, size, and the number density of voids. Experimental data from an array of measurements, such as small-angle scattering (SAS)[38, 39, 53, 57], Infra Red (IR)

spectroscopy [59] nuclear magnetic resonance (NMR)[58] positron- annihilation lifetime (PAL) spectroscopy [61] and calorimetry measurements [48, 49, 60] suggest that the linear size of the voids in *a*-Si lies between 10 Å and 40 Å and that the void-volume fraction can range from 0.01%- 0.3% of the total volume, depending upon the growth process, deposition rate, and the consequent electronic quality of the samples. Following these observations, we constructed a void distribution in the ultra- large model with the following properties: a) The voids are spherical in shape and have a diameter of 12Å; b)The number density of the voids corresponds to a void-volume fraction of 0.2%; c) The voids are sparsely and randomly distributed, so that the distance between any two void centers is significantly larger than the dimension of the voids.

Figure 5.1 shows an example of a void embedded in a two- dimensional amorphous network. The void region is indicated by the gray circle of radius R_v, which is surrounded by a layer of Si atoms (yellow) with a thickness d. Silicon atoms in the layer constitute the surface/wall of the void, which we shall refer to as the void-surface atoms. The remaining Si atoms, within the cubic box (of length l), will be referred to as bulk Si atoms and are indicated as black and blue circles. To study the effect of hydrogen on the evolution of void surfaces, H atoms were introduced inside the voids so that no two H atoms were at a distance less than 1 Å from each other. The presence of H atoms in the network requires that the problem must be treated at the quantum-mechanical level using, for example, first-principles density-functional theory. However, given the size of the ultra-large model, such a task is hopelessly difficult and computationally unfeasible, and an approximation of some sort is necessary. Here, we employed the local approach to electronic-structure calculations by invoking the principle of nearsightedness of an equilibrium system, as proposed by Kohn [194] and address the problem by studying an appropriately large sub-system, defined by a cubical box of length l surrounding each void (see Fig.5.1). Following an (approximate) invariance theorem on electronic structure of disordered alloys, due to Heine and coworkers [195, 196] the quantum local density of states near the voids is essentially independent of the boundary conditions at a sufficient large distance, for example, the presence of a fixed layer of Si atoms on the edge of the box. Referring to Fig.5.1, we chose Rv =6 Å, d =3 Å, and l = 36 Å.

To study the effect of hydrogen on void surfaces, each void was loaded with 30 H atoms, as observed in IR and NMR measurements. *Ab initio* calculations and total-energy optimization were conducted using the first-principles density-functional code SIESTA [197]. The latter employs a localized basis set and norm-conserving Troullier-Martins pseudopotentials [198] which are factorized in the Kleinman-Bylander [199] form to remove the effect of core electrons. Electronic and exchange correlations between electrons are handled using the

local density approximation (LDA), by employing the Perdew-Zunger parameterization of the exchange-correlation functional [200]. Since a fully self-consistent-field solution of the Kohn-Sham equations, consisting of more than 2000 atoms, is computationally very demanding, particularly to conduct MD simulations for a period of 10 picoseconds, we employed the Harris-functional approach [201, 202] that involves linearization of the Kohn-Sham equations. The accuracy and computational efficiency of the Harris-functional approach to treat *a*-Si and *a*-Si:H systems are well-documented in the literature [203]. Single-zeta (SZ) and double-zeta-polarized (DZP) basis functions were employed for Si and H, respectively. Here, SZ functions correspond one s and three p orbitals for Si atoms, where as DZP functions refer to two s and three d orbitals for H atoms. The size of the simulation box is large enough in this work so that the Brillouin zone (of the supercell) collapses into the point, which was used for the Brillouin zone sampling.

5.2.3 Simulation of SAXS

The structure factor of binary system is the function of partial structure factor, which is also the function of the pair correlation function [204–206]. The reduced radial distribution function ($G_{ij}(r)$) is the function of partial pair coronation function $g_{ij}(r)$, defined as, $G_{ij}(r) = 4\pi\rho_{ij}[g_{ij}(r)-1]$, ρ_{ij} is the number density of atom. The wave vector $\vec{k}$ is the difference between the scattered ($\vec{k}'$) and incident ($\vec{k}_0$) wave vectors. i.e ($|\vec{k}'$ -$\vec{k}_0)|$ =$4\pi\sin\theta/\lambda$, where 2θ and λ are scattering angle and wavelength of X-radiation.The SAXS intensity for a binary system can be expressed with the aid of the partial structure factors and the atomic form factors of the constituent atoms. Following Cusack [126, 127] the scattering intensity, $I(k)$, is estimated as, [Ref. Eq.(2.28)],

$$\begin{aligned}\frac{I(k)}{N} = F(k) = f_\alpha^2(x_\alpha x_\beta + x_\alpha^2 S_{\alpha\alpha}) + f_\beta^2(x_\alpha x_\beta \\ + x_\alpha^2 S_{\beta\beta}) + 2f_\alpha f_\beta x_\alpha x_\beta (S_{\alpha\beta}-1)\end{aligned} \tag{5.1}$$

where, $x_\alpha = \frac{N_\alpha}{N}$, $x_\beta = \frac{N_\beta}{N}$ are atomic fractions and f_α and f_β are form factors of α and β atoms and S_{ij} is the partial structure factor defined as,

$$S_{ij} = 1 + 4\pi\rho_0 \int_0^\infty (g_{ij}(r)-1)\frac{\sin kr}{kr} r^2 dr \tag{5.2}$$

$g_{ij}(r)$ is the partial pair distribution function and $G_{ij}(r) = 4\pi\rho_{ij}[g_{ij}(r)-1]$ reduce radial distribution function. $\rho_0 = N/V$ is the number density of atom.

The size of the void were estimated by calculating the radius of gyrations of spatial distribution of void surface atoms, using the Guinier and convex hull approximation. Once

the scattering intensity is available, either numerically or experimentally, the size of the voids, or any extended inhomogeneities, can be estimated by invoking the Guinier approximation in the small-angle limit, k $r_g \leq 1$,

$$I(k) = I(0)exp(\frac{-k^2 r_g^2}{3}) \tag{5.3}$$

In small k region,

$$lnI(k) = lnI(0) - \frac{-k^2 r_g^2}{3} \tag{5.4}$$

This is a straight line with negative slope ($= r_g^2/3$), which gives Guinier's radius as,

$$r_g = \sqrt{3 \times slope} \tag{5.5}$$

$$R_H{}^2 = \frac{1}{n_H} \sum_{j=1}^{n_H} (r_j - \bar{r}')^2 \tag{5.6}$$

where R_g, R_H and r_g are calculated radius of gyration for all surface atoms, hull radius of gyration and and Guinier radius respectively. n_{sa} and n_H are the total surface atoms and hull atoms respectively. $lnI(k)$ and $lnI(0)$ are SAXS intensities at an arbitrary arbitrary (k) and very small ($k \to 0$) wave vectors respectively. For the measurement of the degree of reconstruction, slope parameter "sphericity" of the spherical void is examined. Sphericity of spherical void is defined as,

$$\Phi_S = \frac{\pi^{\frac{1}{3}} (6V_H)^{\frac{2}{3}}}{A_H} \tag{5.7}$$

where V_H and A_H are hull volume and surface area of the void respectively. The definition above is frequently used to measure the shape and roundness of sedimentary quartz particles, and it expresses the ratio of the surface area of a sphere to that of a non-spherical particle having an identical volume [207]. It may be noted that a highly distorted void may not be accurately represented by a convex polyhedron and that the convex-hull volume provides an upper bound of the actual void volume, leading to $R_H > R_g$. r_g is the characteristic size of the inhomogeneities in the dilute concentration limit, which provides a reasonable estimate of void sizes from experimental data, difficulties arise in extracting the r_g value from a $lnI(k)$ vs k^2 plot in simulations, owing to the finite size of the models. Since the effective small-angle region of k is approximately given by $4/L < k < 1/r_g$, where L is the linear dimension of the sample, a sufficiently large model is needed in order to obtain the mean value of r_g via averaging over several independent configurations. However, it has been observed that, even for very large models, the lower limit of k cannot be reduced arbitrarily

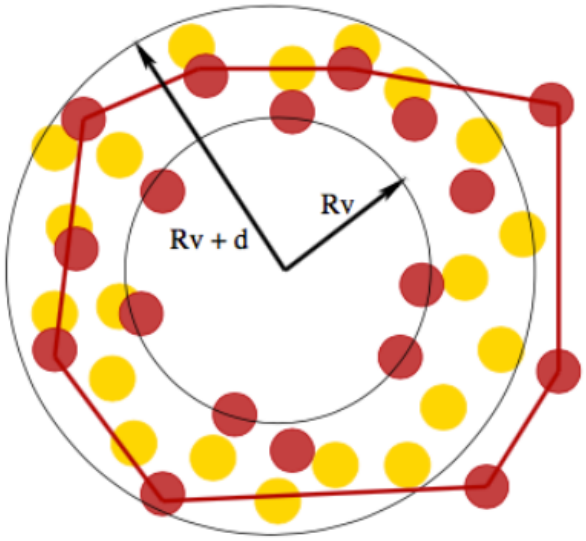

Figure 5.2: A schematic representation of the void in two dimensions showing the characteristic lengths associated with void. Void radius, void shell width, boundary width and edge width are 6, 3, 6 and 3 Å respectively. Hydrogen are initially introduced inside spherical void region of 4 Å radius.

by increasing L due to the presence of noise in $rg(r)$ beyond $\approx$ 25-30 Å.The term $r(g(r)-1)$ in Eq. (5.2) for $r > 25$ Å introduces artifacts in $S(k)$ for small values of k, which make it difficult to accurately compute r_g from the simulated intensity data. This necessitates the construction of alternative measures of void sizes and shapes directly from the distribution of atoms in the vicinity of voids. A simple but effective measure is to compute the gyrational radius from the distribution of the atoms on void surfaces between radii R_v and $R_v + d(= R')$, where R_v is the void radius and d is the width of the void surface, as discussed in earlier section. A schematic diagram to illustrate void reconstruction is presented in Fig.5.2, where the positions of the void-surface atoms before and after annealing are shown in yellow and red colors, respectively. The atoms on the reconstructed surface are distributed within a spherical region of radius $R'_v + x$ and $H[y]$ is the Heaviside step function that asserts that only the atoms with $y > 0$ contribute to R_g. Assuming that the void-surface atoms (yellow) can displace, in the mean-square sense, from their initial position by x during annealing, the radius of gyration, R_g, for the assembly of void atoms (red) can be expressed as, Radius of gyration calculation formula follows as,

$$R_g{}^2 = \frac{1}{n_{sa}} \sum_{i=1}^{n_{sa}} (r_i - r_{cm})^2 H[R'_v + x - r_i] \tag{5.8}$$

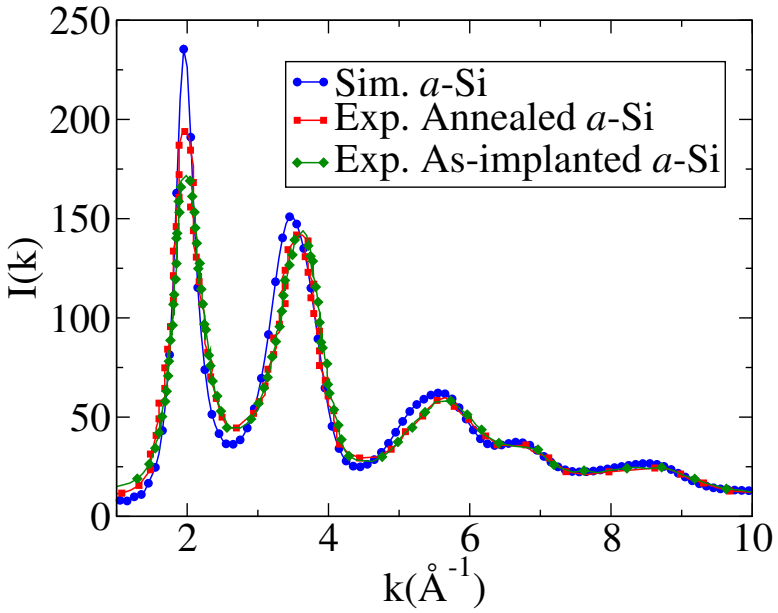

Figure 5.3: Scattering intensity of a-Si. Blue, red and green color represent the simulated, experimental annealed and experimental as-implanted a-Si Ref.[3].

Here, r_i and r_{cm} are the position of the i^{th} atom and the center of mass of n_{sa} void-surface atoms, respectively. The atoms on the reconstructed surface are distributed within a spherical region of radius $R'_v + x$ and $H[y]$ is the Heaviside step function that asserts that only the atoms with $y > 0$ contribute to R_g. Following Ref.[85], we chose a value of x =1.5Å for Si atoms in order to define the boundary of a reconstructed void surface. Since annealing at high temperature can introduce considerable restructuring of void surfaces, it is often convenient to invoke a suitable convex approximation to estimate the size and shape of the voids. Here, we employ the convex-hull approximation that entails constructing the minimal convex polyhedron that includes all the void-surface atoms on the boundary. The size of the convex region can be expressed as the radius of gyration of the convex polyhedron, or convex hull. In Eq. (5.6), n_H is the number of atoms (or vertices) that defines the convex polyhedral surface, and r_h is the center of mass of the polyhedron.

5.3 Results and Discussion

Before addressing the temperature-induced nanostructural changes in voids, we briefly examine the ultra-large model of a-Si, developed in section (5.2), in order to validate its structural properties. Figure,5.3 shows the simulated values of the X-ray scattering intensity, along with the experimental values of the intensity for as-implanted (green) and annealed (red) samples of pure a-Si, reported by Laaziri *et al.*[3]. The simulated values closely match

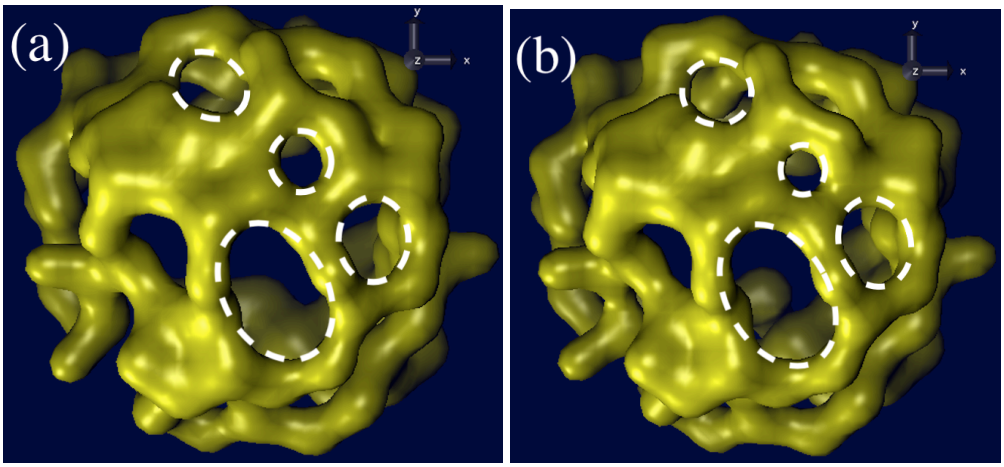

Figure 5.4: 3D void surfaces of a representative void V3 in (a) CMD-R and (b) AIMD-R model at 300 K. The dotted white marks indicates the change in surface from the top view. The number of Si atoms contributing surface are 105 in both CMD-R and AIMD-R models.

with the experimental data in Fig.5.3, especially for the annealed samples, in the wide-angle region from 1Å to 10 Å and beyond.

Together with the X-ray intensity, the average bond angle and its deviation,109.23 $\pm$ 9.26, and the number of four-fold-coordinated atoms, 97.6%, suggest that the structural properties of the model obtained from classical molecular-dynamics simulations in section 5.3 are consistent with experimental results. It may be reasonably assumed that the presence of a small amount of coordination defects (2.4%), which are rather sparsely distributed in the amorphous environment, would not affect the scattering intensity appreciably in the small-angle region of the scattering wave vector.

5.3.1 Void structure evolution at 300 K in *a*-Si

In this section, we discuss the three-dimensional shape and size of the voids in pure *a*-Si obtained from classical and quantum-mechanical annealing of the system at 300 K followed by total-energy optimization. Starting with an examination of the classical and *ab initio* generated surface structures of the voids, we analyze the SAXS spectrum obtained from the ultra-large model, embedded with the voids annealed at 300 K. Figure 5.4(a) and 5.4(b) shows the structure of a representative void V3 after thermalization at 300 K for 10 *ps*, using classical and *ab initio* MD simulations. A close examination suggests that the resultant structures are very similar to each other as far as the void surfaces are concerned, except for small changes as indicated. A similar observation has been made for the remaining voids as well, which showed very little changes on the void surfaces.These results are consistent with the variation of the simulated intensity shown in Fig.5.5(a). A some what more pronounced

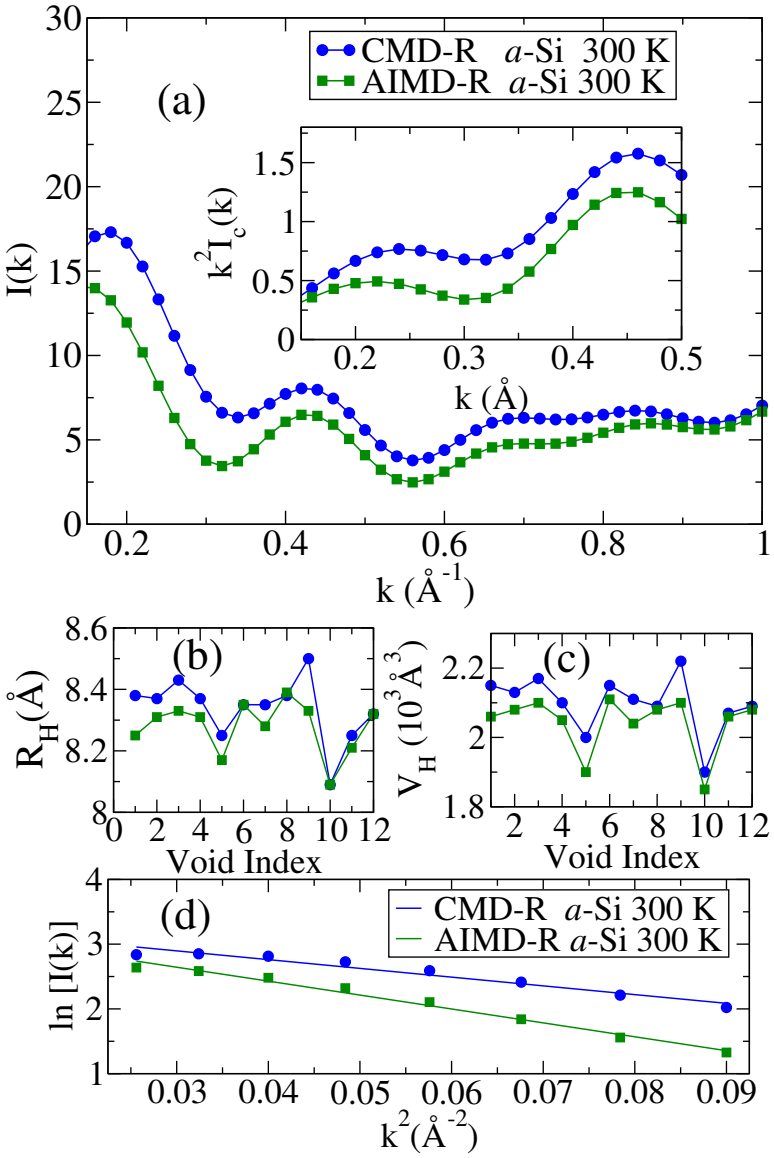

Figure 5.5: (a) Scattering intensities and corresponding Kratky plots inset figure for CMD-R (blue) and AIMD-R (green) *a*-Si at 300 K. (b) Convex hull radius of gyration of CMD-R (blue) and AIMD-R(green). (c) Estimated hull volumes of corresponding void surface atoms. (d) Guinier plots of CMD-R and AIMD-R models with Guinier's fit radius of gyration 6.38 Å and 8.07 Å respectively.

scattering from the classical voids (CMD-R) in comparison to the *ab initio* voids (AIMD-R) can be attributed to a minor expansion of the voids during classical simulations.This is clearly evident from Figs.5.5(a) and 5.5(b), 5.5(c) and 5.5(d) where the radius of gyration and the volume of the voids, respectively, are obtained from the convex-hull approximation of the void region.

The polyhedral radii (R_H) for the voids from classical simulations were found to be

consistently larger than the corresponding radii from *ab initio* simulations in Fig.5.5(b). A similar conclusion applies to polyhedral volumes (V_H), which are plotted in Fig.5.5(c). Once the linear size, area, and volume of the voids are available in the convex approximation, the sphericity of voids Φ_S, can be determined from Eq.(5.7). A further measure of the size of the voids follows from the variation of the SAXS intensity, $I(k)$, with the wave vector, k, in the small-angle region. Kratky plots inset Fig,.5.5(a), shows the voids structure in both CMD-R and AIMD-R model are almost identical at low temperature 300 K. By invoking the Guinier approximation (see Eq.(5.3), the Guinier radius, r_g, can be obtained from ln $I(k)$ vs. k^2 plots. Figure 5.5(d) shows the Guinier fits in the wavevector range, $0.15 \leq k \leq 0.3$ Å^{-1} , which resulted in an r_g value of 6.38 Å for the CMD-R model and 8.07 Å for the AIMD-R model. It should suffice to mention that the computation of the Guinier radius, r_g, is affected by the limited data in the small-angle region of the intensity spectrum and thus it may vary from the estimate obtained from the convex approximation. Having studied the surface structure of voids at 300 K.

5.3.2 Void structure evolution in *a*-Si at 800 K

In this section, high temperature (800 K) annealing effect on void morphology are investigated by using same models. There are significant structural changes in void morphology which are explained with the 3D geometry and the corresponding SAXS intensities. At the high temperature of 800 K, significant restructuring of void surfaces is happened that affects the SAXS intensity and void sizes. Further, it will be apparent that the results from classical and quantum-mechanical simulations vary considerably at 800 K. Figures 5.6(a) and 5.6(b) show the shape of a representative void V3 after annealing at 800 K from classical and *ab initio* MD simulations. A comparison between the two structures in Figs.5.6(a) and 5.6(b) shows the regions on the two surfaces with a varying degree of reconstruction.

The shape of the respective void surfaces obtained from using the convex-hull approximation is shown in Figs.5.6(c) and 5.6(d). Table 5.1, lists some of the parameters that characterize the void geometry in terms of the convex-hull radius (R_H), the radius of gyration of void-surface atoms (R_g) and the Guinier radius (r_g), the hull volume (V_H), and the average sphericity of the voids ($\bar{\Phi}_s$) after annealing at 300 K and 800 K. Although these scalar parameters do not vary much in the convex approximation, it is evident from Figs.5.6(a) and 5.6(b) that classical results differ noticeably from *ab initio* results, indicating the limitation of the classical force field in describing the restructuring of void surfaces at high temperature, namely at 800 K. This observation is also reflected in Fig.5.7, where the simulated values of the intensity of SAXS at 800 K, the convex-hull radii and the volumes of the voids are

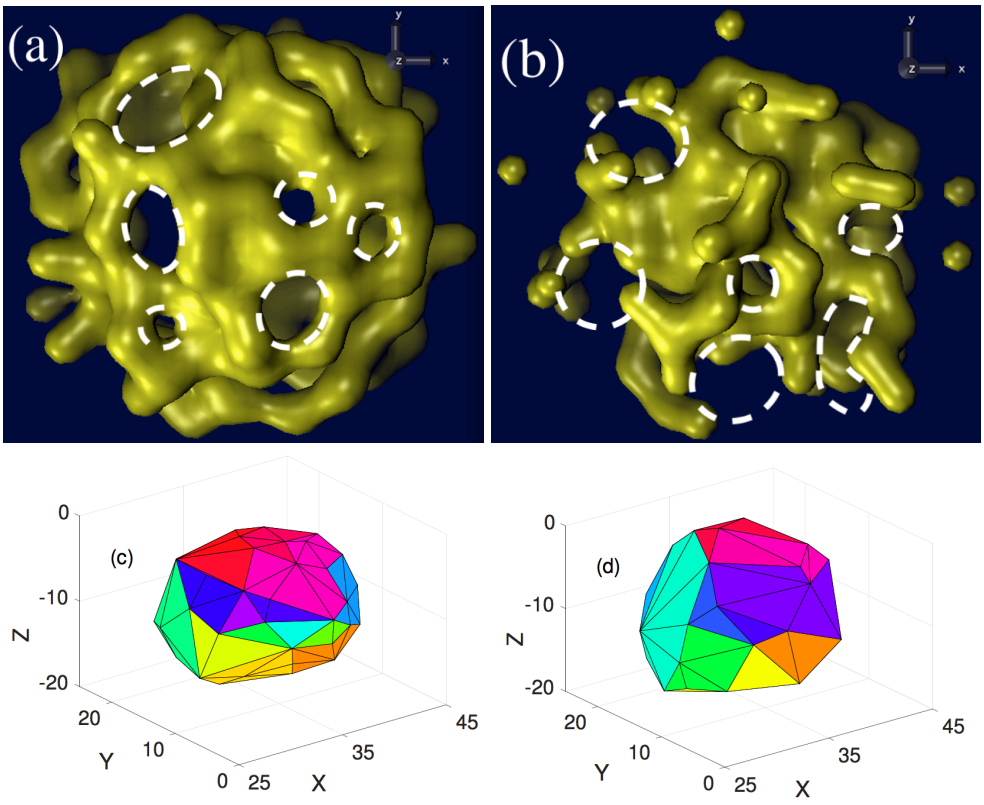

Figure 5.6: 3D void surface of a representative void V3 (a) CMD-R (b) AIMD-R model at 800 K. The dotted white marks indicates the change in surface from the top view. The number of Si atoms contributing surface are 105 and 103 in CMD-R and AIMD-R respectively. (c) and (d) convex hull of the respective voids. Number of hull atoms in CMD-R AND AIMD-R are 49 and 32 respectively.

shown for each void. Like wise at 300 K, SAXS intensity from CMD-R model is stronger than that from AIMD-R model in small-angle limit $0.15 \leq 0.55$ Å^{-1}. The Kratky plots inset figure 5.7(a) are also consistent. An observed strong SAXS intensity could be associated with either bigger size void. As, we have seen that in AIMD-R model, hugely breaking of void wall creating smaller size multiple voids from a single bigger void. This effect is reflective in SAXS leading strong signal from a less purtrubed bigger void.

The hull radius and volume of AIMD-R models are higher at high temperature than that of CMD-R models. Hull surfaces of the same representative void are shown in Fig.5.6(c) and (d), where hull surface of AIMD-R void is slightly stretched out as compared to that of CMD-R. In an average n_H, $\bar{\Phi}_S$, V_H and R_H value changed in AIMD-R models are $\approx$ 33%, 7.9%, 8% and 4% respectively as compare to CMD-R models. In table 5.1 average value of those parameters are listed. Most of the original void surface atoms collapse and they occupy the cavity, few of atoms leave the 4.5Å boundary and coordinate with rest

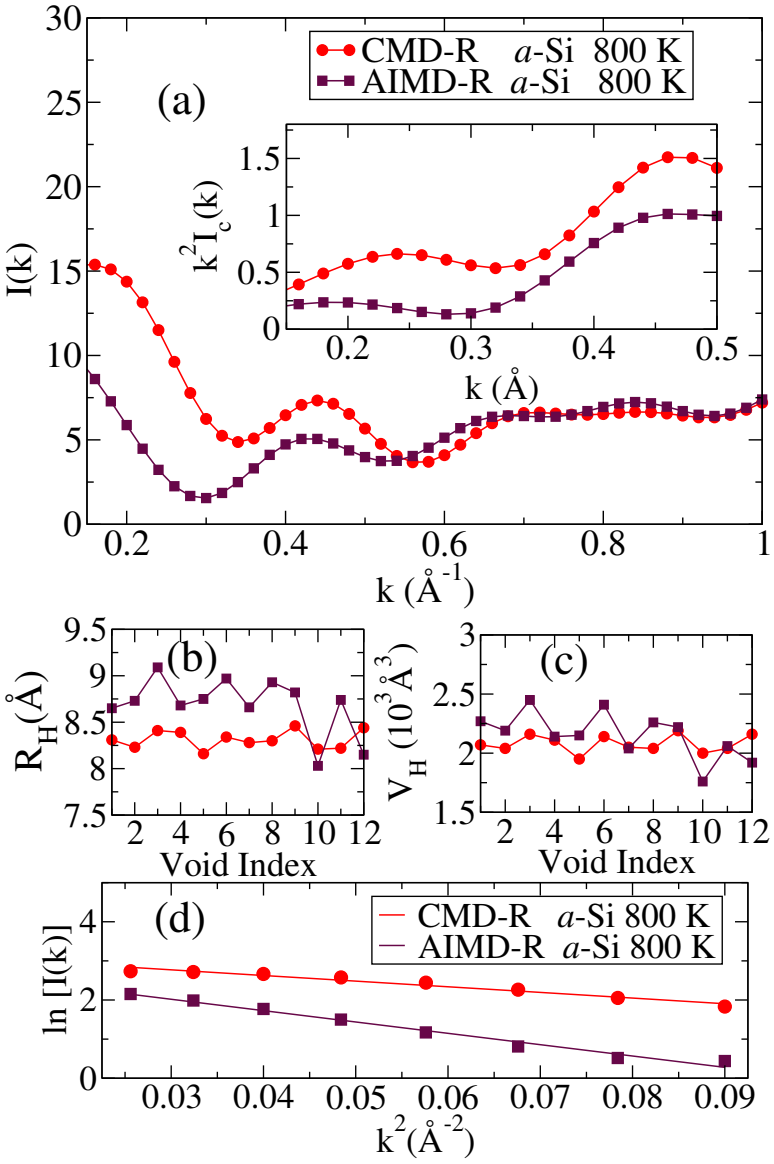

Figure 5.7: (a) Scattering intensities and corresponding Kratky plots for CMD-R (red) and AIMD-R (marron) *a*-Si at 800 K. (b) Convex hull radius of gyration of CMD-R (red) and AIMD-R (marron). (c) Estimated hull volume of corresponding void surface atoms in CMD-R and AIMD-R voids at 800 K. (d) Guinier's plots of CMD-R and AIMD-R models at 800 K with Guinier's fit radius of gyration 6.57 and 9.48 Å respectively.

bulk atoms and few of atoms spread inside the boundary and coordinate with boundary atoms. Due to majority of collapsing atoms and few spread (not bonded atoms) create the void surface which appeared highly changed and comparatively occupied more inner empty cavity leaving the open volume in the network. This is an evidence of calculated lower R_g value and lesser hull atoms. In R_H calculation those atoms who lies inside and outside cut off are not considered. In Fig.5.7 (a), SAXS intensity of AIMD-R model (marron curve) is

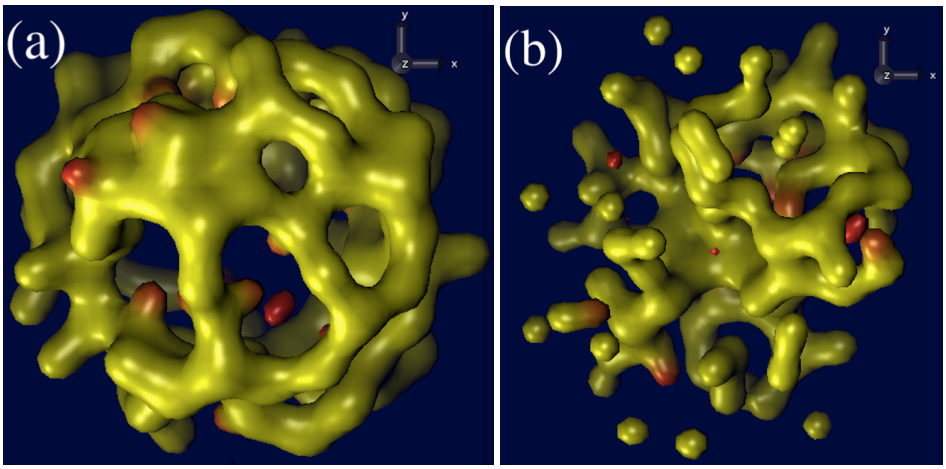

Figure 5.8: The structure of a representative void surface (V3) from AIMD simulations in the presence of H atoms inside the cavity at: (a) 300 K; and (b) 800 K. The yellow and red blobs represent Si and H atoms, respectively. For visualization, an identical set of surface parameters was used for rendering.

observed more smoother than that of CMD-R model at 800 K, this is due the the partially collapsing of the void at 800 K. Kratky plot in inset Fig.5.7(a) is consistent with collapsing or folded surface behavior in AIMD-R models.

5.3.3 Structural evolution of hydrogen-rich voids in *a*-Si

In above section, we have seen that annealing at 800 K can introduce considerable restructuring of void surfaces in pure *a*-Si, which is readily reflected in the three-dimensional shape and size of the voids but may not be apparent from one- dimensional SAXS intensity plots. Here, we shall examine how and to what extent the structural evolution of void surfaces can be affected in the presence of H clusters inside the voids. Small-angle X-ray scattering measurements on hot-wire chemical vapor deposition (HWCVD) films indicate that the presence of preexisting H clusters can affect the nanostructure of voids due to H_2 bubble pressure in the cavities, which, upon total energy minimization and strain relaxation, can lead to geometric changes, as observed via tilting SAXS and surface transmission electron microscopy (STEM) [50]. Although the degree of such nano- structural changes depend on the growth mechanism and the rate of film growth, it is instructive to address the problem from a computational view point using CRN models of *a*-Si, which are characterized by an experimentally consistent void volume faction and clusters of H atoms inside the voids.

Figures 5.8(a) and 5.8(b) show the structure of a hydrogen-rich nanovoid surface of the same representative void V3 obtained after annealing at 300 K and 800 K, followed by total-energy minimization. The evolution of Si and H atoms during annealing was described

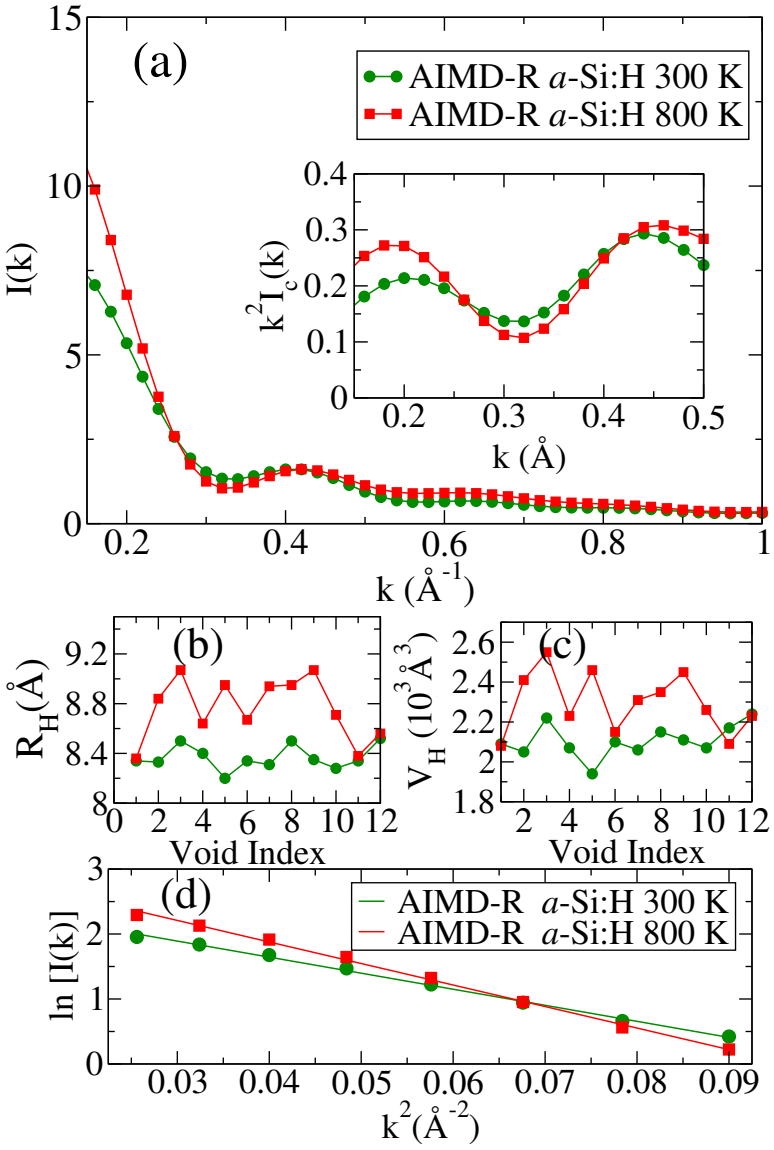

Figure 5.9: (a) Scattering intensities and corresponding Kratky plots in AIMD-R models of *a*-Si:H at 300 K (green) and 800 K (red). (b) Radius of gyration each AIMD-R voids at 300 K and 800 K in convex approximation. (c) Estimated hull volume of corresponding voids. (d) Guinier's plots for SAXS intensities in AIMD-R models of *a*-Si:H at 300 K and 800 K, where the radius of gyration are 8.66 Å and 10.01 Å respectively.

using *ab initio* density-functional forces and energies, from the local basis DFT package SIESTA [197]. The procedure to conduct such AIMD simulations of voids, which are embedded in an ultra-large model of *a*-Si, has been described in method section.

It is evident from Figs.5.8(a) and 5.8(b) that the thermalization of the void (V3) and its neighboring region at 300 K does not introduce notable changes on the void surface, with the exception of the distribution of H atoms. The initial random distribution of H atoms,

which was confined within a radius of 4 Å from the void center, evolved to produce several monohydrides (SiH) and a few dihydrides (SiH_2), along with a few H_2 molecules inside the cavity. The majority of H atoms continue to stay near the void at 300 K. By contrast, a considerable number of Si and H atoms have been found to be thermally driven out of the void region at 800 K. An analysis of the distribution of Si atoms (yellow) on the void surface and H atoms (red) inside the void reveals that approximately 12.4% of the original Si atoms and 23.3% of the H atoms left the void region of radius 10.5 Å after annealing at 800 K. This is evident from the surface plot, obtained from the Gaussian superposition of the atomic positions of the void-surface atoms (of V3) at 800 K, which are shown in Fig. 5.8(a) and 5.8(b). This observation has been found to be more or less true for most of the other voids. On average, approximately 8.3% of the Si atoms and 16.1% of the H atoms were found to leave the void regions at 800 K. By contrast, the corresponding average values at 300 K for Si and H atoms are 0% and 2.5%, respectively.

To get the bulk structural property of H rich *a*-Si void, SAXS intensities from grafted *ab initio* relaxed models at 300 K and 800 K were examined. In presence of H, smoother SAXS intensities in small-angle region are observed at 300 K. A highly distorted 3D void surface at 800 K shown in Fig.5.8(b) corresponds to relatively strong SAXS intensity in Fig. 5.9(a). Kratky plots in inset figure Fig.5.9(a) shows that voids are splitting in to smaller size voids. Also, k^2I_c peak values are at slightly two different locations, signifies the change in shape of the void at two temperatures. An average value of R_H, V_H and r_g are increase by $\approx 5\%$, 8% and 15% respectively on annealing the H rich void at 800 K as compare to that at 300 K. Higher degree of sphericity at high temperature signifies that, majority of Si lie inside the cavity. During the process, individual void volume increases leading larger size void in specific regions but total void volume fraction in the system decreases. Reconstruction in terms of crash and collapse and release of atoms are responsible to increase individual void volume which is consistent with experimentally observed result in tilting experiment [50] by Williamson *et al.*

To obtain the linear size of the voids, we computed the radius of gyration, R_g, using Eq.5.8. Likewise, the convex-hull approximation of a void region, defined by a set of void-surface atoms, provides the radius of the convex polyhedron, R_H , from Eq. 5.6. Figures 5.9(b) and 5.9(c) show the values of R_H and the corresponding hull volumes,V_H, of 12 voids, each of which has been computed upon annealing and geometry relaxation via AIMD simulations. The R_g and R_H values obtained from the real-space distribution of the void atoms are listed in Table 5.1. The apparent deviation of R_H from R_g can be readily attributed to the fact that the computation of R_g involves all the atoms on the surface and interior regions of the voids, whereas the convex-hull approximation includes only those atoms on

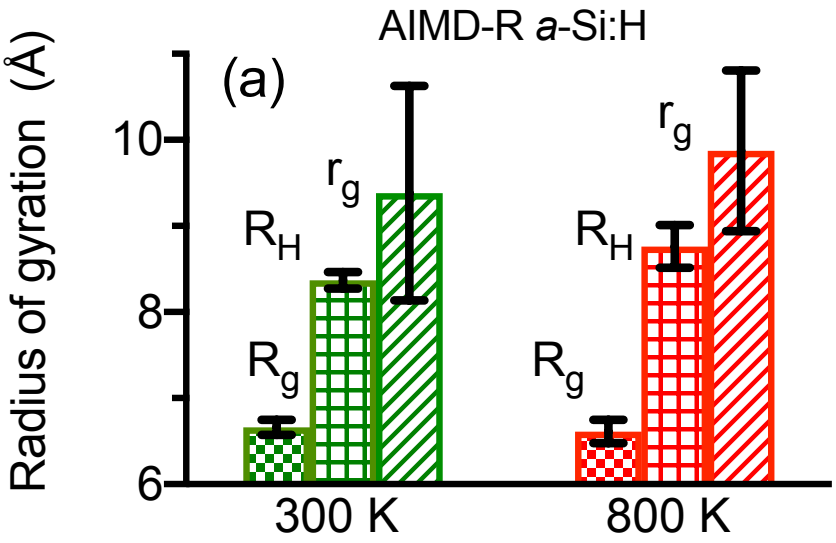

Figure 5.10: Average radius of gyrations; calculated (R_g), hull (R_H) and Guinier (r_g)) for hydrogen rich voids at 300 K and 800 K in *a*-Si with their respective error bars.

the void-surface region that defines a minimal convex surface. Thus, R_H provides an upper bound of the radial size of the voids.

In order to compare R_H and R_g values with the linear size of the voids from the simulated intensity plots in SAXS, we have invoked the Guinier approximation to estimate the Guinier radius, r_g, from $lnI(k)$-k^2 plots, as shown in Fig.5.9(d). Table 5.1 suggests that the r_g values obtained from the simulated intensity plots match closely with the corresponding average values of R_H at 300 K and 800 K. It may be noted that, while the intensity plot in Fig. 5.9(a) is not particularly sensitive to the shape of the voids, the slightly pronounced scattering in the region $k^2 = 0.06$ Å^{-2} is possibly indicative of the expansion of the void volume, as observed in the convex-hull volume in Fig.5.9(c). The exact cause of this increased scattering intensity is difficult to determine but it appears that a combination of the pressure due to H_2 bubbles, surface roughening of the voids, and the displacement of the atoms on the void surfaces at high temperature could lead to this additional scattering. This observation is corroborated by the results from a small-angle X-ray scattering study of nanovoids in HWCVD amorphous Si films that indicated an increase of individual void volumes upon annealing at 813 K.

Figure, 5.10 shows a comparison of the radius of gyrations at low and high temperature in the presence of H around the void, where at high temperature role of hydrogen dynamics in restructuring the void can be depicted. This observation is supported by an observed low R_g value at high temperature. Si atoms around the void surface loop loose their coordination and collapses partially occupying the cavity which lies close the the void center and contribute

Table 5.1: Average void parameters in *a*-Si *a*-Si:H models at low temperature. R_g (Å), $R_s = \sqrt{\frac{5}{3}}R_g$ (Å), R_H (Å), r_g (Å), V_H (Å^3) and $\bar{\Phi}$ calculated radius of gyration, hull radius of gyration, Guinier radius of gyration, hull volume in ($\times 10^3$) Å^3 and sphericity respectively.

Models	R_g	R_s	R_H	r_g	$V_H(\times 10^3)$	$\bar{\Phi}_S$
		a-Si				
CMD-R 300 K	7.60	9.80	8.34	6.38	2.1	0.66
AIMD-R 300 K	7.55	9.74	8.28	8.07	2.04	0.67
CMD-R 800K	7.56	9.75	8.31	6.57	2.08	0.63
AIMD-R 800 K	6.84	8.82	8.67	9.48	2.25	0.68
		a-Si:H				
AIMD-R 300K	6.66	8.59	8.36	8.66	2.12	0.56
AIMD-R 800 K	6.61	8.53	8.76	10.01	2.29	0.71

low R_g value. On the other hand high hull radii at that temperature signifies movement of Si/H outside the cavity providing significant change in void structure. An observed higher Guinier radius of gyration is associated with the relatively stronger SAXS signal due to the dynamics of the H around the void. As, the r_g calculation was done in same k range 0.15-0.3 Å^{-1} but it is configuration dependence, higher error bar for r_g value associate with that. A relatively higher error bar in R_g and R_H at high temperature shows that degree o reconstruction of different void configuration are different.This means that in amorphous network, at different void location, void size and shape can be different.

5.3.4 Hydrogen dynamics near voids in *a*-Si

In this section, the dynamics of hydrogen atoms in the vicinity of void surfaces from *ab initio* simulations are discussed. Since the mass of H atoms is significantly smaller than Si atoms, the motion of H atoms is more susceptible to the annealing temperature and, more importantly, to the resulting temperature-induced structural changes on the void surfaces. This is particularly noticeable at high temperature. Having established earlier that the structural changes on the void surfaces are more pronounced at 800 K, we shall now examine the character of the atomic dynamics of hydrogen inside (and near the surface of) the voids at 800 K. Despite the limited timescale of the present *ab initio* simulations, spanning 10 *ps* only, it is reasonable to assume that, at high temperature, the dynamical character of hydrogen motion inside the voids would be reflected in the first several picoseconds.

Figure 5.11, depicts the time evolution of hydrogen atoms at 800 K within two voids, V12 and V7. Initially, all hydrogen atoms were uniformly distributed inside the voids within a radius of 4 Å from the center of the voids (Ref. Fig.5.1). The mean-square displacements

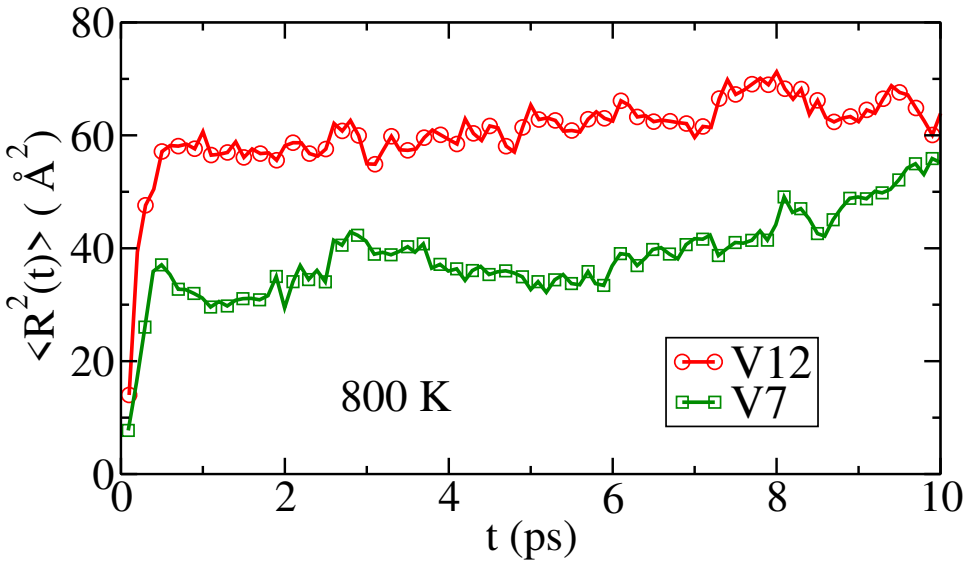

Figure 5.11: The time evolution of the mean-square displacements (MSD) of H inside two voids, V12 (red) and V7 (green), at 800 K. The difference between the two sets of MSD values can be attributed to the degree of void-surface reconstruction.

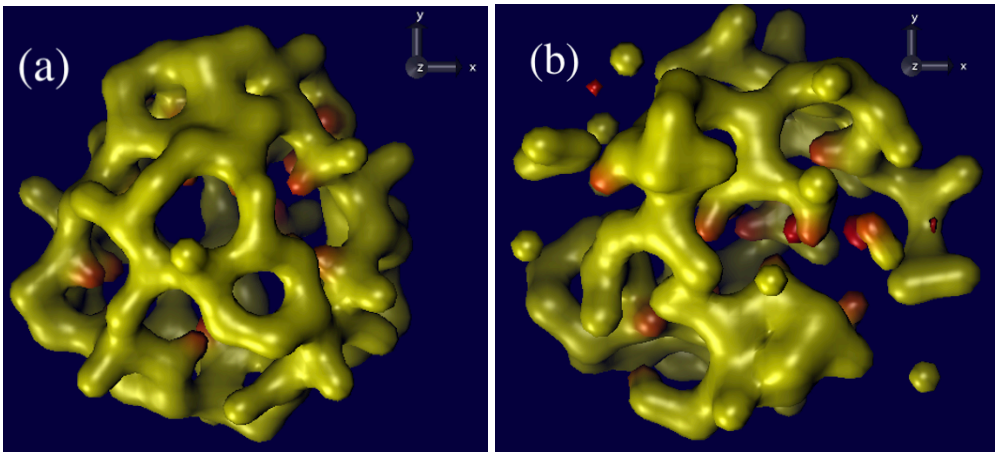

Figure 5.12: Hydrogen-induced surfaces at 800 K corresponding to mean-square displacements (MSD) of H inside two voids shown in 5.11. (a) The compact or smooth structure of V12 surface compared to a relatively fuzzy or scattered distribution of Si atoms in (b) V7 at 800 K.

(MSD), $<R^2(t)>$ of hydrogen atoms averaged over all H atoms in the respective void are shown in Fig.5.11 from 0 to 10 *ps*. The corresponding real- space distributions of Si and H atoms on the void surfaces and their immediate vicinity are also shown in Fig.5.12(a) and 5.12(b) for V7 and V12, respectively. The difference between the two sets of MSD values can be understood by taking into account the real-space structure of the void surfaces. In addition to the trivial thermal and configurational fluctuations caused by temperature and

the disorder in H distributions, respectively the motion of H atoms is also affected by the varying degree of restructuring of Si atoms on the void surfaces. The surface structure of V7 can be seen to be more open compared to its counterpart in V12, as shown in Figs.5.12(a) and 5.12(b), respectively. This has been also confirmed by analyzing the distributions of void-surface atoms in the interior of V12 and V7. The presence of Si atoms inside V7 reduces the effective diffusion rate of H atoms, due to additional scattering from interior Si atoms, in their early time evolution. By contrast, the less open or compact void surface of V12, with few Si atoms inside, provides less resistance to H atoms during their early evolution.Thus, hydrogen diffusion in V12 proceeds almost uninterruptedly, in the presence of few Si atoms from void surfaces, leading to a notable difference in their MSD values during the first several picoseconds of simulations. This observation has been found to be true for other pairs of voids for which a notable difference in the MSD values exists.

5.3.5 Hydrogen-bonding configurations near voids

Experimental data from positron-annihilation lifetime (PAL) spectroscopy [83] Rutherford backscattering spectrometry (RBS)[86] and Fourier-transform infrared spectroscopy attenuated total reflection (FTIR-ATR) [86] indicate that bonded and non-bonded hydrogens play an important role in characterizing the structural and optical properties of *a*-Si:H. Sekimoto et al. [83, 86] recently demonstrated that the presence of non-bonded hydrogens (NBH) beyond 2.8 at.% in amorphous silicon networks led to changes in the vacancy-size distribution and induced formation of nanometer-size voids in the network via relaxation of internal stress.

The presence of H_2 molecules and their evolution can be probed by an analysis of the low-temperature (LT) peak of the hydrogen-effusion profile [83, 208, 209] near 750 K, whereas the number density of H_2 molecules can be estimated from the collision induced weak IR absorption in the frequency region of 4100 cm^{-1} to 5500 cm^{-1}. Chabal and Patel [59] reported a value of 10^{21} H_2 /cm^3 by analyzing data obtained from IR measurements at room temperature. Although the present study, based on pure *a*-Si networks, does not permit us to address the crucial role of hydrogen-bonding configurations in *a*-Si:H in general, it does provide us with new insights into the role of bonded and non- bonded hydrogens in the vicinity of the walls of H-rich voids. Tables 5.2 and 5.3, list the statistics and the average concentration of various bonded and non-bonded hydride configurations inside the voids, respectively.

Non-bonded hydrogens chiefly comprise H_2 molecules, along with one or two isolated H atoms near the voids. The latter possibly originate from the short annealing time of 10 ps

Table 5.2: Hydrogen bonding configuration AIMD-R model of *a*-Si:H at 300 K and 800 K. H_{iso}, H_2, SiH_n, R_g, r_g,R_H (Å) , V_H ($\times$ 10^3 Å^3) and Φ_S respectively represents number of isolated H, H molecule, silicon hydride configurations; $n = 1$ (monohydride), 2 (dihydride) and 3 (trihydride), calculated radius, Guinier radius, hull radius, hull volume and the degree of sphericity.

Void	H_2	H_{iso}	SiH	SiH_2	SiH_3	R_g	r_g	R_H	V_H	Φ_S
				300 K						
V1	1	0	25	2	0	6.67	9.83	8.34	2.09	0.51
V2	3	0	23	1	0	6.64	10.05	8.33	2.05	0.56
V4	3	0	18	3	0	6.71	8.45	8.5	2.22	0.59
V6	0	0	23	1	0	6.76	8.44	8.4	2.07	0.58
V7	1	0	26	1	0	6.53	7.81	8.2	1.95	0.62
V8	2	1	24	1	0	6.71	7.6	8.34	2.10	0.54
V10	1	0	27	1	0	6.65	10.62	8.31	2.06	0.54
V11	1	0	24	2	0	6.64	11.41	8.5	2.15	0.57
V12	3	1	21	0	1	6.59	10.75	8.35	2.12	0.51
V16	3	1	20	2	0	6.57	8.35	8.28	2.07	0.6
V17	4	0	23	0	0	6.57	10.01	8.34	2.17	0.59
V18	2	0	28	0	0	6.8	9.25	8.52	2.45	0.56
				800 K						
V1	0	0	26	2	0	6.45	10.02	8.36	2.08	0.90
V2	2	0	23	2	0	6.71	10.25	8.84	2.41	0.66
V4	2	0	22	2	0	6.7	9.97	9.07	2.55	0.79
V6	1	0	28	1	0	6.64	10.07	8.64	2.23	0.62
V7	0	0	26	1	0	6.72	10.33	8.95	2.46	0.70
V8	2	0	22	1	1	6.41	9.52	8.67	2.15	0.83
V10	3	0	18	3	0	6.71	9.82	8.94	2.31	0.64
V11	1	1	23	3	0	6.55	10.27	8.95	2.36	0.73
V12	1	0	26	1	0	6.62	8.59	9.07	2.45	0.62
V16	1	0	24	2	0	6.67	8.01	8.71	2.26	0.62
V17	3	1	23	1	0	6.38	11.81	8.38	2.09	0.81
V18	0	0	27	2	0	6.79	9.82	8.56	2.24	0.56

of AIMD simulations. The number of H_2 molecules per void ranges from 0 to 4 and 0 to 3 at 300 K and 800 K, respectively, which translates into a density of (1.5-2.2)$\times 10^{21}$ H_2/cm^3 for nanometer-size voids. This value matches very well with the experimental value of 10^{21} H_2/cm^3 from IR measurements by Chabal and Patel [59] as mentioned earlier. These results are also consistent with the data reported in Ref.[83], obtained from RBS measurements. On the other hand, the great majority of bonded hydrogens have appeared in monohydride(SiH) configurations. An examination of the local bonding environment of silicon atoms near the

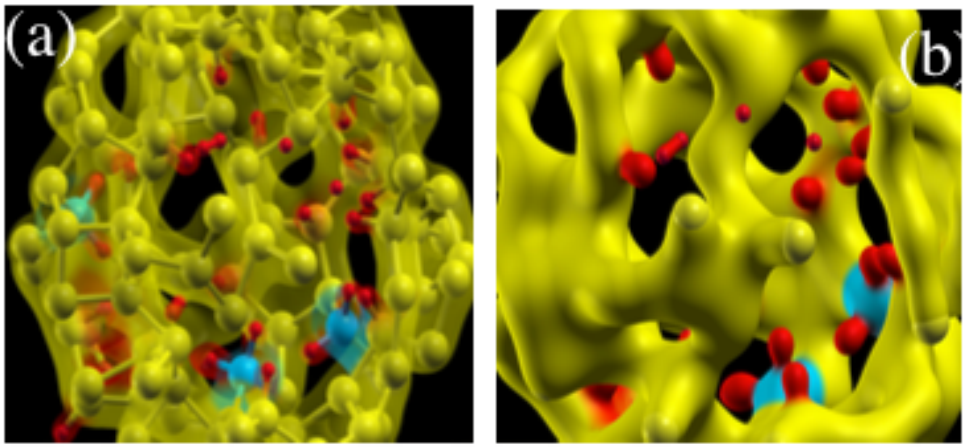

Figure 5.13: Bonded and non-bonded hydrogens inside a void (V3) from AIMD simulations at 300 K. (a)The interior wall of the void can be seen to be decorated with several SiH (yellow-red) and three SiH_2 (blue-red) configurations, as well as three H_2 molecules and a pair of isolated H atoms. (b) A magnified view of the wall, showing protruding monohydrides (yellow-red) and dihydrides (blue-red) on the wall.

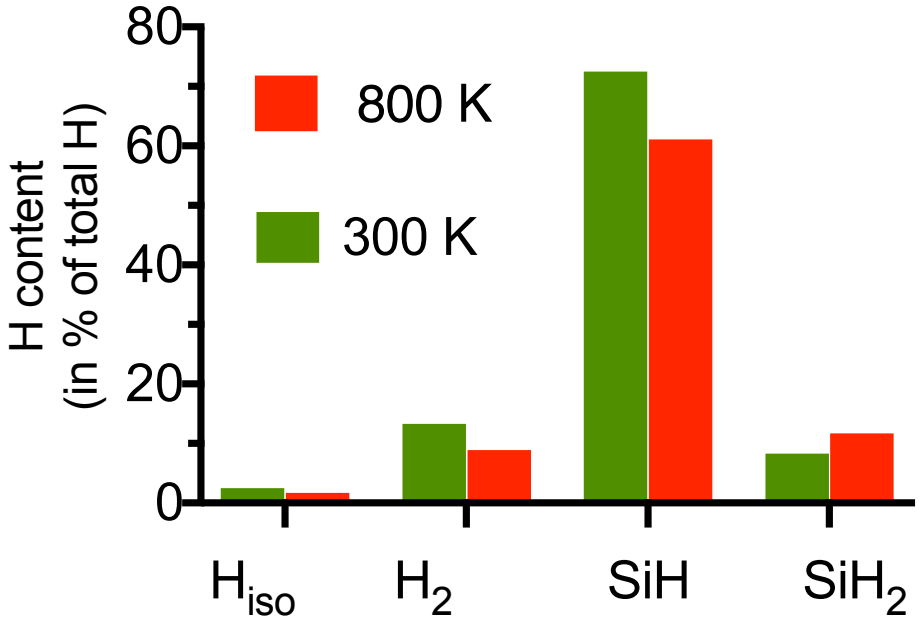

Figure 5.14: Hydrogen-bonding configurations in the vicinity of void surfaces in *a*-Si:H after annealing at 300 K and 800 K. The results presented here were averaged over 12 independent void configurations.

void surfaces showed that approximately 72.5 at.% and 61.1 at.% of total H atoms formed Si-H bonds at 300 K and 800 K, respectively. Of the remaining H atoms, about 8.3 %

Table 5.3: Average Si-H bonding statistics near the vicinity of voids.

Temp. (K)	H_{iso}%	H_2%	SiH%	SiH_2%	SiH_3%
300 K	2.5	13.33	72.5	8.33	0.83
800 K	1.39	8.89	61.11	11.67	0.83

(11.7%) were found to be bonded with Si as SiH_2 configurations at 300 K (800 K). The rest of the hydrogen has left the spherical void region of radius 10.5 Å. A graphic distribution of the presence of H_2 molecules and the bonded SiH_2 configurations on the wall of V3 at 300 K is depicted in Fig.5.13.

Several SiH_2 configurations can be seen to have formed on the surface of the void. This observation is consistent with experimental results from infrared measurements [59] and the recent computational studies based on information-driven atomistic modeling of *a*-Si:H [81, 82]. Figure 5.13 shows the concentration of hydrogen associated with various hydrogen-bonding configurations. The results clearly establish that a considerable number of H_2 molecules, of about 9-13% of the total H, can form near voids, depending upon the annealing temperature, concentration of H atoms, and the source of hydrogen.

5.4 Conclusions

In this chapter, we studied the temperature-induced nanostructural changes of the voids in *a*-Si at low and high annealing temperature in the range 300-800 K using classical and quantum-mechanical simulations, in the absence and presence of hydrogen near voids. This was achieved by generating an ultra-large model of *a*-Si, consisting of more than 260,000 atoms, in order to be able to produce a realistic distribution of nanometer-size voids in the amorphous environment of Si atoms, as observed in SAXS, PAL, IR, and hydrogen- effusion measurements. An examination of the distribution of the atoms near the voids reveals that the reconstruction of void surfaces in pure *a*-Si at 300 K led to minimal changes in the shape and size of the voids, which can be readily understood from a classical treatment of the problem. By contrast, the high-temperature annealing at 800 K caused significant changes in the shape and size of the voids, with noticeable structural differences between classical and quantum-mechanical results. This observation appears to indicate that classical potentials, such as the modified SW potential, might not be particularly suitable for an accurate description of the dynamics of Si atoms near voids and the resulting reconstruction of the void surfaces at high temperatures. An important outcome of this work is that the dynamics of bonded and non-bonded hydrogens near the voids and the degree of void-surface reconstruction

are found to be intrinsically related to each other. *Ab initio* annealing of *a*-Si networks with a void-volume fraction of 0.2% at 300 K and 800 K suggests that the presence of hydrogen within voids can facilitate surface reconstruction through the formation of silicon monohydride and dihydride configurations, as well as the displacement of Si atoms on the void surfaces. The rearrangement of atoms on void surfaces affects the diffusion of non-bonded hydrogens, which in turn produce surface bumps and changes the shape and size of the original void. This observation is reflected in the time evolution of hydrogen during annealing. The presence of Si atoms inside a heavily reconstructed fuzzy/rough void surface reduces the effective diffusion rate of hydrogen, due to additional scattering from the interior Si atoms, in their early time evolution. In contrast, a compact void surface with no or only a few Si atoms inside provides less resistance to hydrogen during their early evolution. Thus, hydrogen diffusion inside a compact or smooth void proceeds with little or no hindrance, leading to a notable difference in their mean-square-displacement (MSD) values during their early time evolution. Finally, the results from the study show the presence of bonded hydrogens, mostly SiH, SiH_2, and non-bonded hydrogens (NBH) in the form of H_2 molecules. The concentration of BH and NBH found in our study is consistent with the experimental values obtained from infrared (IR), Rutherford back scattering (RBS), and hydrogen-forward scattering (HFS) measurements. An examination of the hydride configurations near the voids suggests that the interior wall of the voids are decorated with SiH_2, which is supported by experimental results from infrared and ellipsometric studies. Likewise, the concentration of H_2 molecules obtained from the first-principles density-functional simulations in the present study is found to be consistent with the experimental value estimated from the collision-induced weak IR absorption by H_2 molecules in the frequency region of 4100-5500 cm^{-1}.

Chapter 6
SUMMARY

In summary, this dissertation contains a computational and theoretical study on a high-quality ultra-large model of *a*-Si particularly, on the void morphology. For the characterization of the voids, the small-angle X-ray scattering (SAXS) simulation method in conjunction with high-quality graphics for surface rendering is used. A systematic study of the variation of the simulated scattering intensity in the small-angle scattering region with the number density, size, shape, and the spatial distribution of the voids in the networks is presented in chapter 3. The relationship between the scattering intensity in small-angle region and the three-dimensional structure of nanoscale voids are addressed in ultra-large high-quality *a*-Si networks with $0.1 - 0.3\%$ void-volume fraction as observed in experiments using small-angle X-ray scattering (SAXS) and positron annihilation spectroscopy (PAS). Our results suggest that the scattering intensity in the small-angle region is particularly sensitive to the number density and size of the voids, but the effect of the geometry or shape and the distribution of the voids are less pronounced in the intensity profiles. A comparison of the average size of the voids obtained from the simulated values of the intensity, using the Guinier approximation [119] and Kratky plots [120], with those from the spatial distribution of the atoms in the vicinity of void surfaces are presented.

A computational study of the void-induced microstructure in ultra-large model of amorphous silicon *a*-Si with a void-volume fraction of 0.3% is presented in chapter 4. The relationship between the morphology of voids particularly shape and size, and corresponding scattering intensity in small angle region are studied by computing the the Fourier transform of the reduced pair-correlation function and the atomic-form factor of amorphous silicon. The effect of low-temperature ($\leq$600 K) annealing on restructuring the void morphology and the corresponding scattering intensities are addressed by studying atomic displacement on the void wall. A high-quality surface rendering software VMD is used to feature the void surfaces and their radius of gyrations are calculated from the spatial distribution of the surface atoms constructing the void wall. Also, from the scattering intensity plots, using Guinier approximation, Guinier radius of gyration of those annealed and corresponding annealed models are calculated and compared. The study suggests that low-temperature annealing can lead to considerable restructuring of void surfaces and scattering intensities in classical MD models of *a*-Si.

An *ab initio* study of the hydrogen microstructure in ultra-large model of amorphous silicon with an emphasis on the morphology of voids and the dynamics of hydrogen inside the voids. By using ultra-large *a*-Si model, obtained from classical molecular-dynamics simulations, with a realistic void-volume density of 0.2% as observed in experiments, the dynamics of Si and H atoms on the surface of the cavities are studied and their effects on the shape and size of the voids are examined using first-principles density-functional simulations. The results from *ab initio* calculations are compared with those obtained from using the modified Stillinger-Weber potential. The nanostructural evolution of the voids are examined by analyzing the three-dimensional distribution of Si and H atoms on/near void surfaces using the convex-hull approximation, and computing the radius of gyration of the corresponding convex hulls. A comparison of the results with those from the simulated values of the intensity in the small-angle X-ray scattering of a-Si/a-Si:H in the Guinier approximation is also provided, along with a discussion of bonded and non-bonded hydrogen in the vicinity of voids.

Appendix A

Pseudo-code for Filon's Method

```
c=========================
c Filon's method
c theta <0.1, use different A,B,C
c ==========================
       if(theta.lt.0.1) then
         A=the3*(2.0/45.0)-(2.0/315.0)*the5+(2.0/4725.0)*the7
         B=(2.0/3.0)+(2.0/15.0)*the2-
& (4.0/105.0)*the4+(2.0/567.0)*the6-
& (4.0/22275.0)*the8
          C=(4.0/3.0)-(2.0/15.0)*the2+(1.0/270.0)*the4-
              (1.0/11340.0)*the6+ (1.0/997920.0)*the8
         else
            A=q1+q2*(sin(theta)*cos(theta))-
                2.0*q3*(sin(theta)*sin(theta))
           B=2.0*(q2+q2*cos(theta)*cos(theta)-
               q3*2.0*sin(theta)*cos(theta))
           C=4.0*(q3*sin(theta)-q2*(cos(theta)))
         end if

       do jj =1,n
c  Si-Si interstion
       part11=A*(rdgr1(2*jj)*cos(k(ii)*r(2*jj))-
     &           rdgr1(2*jj+2)*cos(k(ii)*r(2*jj+2)))
       part12=B*(0.5*rdgr1(2*jj)*sin(k(ii)*r(2*jj))+
     &          0.5*rdgr1(2*jj+2)*sin(k(ii)*r(2*jj+2)))
       part13=C*(rdgr1(2*jj+1)*sin(k(ii)*r(2*jj+1)))
c  Si-H interaction
      part21=A*(rdgr2(2*jj)*cos(k(ii)*r(2*jj))-
     &           rdgr2(2*jj+2)*cos(k(ii)*r(2*jj+2)))
```

```
           part22=B*(0.5*rdgr2(2*jj)*sin(k(ii)*r(2*jj))+
     &          0.5*rdgr2(2*jj+2)*sin(k(ii)*r(2*jj+2)))
           part23=C*(rdgr2(2*jj+1)*sin(k(ii)*r(2*jj+1)))
c H-H interaction
else
part31=A*(rdgr3(2*jj)*cos(k(ii)*r(2*jj))-
     &           rdgr3(2*jj+2)*cos(k(ii)*r(2*jj+2)))
           part32=B*(0.5*rdgr3(2*jj)*sin(k(ii)*r(2*jj))+
     &          0.5*rdgr3(2*jj+2)*sin(k(ii)*r(2*jj+2)))
           part33=C*(rdgr3(2*jj+1)*sin(k(ii)*r(2*jj+1)))

c intgr=f(ii)*h*(part1+part2+part3)

         intgr1=h*(part11+part12+part13)
        intgr2=h*(part21+part22+part23)
         intgr3=h*(part31+part32+part33)
        sumint1(ii)=sumint1(ii)+intgr1
         sumint2(ii)=sumint2(ii)+intgr2
            sumint3(ii)=sumint3(ii)+intgr3
      end do
c============================
c partial structure factor Sk
c I(k)/N=F(k)
c xa and xb atomic fractions
c=========================
sk1(ii)=1.0+sumint1(ii)/k(ii)
sk2(ii)=1.0+sumint2(ii)/k(ii)
sk3(ii)=1.0+sumint3(ii)/k(ii)
F(ii)=fk1sq*(xa*xb+xa*xa*sk1(ii)) +
     fk2sq*(xa*xb+xb*xb*sk3(ii)) + 2.0*
      fk1*fk2*xa*xb*(sk2(ii)-1.0
```

Appendix B

Siesta-input

```
     ******************************
     *  WELCOME TO SIESTA  *
     ******************************
Dump of input data file ***************
System Name         SiH-FV2-V1-2234
SystemLabel         sih
NumberOfAtoms       2234
NumberOfSpecies     2
%block ChemicalSpeciesLabel
 1  14  Si
 2   1  H
%endblock ChemicalSpeciesLabel
PAO.BasisSize       SZ
PAO.EnergyShift     300 meV
LatticeConstant     50.0 Ang
%block LatticeVectors
  1.000  0.000  0.000
  0.000  1.000  0.000
  0.000  0.000  1.000
%endblock LatticeVectors
MeshCutoff          100.0 Ry
MaxSCFIterations    50
DM.MixingWeight      0.3
DM.NumberPulay       3
DM.Tolerance         5.d-3
DM.UseSaveDM
SolutionMethod       diagon
ElectronicTemperature  25 meV
Harries_functional    .true.
```

```
XC.functional      LDA
XC.authors      CA
MD.TypeOfRun         CG
MD.NumCGsteps        5
UseSaveData          T
MD.LengthTimestep    10 fs
MD.MaxCGDispl        0.1  Ang
MD.MaxForceTol       0.01 eV/Ang
%block GeometryConstraints
position from 1253 to 2204 1.0 0.0 0.0
position from 1253 to 2204 0.0 1.0 0.0
position from 1253 to 2204 0.0 0.0 1.0
%endblock GeometryConstraints
WarningMinimumAtomicDistance  1.0 Ang
AtomicCoordinatesFormat  ScaledCartesian
%block AtomicCoordinatesAndAtomicSpecies
   21.622967  -35.604701   52.874742          1   Si          1
   16.764405  -44.973789   58.111836          1   Si          2
   24.742495  -51.464017   55.390840          1   Si          3
   15.454297  -44.934751   52.349602          1   Si          4
   26.188266  -45.687792   50.502932          1   Si          5
   25.321317  -47.975523   61.073169          1   Si          6
   15.332203  -44.762164   56.306614          1   Si          7
   29.043011  -46.348350   55.962616          1   Si          8
   20.296670  -50.624200   60.928876          1   Si          9
   17.994528  -49.350855   53.224613          1   Si         10
   ..........................................
   ..........................................
   23.369800  -43.788000   57.203900          2   H        2230
   22.433800  -39.688600   55.941700          2   H        2231
   25.868700  -42.473800   58.846400          2   H        2232
   26.040600  -40.680200   54.086700          2   H        2233
   19.345800  -40.010500   59.728000          2   H        2234
%endblock AtomicCoordinatesAndAtomicSpecies
End of input data file **********************************
```

BIBLIOGRAPHY

[1] Xie, R., Long, G.G., Weigand, S.J., Moss, S.C., Carvalho, T., Roorda, S., Hejna, M., Torquato, S., and Steinhardt, P.J. *Hyperuniformity in amorphous silicon based on the measurement of the infinite-wavelength limit of the structure factor*. Proceedings of the National Academy of Science, **110**(33), 13250–13254 (2013)

[2] Williamson, D. *Microstructure of amorphous-silicon-based solar cell materials by small-angle X-ray scattering*. NREL/TP-411-8122.UC Category 1262. DE95009273, page 1262 (1995). URL `https://digital.library.unt.edu/ark:/67531/metadc619364/`

[3] Laaziri, K., Kycia, S., Roorda, S., Chicoine, M., Robertson, J.L., Wang, J., and Moss, S.C. *High-energy X-ray diffraction study of pure amorphous silicon*. Phys. Rev. B, **60**(19), 13520–13533 (1999)

[4] Thompson, M.J. and Tuan, H.C. *Amorphous silicon electronic devices and their applications*. IEEE Aerospace and Electronic Systems Magazine, **2**(8), 25–29 (1987)

[5] Street, R.A. *Hydrogenated Amorphous Silicon*. Cambridge Solid State Science Series, (Cambridge University Press1991)

[6] Street, R. *Technology and Applications of Amorphous Silicon*, volume 37 of *Springer Series in Materials Science*, (Springer-Verlag2000)

[7] Kasap, S. and Capper, P. *Springer Handbook of Electronic and Photonic Materials*. Springer Handbooks, (Springer International Publishing2017)

[8] Yonezawa, F. *Fundamental Physics of Amorphous Semiconductors: Proceedings of the Kyoto Summer Institute, Kyoto, Japan, September 8-11, 1980*. Springer series in solid-state sciences, (Springer-Verlag1981)

[9] Morigaki, K., Kugler, S., and Shimakawa, K. *Amorphous Semiconductors: Structural, Optical, and Electronic Properties*. Wiley Series in Materials for Electronic & Optoelectronic Applications, (Wiley2016)

[10] Gope, J., Kumar, S., Parashar, A., Dixit, P., Rauthan, C., Panwar, O., Patel, D., and Agarwal, S. *Amorphous and nanocrystalline silicon made by varying deposition pressure in pecvd process*. Journal of Non-Crystalline Solids, **355**(45), 2228 – 2232 (2009)

[11] Schropp, R.E. and Zenan, M. *Amorphous and Microcrystalline Silicon Solar Cells: Modeling, Materials and Device Technology*, volume 5 of *Electronic Materials: Science & Technology*, (Springer US1998)

[12] Johari, G., Ram, S., Astl, G., and Mayer, E. *Characterizing amorphous and microcrystalline solids by calorimetry*. Journal of Non-Crystalline Solids, **116**(2), 282 – 285 (1990)

[13] Bergmann, R., Kohler, J., Dassow, R., Zaczek, C., and Werner, J. *Nucleation and growth of crystalline silicon films on glass for solar cells*. physica status solidi (a), **166**, 587 – 602 (1998)

[14] Morigaki, K. *Physics of Amorphous Semiconductors*, (World Scientific1999)

[15] Hui, C. and E. Miller, C. *A rapid quenching technique for the preparation of thin uniform films of amorphous solids*. Review of Scientific Instruments, **41**, 1237 – 1238 (1970)

[16] H. Cohen, M. *Theory of amorphous semiconductors*. Radiation Effects, **8**, 261–262 (1971)

[17] Muller, H. and Thomas, P. *Activated transport in amorphous semiconductors. I. the theoretical approach*. Journal of Physics C: Solid State Physics, **17**, 5337 (2000)

[18] Schulze, T.F., Korte, L., Ruske, F., and Rech, B. *Band lineup in amorphous/crystalline silicon heterojunctions and the impact of hydrogen microstructure and topological disorder*. Phys. Rev. B, **83**, 165314 (2011)

[19] Agarwal, S.C. *Nature of localized states in amorphous semiconductors- A study by electron spin resonance*. Phys. Rev. B, **7**, 685–691 (1973)

[20] Nemanich, R., Lucovsky, G., Pollard, W., and Joannopoulos, J. *Spectroscopic evidence for bonding coordination defects in amorphous as*. Solid State Communications, **26**(3), 137 – 139 (1978)

[21] Custer, J.S., Thompson, M.O., Jacobson, D.C., Poate, J.M., Roorda, S., Sinke, W.C., and Spaepen, F. *Density of amorphous Si*. Applied Physics Letters, **64**(4), 437–439 (1994)

[22] Smith, Z.E. and Wagner, S. *Band tails, entropy, and equilibrium defects in hydrogenated amorphous silicon*. Phys. Rev. Lett., **59**, 688–691 (1987)

[23] Street, R.A., Biegelsen, D.K., and Knights, J.C. *Defect states in doped and compensated a-Si:H*. Phys. Rev. B, **24**, 969–984 (1981)

[24] Stutzmann, M. and Biegelsen, D.K. *Dangling or floating bonds in amorphous silicon*. Phys. Rev. Lett., **60**, 1682–1682 (1988)

[25] Brodsky, M.H. and Title, R.S. *Electron spin resonance in amorphous silicon, germanium, and silicon carbide*. Phys. Rev. Lett., **23**, 581–585 (1969)

[26] Pantelides, S.T. *Defects in amorphous silicon: A new perspective*. Phys. Rev. Lett., **57**, 2979–2982 (1986)

[27] Chittick, R., Alexander, H.J., and Sterling, H.F. *The preparation and properties of amorphous silicon*. Journal of The Electrochemical Society - J ELECTROCHEM SOC, **116** (1969)

[28] Lucovsky, G., Nemanich, R.J., and Knights, J.C. *Structural interpretation of the vibrational spectra of a-Si: H alloys*. Phys. Rev. B, **19**, 2064–2073 (1979)

[29] Smets, A.H.M., Kessels, W.M.M., and van de Sanden, M.C.M. *Vacancies and voids in hydrogenated amorphous silicon*. Applied Physics Letters, **82**(10), 1547–1549 (2003)

[30] Paul, W. and Anderson, D.A. *Properties of amorphous hydrogenated silicon, with special emphasis on preparation by sputtering*. Solar Energy Materials, **5**(3), 229 – 316 (1981)

[31] Spear, W.E. and Comber, P.G.L. *Electronic properties of substitutionally doped amorphous Si and Ge*. The Philosophical Magazine: A Journal of Theoretical Experimental and Applied Physics, **33**(6), 935–949 (1976)

[32] Carlson, D.E. and Wronski, C.R. *Amorphous silicon solar cell*. Applied Physics Letters, **28**(11), 671–673 (1976)

[33] Carlson, D.E. and Wronski, C.R. *Amorphous silicon solar cell*. Journal of Electronic Materials, **6**(2), 95–196 (1977)

[34] Zhang, S.B. and Branz, H.M. *Hydrogen above saturation at silicon vacancies: H-pair reservoirs and metastability sites*. Phys. Rev. Lett., **87**, 105503 (2001)

[35] Postol, T.A., Falco, C.M., Kampwirth, R.T., Schuller, I.K., and Yelon, W.B. *Structure of amorphous silicon and silicon hydrides*. Phys. Rev. Lett., **45**, 648–652 (1980)

[36] Chenevas-Paule, A., Bellissent, R., Roth, M., and I., P.J. *Correlation between staebler wronski effect and medium range order in a-Si:H by sans*. Journal of Non-Crystalline Solids, **77-78**, 373 – 376 (1985)

[37] Craven, A.J., Patterson, A.M., Long, A.R., and Wilson, J.I.B. *Small angle electron scattering in a-Si and a-Si:H films*. Journal of Non-Crystalline Solids, **77-78**, 217 – 220 (1985)

[38] D'Antonio, P. and Konnert, J.H. *Small-angle-scattering evidence of voids in hydrogenated amorphous silicon*. Phys. Rev. Lett., **43**, 1161–1163 (1979)

[39] Muramatsu, S., Matsubara, S., Watanabe, T., Shimada, T., Kamiyama, T., and Suzuki, K. *Small-angle X-ray scattering studies of a-Si_{1-x} Ge_x: H alloys*. Journal of Non-Crystalline Solids, **150**(1), 163 – 166 (1992)

[40] Mahan, A.H., Williamson, D.L., Nelson, B.P., and Crandall, R.S. *Characterization of microvoids in device-quality hydrogenated amorphous silicon by small-angle X-ray scattering and infrared measurements*. Phys. Rev. B, **40**(17), 12024–12027 (1989)

[41] Mahan, A.H., Xu, Y., Williamson, D.L., Beyer, W., Perkins, J.D., Vanecek, M., Gedvilas, L.M., and Nelson, B.P. *Structural properties of hot wire a-Si:H films deposited at rates in excess of 100Å/s*. Journal of Applied Physics, **90**, 5038–5047 (2001)

[42] Manfredotti, C., Fizzotti, F., Boero, M., Pastorino, P., Polesello, P., and Vittone, E. *Influence of hydrogen-bonding configurations on the physical properties of hydrogenated amorphous silicon*. Phys. Rev. B, **50**(24), 18046–18053 (1994)

[43] Ouwens, J.D. and Schropp, R.E.I. *Hydrogen microstructure in hydrogenated amorphous silicon*. Phys. Rev. B, **54**, 17759–17762 (1996)

[44] Reimer, J.A., Vaughan, R.W., and Knights, J.C. *Proton nmr studies of annealed plasma-deposited amorphous Si:H films*. Solid State Communications, **37**(2), 161 – 164 (1981)

[45] Carlos, W.E. and Taylor, P.C. *^{1}H NMR in a-Si*. Phys. Rev. B, **26**, 3605–3616 (1982)

[46] Baum, J., Gleason, K.K., Pines, A., Garroway, A.N., and Reimer, J.A. *Multiple-quantum nmr study of clustering in hydrogenated amorphous silicon*. Phys. Rev. Lett., **56**, 1377–1380 (1986)

[47] Petrich, M.A., Gleason, K.K., and Reimer, J.A. *Structure and properties of amorphous hydrogenated silicon carbide*. Phys. Rev. B, **36**, 9722–9731 (1987)

[48] Graebner, J.E., Golding, B., Allen, L.C., Biegelsen, D.K., and Stutzmann, M. *Solid hydrogen in hydrogenated amorphous silicon*. Phys. Rev. Lett., **52**(7), 553–556 (1984)

[49] Löhneysen, H.V., Schink, H.J., and Beyer, W. *Direct experimental evidence for molecular hydrogen in amorphous Si: H*. Phys. Rev. Lett., **52**, 549–552 (1984)

[50] Young, D.L., Stradins, P., Xu, Y., Gedvilas, L.M., Iwaniczko, E., Yan, Y., Branz, H.M., Wang., Q., and Williamson, D.L. *Nanostructure evolution in hydrogenated amorphous silicon during hydrogen effusion and crystallization*. Applied Physics Letters, **90**(8), 081923 (2007)

[51] Keita, A.S., Wang, Z., Phillipp, F., Bischoff, E., and Mittemeijer, E.J. *Highly retarded crystallization in hydrogenated amorphous germanium; emergence of a porous nanocrystalline structure*. Thin Solid Films, **615**, 145 – 151 (2016)

[52] Fontcuberta I Morral, A., Roca I Cabarrocas, P., and Clerc, C. *Structure and hydrogen content of polymorphous silicon thin films studied by spectroscopic ellipsometry and nuclear measurements*. Phys. Rev. B, **69**, 125307 (2004)

[53] Wright, C.A., Hannon, C.A., Sinclair, N.R., Brunier, T.M., Guy, A.C., Stewart, J.R., Strobel, B.M., and Jansen, F. *Neutron scattering studies of hydrogenated, deuterated and fluorinated amorphous silicon*. Journal of Physics: Condensed Matter, **19**(41), 415109 (2007)

[54] Mathé, E., Naudon, A., Elliq, M., Fogarassy, E., and de Unamuno, S. *Influence of hydrogen on the structure and surface morphology of pulsed arf excimer laser crystallized amorphous silicon thin films*. Applied Surface Science, **54**, 392 – 400 (1992). ISSN 0169-4332

[55] Wang, H., Lusquiñs, F., and Yao, Y. *Effect of hydrogen on surface texturing and crystallization of a-Si:H thin film irradiated by excimer laser*. Applied Physics A, **107**, 307–320 (2012)

[56] Manakov, S. and I. Taurbayev, T. *Morphology and structural properties of a-Si:H and a-SiC:H films controlled in nanoscale*. Journal of Nanoelectronics and Optoelectronics, **7**, 619–622 (2012)

[57] Williamson, D., Mahan, A., Nelson, B., and Crandall, R. *The observation of microvoids in device quality hydrogenated amorphous silicon*. Journal of Non-Crystalline Solids, **114**, 226 – 228 (1989)

[58] Boyce, J.B. and Stutzmann, M. *Orientational ordering and melting of molecular H_2 in an a-Si matrix: NMR studies*. Phys. Rev. Lett., **54**, 562–565 (1985)

[59] Chabal, Y.J. and Patel, C.K.N. *Infrared Absorption in a-Si:H: First Observation of Gaseous Molecular H_2 and Si-H Overtone*. Phys. Rev. Lett., **53**(2), 210–213 (1984)

[60] Conradi, M.S. and Norberg, R.E. *Molecular H_2: Nuclear-spin-relaxation centers for protons in a-Si: H*. Phys. Rev. B, **24**, 2285–2288 (1981)

[61] He, Y.J., Hasegawa, M., Lee, R., Berko, S., Adler, D., and Jung, A.L. *Positron-annihilation study of voids in a-Si and a-Si:H*. Phys. Rev. B, **33**, 5924–5927 (1986)

[62] Biswas, P., Atta-Fynn, R., and Drabold, D.A. *Reverse monte carlo modeling of amorphous silicon*. Phys. Rev. B, **69**, 195207 (2004)

[63] Limbu, D.K., Atta-Fynn, R., Drabold, D.A., Elliott, S.R., and Biswas, P. *Structural properties of transition-metal clusters via force-biased monte carlo and ab initio calculations: A comparative study*. Phys. Rev. B, **96**, 174208 (2017)

[64] Limbu, D.K., Atta-Fynn, R., Drabold, D.A., Elliott, S.R., and Biswas, P. *Information-driven inverse approach to disordered solids: Applications to amorphous silicon*. Phys. Rev. Materials, **2**, 115602 (2018)

[65] Limbu, D.K., Atta-Fynn, R., and Biswas, P. *Atomistic simulation of nearly defect-free models of amorphous silicon: An informa tion-based approach*. MRS Advances, **4**(2), 87–93 (2019)

[66] Biswas, R., Kwon, I., Bouchard, A.M., Soukoulis, C.M., and Grest, G.S. *Intense small wave-vector scattering from voids in amorphous silicon: A theoretical simulation*. Phys. Rev. B, **39**, 5101–5106 (1989)

[67] Brahim, R. and Chehaidar, A. *Small-Angle X-Ray Scattering of Amorphous Germanium: Numerical Modeling*. Advances in Materials Physics and Chemistry, **3**(1A), 19–30 (2013)

[68] Barkema, G.T. and Mousseau, N. *High-quality continuous random networks*. Phys. Rev. B, **62**, 4985–4990 (2000)

[69] Stillinger, F.H. and Weber, T.A. *Computer simulation of local order in condensed phases of silicon*. Phys. Rev. B, **31**(8), 5262–5271 (1985)

[70] Vink, R.L.C., Barkema, G.T., van der Weg, W.F., and Mousseau, N. *Fitting the Stillinger-Weber potential to amorphous silicon*. Journal of Non-Crystalline Solids, **282**(2), 248–255 (2001)

[71] Donovan, T.M. and Heinemann, K. *High-resolution electron microscope observation of voids in amorphous Ge*. Phys. Rev. Lett., **27**, 1794–1796 (1971)

[72] Galeener, F.L. *Optical evidence for a network of cracklike voids in amorphous germanium*. Phys. Rev. Lett., **27**, 1716–1719 (1971)

[73] Shevchik, N.J. and Paul, W. *Voids in amorphous semiconductors*. Journal of Non-Crystalline Solids, **16**(1), 55 – 71 (1974)

[74] Letcher, J.H. and Schmidt, P.W. *Small-angle X-ray scattering determination of particle-diameter distributions in polydisperse suspensions of spherical particles*. Journal of Applied Physics, **37**(2), 649–655 (1966)

[75] Muramatsu, S., Suzuki, R., Wei, L., and Tanigawa, S. *Microvoids in a-Si:H and a-SiGe:H alloys*. Solar Energy Materials and Solar Cells, **34**(1), 525 – 531 (1994)

[76] Williamson, D.L., Roorda, S., Chicoine, M., Tabti, R., Stolk, P.A., Acco, S., and Saris, F.W. *On the nanostructure of pure amorphous silicon*. Applied Physics Letters, **67**(2), 226–228 (1995)

[77] Zou, X., Chan, Y.C., Webb, D.P., Lam, Y.W., Hu, Y.F., Beling, C.D., Fung, S., and Weng, H.M. *Photoinduced dehydrogenation of defects in undoped a-Si:H using positron annihilation spectroscopy*. Phys. Rev. Lett., **84**, 769–772 (2000)

[78] Beyer, W. *Characterization of microstructure in amorphous and microcrystalline si and related alloys by effusion of implanted helium*. Physica Status Solidi (c), **1**(5), 1144–1153 (2004)

[79] Chakraborty, S. and Drabold, D.A. *Static and dynamic properties of hydrogenated amorphous silicon with voids*. Phys. Rev. B, **79**, 115214 (2009)

[80] Beyer, W., Hilgers, W., Prunici, P., and Lennartz, D. *Voids in hydrogenated amorphous silicon materials*. Journal of Non-Crystalline Solids, **358**(17), 2023 – 2026 (2012)

[81] Biswas, P., Drabold, D.A., and Atta-Fynn, R. *Microstructure from joint analysis of experimental data and ab initio interactions: Hydrogenated amorphous silicon*. Journal of Applied Physics, **116**(24), 244305 (2014)

[82] Biswas, P. and Elliott, S.R. *Nanoscale structure of microvoids in a-Si:H: A first-principles study*. Journal of Physics: Condensed Matter, **27**(43), 435201 (2015)

[83] Sekimoto, T., Matsumoto, M., Sagara, A., Hishida, M., and Terakawa, A. *Changes in the vacancy size distribution induced by non-bonded hydrogens in hydrogenated amorphous silicon*. Journal of Non-Crystalline Solids, **447**, 207 – 211 (2016)

[84] Biswas, P., Paudel, D., Atta-Fynn, R., Drabold, D.A., and Elliott, S.R. *Morphology and number density of voids in hydrogenated amorphous silicon: An ab initio study*. Phys. Rev. Applied, **7**, 024013 (2017)

[85] Paudel, D., Atta-Fynn, R., Drabold, D.A., Elliott, S.R., and Biswas, P. *Small-angle X-ray scattering in amorphous silicon: A computational study*. Phys. Rev. B, **97**(18), 184202 (2018)

[86] Sekimoto, T., Matsumoto, M., and Terakawa, A. *Dense restructuring of amorphous silicon network induced by non-bonded hydrogen*. Japanese Journal of Applied Physics, **57**(8S3), 08RB07 (2018)

[87] Beyer, W., Andrä, G., Bergmann, J., Breuer, U., Finger, F., Gawlik, A., Haas, S., Lambertz, A., Maier, F.C., Nickel, N.H., and Zastrow, U. *Temperature and hydrogen diffusion length in hydrogenated amorphous silicon films on glass while scanning with a continuous wave laser at 532nm wavelength*. Journal of Applied Physics, **124**(15), 153103 (2018)

[88] Kugler, S., Molnár, G., Petö, G., Zsoldos, E., Rosta, L., Menelle, A., and Bellissent, R. *Neutron-diffraction study of the structure of evaporated pure amorphous silicon*. Physical review. B, Condensed matter, **40**, 8030–8032 (1989)

[89] Gleason, K.K., Petrich, M.A., and Reimer, J.A. *Hydrogen microstructure in amorphous hydrogenated silicon*. Phys. Rev. B, **36**, 3259–3267 (1987)

[90] Langford, A.A., Fleet, M.L., Nelson, B.P., Lanford, W.A., and Maley, N. *Infrared absorption strength and hydrogen content of hydrogenated amorphous silicon*. Phys. Rev. B, **45**, 13367–13377 (1992)

[91] Freeman, E.C. and Paul, W. *Infrared vibrational spectra of RF-sputtered hydrogenated amorphous silicon*. Phys. Rev. B, **18**, 4288–4300 (1978)

[92] Shanks, H., Fang, C.J., Ley, L., Cardona, M., Demond, F.J., and Kalbitzer, S. *Infrared spectrum and structure of hydrogenated amorphous silicon*. physica status solidi (b), **100**(1), 43–56 (1980)

[93] Polk, D. *Structural model for amorphous silicon and germanium*. Journal of Non-Crystalline Solids, **5**(5), 365 – 376 (1971)

[94] Wooten, F., Winer, K., and Weaire, D. *Computer generation of structural models of amorphous Si and Ge*. Phys. Rev. Lett., **54**, 1392–1395 (1985)

[95] Keating, P.N. *Effect of invariance requirements on the elastic strain energy of crystals with application to the diamond structure*. Phys. Rev., **145**, 637–645 (1966)

[96] Tersoff, J. *New empirical approach for the structure and energy of covalent systems*. Phys. Rev. B, **37**, 6991–7000 (1988)

[97] Kwon, I., Biswas, R., and Soukoulis, C.M. *Molecular-dynamics simulations of defect formation in hydrogenated amorphous silicon*. Phys. Rev. B, **45**, 3332–3339 (1992)

[98] Zi, J., Zhang, K., and Xie, X. *Modification of Stillinger-Weber potentials for Si and Ge*. Physical review. B, Condensed Matter, **41**, 12915–12918 (1990)

[99] Tuttle, B. and Adams, J.B. *Structure of a-Si:H from harris-functional molecular dynamics*. Phys. Rev. B, **53**, 16265–16271 (1996)

[100] Jones, R. and Briddon, P. *Chapter 6 the ab initio cluster method and the dynamics of defects in semiconductors*. In *Identification of Defects in Semiconductors*, volume 51 of *Semiconductors and Semimetals*, pages 287 – 349, (Elsevier1998)

[101] Buda, F., Chiarotti, G.L., Car, R., and Parrinello, M. *Structure of hydrogenated amorphous silicon from ab initio molecular dynamics*. Phys. Rev. B, **44**, 5908–5911 (1991)

[102] Jarolimek, K., de Groot, R.A., de Wijs, G.A., and Zeman, M. *First-principles study of hydrogenated amorphous silicon*. Phys. Rev. B, **79**, 155206 (2009)

[103] Marx, D. and Hutter, J. *Ab Initio Molecular Dynamics: Basic Theory and Advanced Methods*, (Cambridge University Press2009). ISBN 9781139477192

[104] Car, R. and Parrinello, M. *Unified approach for molecular dynamics and density-functional theory*. Phys. Rev. Lett., **55**, 2471–2474 (1985)

[105] Thomas, L.H. *The calculation of atomic fields*. Mathematical Proceedings of the Cambridge Philosophical Society, **23**(5), 542–548 (1927)

[106] Fermi, E. *Eine statistische methode zur bestimmung einiger eigenschaften des atoms und ihre anwendung auf die theorie des periodischen systems der elemente*. Zeitschrift für Physik, **48**(1), 73–79 (1928)

[107] Hartree, D.R. *The wave mechanics of an atom with a non-coulomb central field. Part I. Theory and Methods*. Mathematical Proceedings of the Cambridge Philosophical Society, **24**(1), 89–110 (1928)

[108] Hartree, D.R. *The wave mechanics of an atom with a non-coulomb central field. Part II. Some Results and Discussion*. Mathematical Proceedings of the Cambridge Philosophical Society, **24**(1), 111–132 (1928)

[109] Dirac, P.A.M. *Note on exchange phenomena in the thomas atom*. Mathematical Proceedings of the Cambridge Philosophical Society, **26**(3), 376?385 (1930)

[110] Kohn, W. and Sham, L.J. *Self-consistent equations including exchange and correlation effects*. Phys. Rev., **140**, A1133–A1138 (1965)

[111] Kato, T. *On the eigenfunctions of many-particle systems in quantum mechanics*. Communications on Pure and Applied Mathematics, **10**(2), 151–177 (1957)

[112] Perdew, J.P. and Yue, W. *Accurate and simple density functional for the electronic exchange energy: Generalized gradient approximation*. Phys. Rev. B, **33**, 8800–8802 (1986)

[113] Perdew, J.P., Burke, K., and Ernzerhof, M. *Generalized gradient approximation made simple*. Phys. Rev. Lett., **77**, 3865–3868 (1996)

[114] Fortner, J. and Lannin, J.S. *Radial distribution functions of amorphous silicon*. Phys. Rev. B, **39**, 5527–5530 (1989)

[115] Singh, R., Prakash, S., Nath Shukla, N., and Prasad, R. *Sample dependence of the structural, vibrational, and electronic properties of a-Si:H : A density-functional-based tight-binding study*. Phys. Rev. B, **70** (2004)

[116] Anderson, P.W. *Model for the electronic structure of amorphous semiconductors*. Phys. Rev. Lett., **34**, 953–955 (1975)

[117] Alben, R., Weaire, D., Smith, J.E., and Brodsky, M.H. *Vibrational properties of amorphous Si and Ge*. Phys. Rev. B, **11**, 2271–2296 (1975)

[118] Rella, C.W., van der Voort, M., Akimov, A.V., van der Meer, A.F.G., and Dijkhuis, J.I. *Localization of the Si-H stretch vibration in amorphous silicon*. Applied Physics Letters, **75**(19), 2945–2947 (1999)

[119] Guinier, A. and Fournet, G. *Small-angle scattering of X-rays*, (Wiley1995)

[120] Kratky, O. and Glatter, O. *Small angle x-ray scattering*, (Academic Press London ; New York1982). ISBN 0122862805

[121] Feigin, L. and Svergun, D. *Structure Analysis by Small-Angle X-Ray and Neutron Scattering*, (Springer US2013)

[122] Lazzari, R. *IsGISAXS: a program for grazing-incidence small-angle X-ray scattering analysis of supported islands*. Journal of Applied Crystallography, **35**(4), 406–421 (2002)

[123] Debye, P. *Zerstreuung von Röntgenstrahlen*. Annalen der Physik, **351**(6), 809–823 (1915)

[124] Schneidman, D., Kim, S.J., and Sali, A. *Integrative structural modeling with small angle X-ray scattering profiles*. BMC structural biology, **12**, 17 (2012)

[125] Cromer, D.T. and Mann, J.B. *X-ray scattering factors computed from numerical Hartree–Fock wave functions*. Acta Crystallographica Section A, **24**(2), 321–324 (1968)

[126] Cusack, N. *The Physics of Structurally Disordered Matter: An Introduction (Graduate Student Series in Physics)*, (Adam Hilger1987)

[127] Elliott, S.R. *Physics of Amorphous Materials 2nd edition*, (Harlow : Longman Scientific & Technical1990)

[128] Filon, L.N.G. *III on a quadrature formula for trigonometric integrals*. Proceedings of the Royal Society of Edinburgh, **49**, 38–47 (1930)

[129] Guinier, A. *X-ray Diffraction in Crystals, Imperfect Crystals, and Amorphous Bodies*. Dover Books on Physics Series, (Dover Publications1994)

[130] Hura, G.L., Menon, A.L., Hammel, M., Rambo, R.P., Poole II, F.L., Tsutakawa, S.E., Jenney Jr, F.E., Classen, S., Frankel, K.A., Hopkins, R.C., Yang, S.j., Scott, J.W., Dillard, B.D., Adams, M.W.W., and Tainer, J.A. *Robust, high-throughput solution structural analyses by small angle X-ray scattering (SAXS)*. Nature Methods, **6**, 606 (2009)

[131] Walenta, E. *Small angle X-ray scattering. von o. glatter und o. kratky*. Acta Polymerica, **36**(5), 296–296 (1985)

[132] Bernadó, P. and Svergun, D.I. *Analysis of Intrinsically Disordered Proteins by Small-Angle X-ray Scattering*, pages 107–122, (Springer New York, New York, NY2012)

[133] Mertens, H.D. and Svergun, D.I. *Structural characterization of proteins and complexes using small-angle X-ray solution scattering*. Journal of Structural Biology, **172**(1), 128 – 141 (2010)

[134] Putnam, C.D., Hammel, M., Hura, G.L., and Tainer, J.A. *X-ray solution scattering (saxs) combined with crystallography and computation: defining accurate macromolecular structures, conformations and assemblies in solution*. Quarterly Reviews of Biophysics, **40**(3), 191–285 (2007)

[135] Akiyama, S., Nohara, A., Ito, K., and Maéda, Y. *Assembly and disassembly dynamics of the cyanobacterial periodosome*. Molecular Cell, **29**(6) (2008)

[136] Doniach, S. *Changes in biomolecular conformation seen by small angle X-ray scattering*. Chemical Reviews, **101**(6), 1763–1778 (2001)

[137] BernadÄ, P., Mylonas, E., Petoukhov, M.V., Blackledge, M., and Svergun, D.I. *Structural characterization of flexible proteins using small-angle X-ray scattering*. Journal of the American Chemical Society, **129**(17), 5656–5664 (2007)

[138] Bernado, P. and Svergun, D.I. *Structural analysis of intrinsically disordered proteins by small-angle X-ray scattering*. Mol. BioSyst., **8**, 151–167 (2012)

[139] Zheng, W. and Doniach, S. *Protein structure prediction constrained by solution X-ray scattering data and structural homology identification*. Journal of Molecular Biology, **316**(1), 173–187 (2002)

[140] Moore, P.B. *Small-angle scattering. information content and error analysis*. Journal of Applied Crystallography, **13**(2), 168–175 (1980)

[141] de Graff, A. and Thorpe, M. *The long-wavelength limit of the structure factor of amorphous silicon and vitreous silica*. Acta Crystallographica Section A: Foundations and Advances, **66**(1), 22–31 (2010)

[142] Nosé, S. *A unified formulation of the constant temperature molecular dynamics methods*. J. Chem. Phys., **81**(1), 511–519 (1984)

[143] Hoover, W.G. *Canonical dynamics: Equilibrium phase-space distributions*. Phys. Rev. A, **31**, 1695–1697 (1985)

[144] Martyna, G.J., Tuckerman, M.E., Tobias, D.J., and Klein, M.L. *Explicit reversible integrators for extended systems dynamics*. Mol. Phys., **87**(5), 1117–1157 (1996)

[145] Nocedal, J. *Updating quasi-newton matrices with limited storage*. Mathematics of Computation, **35**, 773–782 (1980)

[146] Liu, D.C. and Nocedal, J. *On the limited memory bfgs method for large scale optimization*. Mathematical Programming, **45**(1), 503–528 (1989)

[147] Shannon, C.E. *A mathematical theory of communication*. The Bell System Technical Journal, **27**(3), 379–423 (1948)

[148] Damaschun, G.and Müller, J.J. and Pürschel, H.V. *Über die meß-strategie bei der untersuchung der röntgenkleinwinkelstreuung von verdünnten monodispersen lösungen von makromolekülen, 1. mitt*. Monatshefte für Chemie / Chemical Monthly (1968)

[149] Levashov, V.A., Billinge, S.J.L., and Thorpe, M.F. *Density fluctuations and the pair distribution function*. Phys. Rev. B, **72**, 024111 (2005)

[150] *International Tables for Crystallography. Volume C: Mathematical Physical and Chemical Tables*. Acta Crystallographica Section A, **49**(2), 371–373 (1993)

[151] Doyle, P.A. and Turner, P.S. *Relativistic Hartree–Fock X-ray and electron scattering factors*. Acta Crystallographica Section A, **24**(3), 390–397 (1968)

[152] Smith, G.H. and Burge, R.E. *The analytical representation of atomic scattering amplitudes for electrons*. Acta Crystallographica, **15**(3), 182–186 (1962)

[153] Chabal, Y.J. and Patel, C.K.N. *Molecular hydrogen in a-Si: H*. Rev. Mod. Phys., **59**, 835–844 (1987)

[154] Wu, Y., Stephen, J.T., Han, D.X., Rutland, J.M., Crandall, R.S., and Mahan, A.H. *New hydrogen distribution in a-Si:H: An NMR study*. Phys. Rev. Lett., **77**, 2049–2052 (1996)

[155] Schaefer, H.E., Würschum, R., Schwarz, R.and Slobodin, D., and Wagner, S. *Amorphous hydrogenated silicon studied by positron lifetime spectroscopy*. Applied Physics A, **40**(3), 145–149 (1986)

[156] Suzuki, R., Kobayashi, Y., Mikado, T., Matsuda, A., Mcelheny, P.J., Mashima, S., Ohgaki, H., Chiwaki, M., Yamazaki, T., and Tomimasu, T. *Characterization of hydrogenated amorphous silicon films by a pulsed positron beam*. Japanese Journal of Applied Physics, **30**(10R), 2438 (1991)

[157] Štich, I., Car, R., and Parrinello, M. *Amorphous silicon studied by ab initio molecular dynamics: Preparation, structure, and properties*. Phys. Rev. B, **44**, 11092–11104 (1991)

[158] Barkema, G.T. and Mousseau, N. *Event-based relaxation of continuous disordered systems*. Phys. Rev. Lett., **77**, 4358–4361 (1996)

[159] Klein, P., Urbassek, H.M., and Frauenheim, T. *Tight-binding molecular-dynamics study of a-Si:H: Preparation, structure, and dynamics*. Phys. Rev. B, **60**, 5478–5484 (1999)

[160] de Graff, A.M.R. and Thorpe, M.F. *The static structure factor of amorphous silicon and vitreous silica* (2009). `arXiv:0909.2457`

[161] Mahan, A., Williamson, D., Nelson, B., and Crandall, R. *Small-angle x-ray scattering studies of microvoids in a-SiC:H and a-Si:H*. Solar Cells, **27**(1), 465 – 476 (1989)

[162] Acco, S., Williamson, D.L., Stolk, P.A., Saris, F.W., van den Boogaard, M.J., Sinke, W.C., van der Weg, W.F., Roorda, S., and Zalm, P.C. *Hydrogen solubility and network stability in amorphous silicon*. Phys. Rev. B, **53**, 4415–4427 (1996)

[163] Kikhney, A.G. and Svergun, D.I. *A practical guide to small angle X-ray scattering (SAXS) of flexible and intrinsically disordered proteins*. FEBS Letters, **589**(19PartA), 2570–2577 (2015)

[164] Burger, V.M., Arenas, D.J., and Stultz, C.M. *A structure-free method for quantifying conformational flexibility in proteins*. Scientific reports, **6**, 29040 (2016)

[165] Deschamps, A. and De Geuser, F. *On the validity of simple precipitate size measurements by small-angle scattering in metallic systems*. Journal of Applied Crystallography, **44**(2), 343–352 (2011)

[166] Claudio, T., Stein, N., Stroppa, D.G., Klobes, B., Koza, M.M., Kudejova, P., Petermann, N., Wiggers, H., Schierning, G., and Hermann, R.l.P. *Nanocrystalline silicon: lattice dynamics and enhanced thermoelectric properties*. Phys. Chem. Chem. Phys., **16**, 25701–25709 (2014)

[167] Diaz, J.M.A., Kambara, M., and Yoshida, T. *Detection of Si nanoclusters by X-ray scattering during silicon film deposition by mesoplasma chemical vapor deposition*. Journal of Applied Physics, **104**(1), 013536 (2008)

[168] Leadbetter, A.J., Rashid, A.A.M., Colenutt, N., Wright, A.F., and Knights, J.C. *Nature of the structural heterogeneity in sih films by small angle neutron scattering*. Solid State Communications, **38**(10), 957 – 960 (1981)

[169] Young, D.L., Stradins, P., Xu, Y., Gedvilas, L.M., Iwaniczko, E., Yan, Y., Branz, H.M., Wang., Q., and Williamson, D.L. *Nanostructure evolution in hydrogenated amorphous silicon during hydrogen effusion and crystallization*. Applied Physics Letters, **90**(8), 081923 (2007)

[170] Beyer, W., Lennartz, D., Prunici, P., and Stiebig, H. *Annealing effects of microstructure in thin-film silicon solar cell materials measured by effusion of implanted rare gas atoms*. MRS Proceedings, **1321**, mrss11–1321–a17–14 (2011)

[171] Humphrey, W., Dalke, A., and Schulten, K. *VMD: Visual molecular dynamics*. Journal of Molecular Graphics, **14**(1), 33 – 38 (1996)

[172] Ohdomari, I., Ikeda, M., and Yoshimoto, H. *Annealing behavior of a void network in amorphous silicon*. Physics Letters A, **64**, 253–255 (1977)

[173] Guha, S., Huang, C.Y., and Hudgens, S.J. *Annealing behavior of light-induced defects in hydrogenated amorphous silicon alloys*. Applied Physics Letters, **45**(1), 50–51 (1984)

[174] Luo, Y., Sui, X., He, Y., Huang, H., Zhou, N., and Zhou, L. *The influence of annealing temperature upon the structure of a-Si:H/c-Si thin films*. Journal of Non-Crystalline Solids, **471** (2017)

[175] Luo, Y., Hongyong, G., Zhou, N., Huang, H., and Zhou, L. *Molecular dynamics study about the effect of substrate temperature on a-Si:H structure*. Applied Physics A, **124** (2018)

[176] Deschamps, A. and de Geuser, F. *Quantitative characterization of precipitate microstructures in metallic alloys using small-angle scattering*. Metallurgical and Materials Transactions A, **44**(1), 77–86 (2013)

[177] Paudel, D., Atta-Fynn, R., Drabold, D.A., and Biswas, P. *Effect of low-temperature annealing on the void-induced microstructure in amorphous silicon: A computational study*. arXiv:1808.09119 (2018)

[178] DeWolf, S., Descoeudres, A., Holman, Z., and Ballif, C. *High-efficiency silicon heterojunction solar cells: A review*. Green, **2**(1), 7–24 (2012)

[179] Kanevce, A. and Metzger, W.K. *The role of amorphous silicon and tunneling in heterojunction with intrinsic thin layer (HIT) solar cells*. Journal of Applied Physics, **105**(9), 094507 (2009)

[180] Zeman, M. and Zhang, D. *Heterojunction Silicon Based Solar Cells*, (Springer Berlin Heidelberg2012)

[181] Ge, J., Ling, Z.P., Wong, J., Mueller, T., and Aberle, A.G. *Optimisation of intrinsic a-Si:H passivation layers in crystalline-amorphous silicon heterojunction solar cells*. Energy Procedia, **15**, 107 – 117 (2012)

[182] Fujiwara, H., Kondo, M., and Matsuda, A. *Real-time spectroscopic ellipsometry studies of the nucleation and grain growth processes in microcrystalline silicon thin films*. Phys. Rev. B, **63**, 115306 (2001)

[183] Collins, R., Ferlauto, A., Ferreira, G., Chen, C., Koh, J., Koval, R., Lee, Y., Pearce, J., and Wronski, C. *Evolution of microstructure and phase in amorphous, protocrystalline, and microcrystalline silicon studied by real time spectroscopic ellipsometry*. Solar Energy Materials and Solar Cells, **78**(1), 143 – 180 (2003)

[184] Han, D., Lorentzen, J.D., Weinberg-Wolf, J., McNeil, L.E., and Wang, Q. *Raman study of thin films of amorphous-to-microcrystalline silicon prepared by hot-wire chemical vapor deposition*. Journal of Applied Physics, **94**(5), 2930–2936 (2003)

[185] Macco, B., Melskens, J., Podraza, N., Arts, K., Pugh, C., Thomas, O., and Kessels, W. *Correlating the silicon surface passivation to the nanostructure of low-temperature a-Si:H after rapid thermal annealing*. Journal of Applied Physics, **122**(3), 035302 (2017)

[186] Williamson, D., Jones, S., and Chen, Y. *Small-angle X-ray scattering studies of microvoids in amorphous-silicon-based semiconductors*. NREL/TP-451-6395.UC Category 271. DE94006931, page 6395 (1994). URL `https://digital.library.unt.edu/ark:/67531/metadc619364/`

[187] Serényi, M., Frigeri, C., Szekrényes, Z., Kamarás, K., Nasi, L., Csik, A., and Khánh, N.Q. *On the formation of blisters in annealed hydrogenated a-Si layers*. Nanoscale Research Letters, **8**(1), 84 (2013)

[188] Britton, D.T., Hempel, A., Härting, M., Kögel, G., Sperr, P., Triftshäuser, W., Arendse, C., and Knoesen, D. *Annealing and recrystallization of hydrogenated amorphous silicon*. Phys. Rev. B, **64**, 075403 (2001)

[189] Von Keudell, A. and Abelson, J.R. *Evidence for atomic h insertion into strained Si-Si bonds in the amorphous hydrogenated silicon subsurface from in situ infrared spectroscopy*. Applied Physics Letters, **71**(26), 3832–3834 (1997)

[190] Barber, C.B., Dobkin, D.P., and Huhdanpaa, H. *The quickhull algorithm for convex hulls*. ACM Transactions on Mathematical Software, **22**(4), 469–483 (1996)

[191] Melskens, J., Eijt, S.W.H., Schouten, M., Vullers, A.S., Mannheim, A., Schut, H., Macco, Bart and, M., and Smets, A.H.M. *Migration of Open Volume Deficiencies in Hydrogenated Amorphous Silicon During Annealing*. IEEE Journal of Photovoltaics, **7**(2), 421–429 (2017)

[192] Acco, S., Williamson, D.L., van Sark, W.G.J.H.M., Sinke, W.C., van der Weg, W.F., Polman, A., and Roorda, S. *Nanoclustering of hydrogen in ion-implanted and plasma-grown amorphous silicon*. Phys. Rev. B, **58**(19), 12853–12864 (1998)

[193] Guha, S., Yang, J., Jones, S.J., Chen, Y., and Williamson, D.L. *Effect of microvoids on initial and light-degraded efficiencies of hydrogenated amorphous silicon alloy solar cells*. Applied Physics Letters, **61**(12), 1444–1446 (1992)

[194] Kohn, W. *Density functional and density matrix method scaling linearly with the number of atoms*. Phys. Rev. Lett., **76**, 3168–3171 (1996)

[195] Ehrenreich, H., Seitz, F., and Turnbull, D. *Solid state physics* (1980)

[196] Haydock, R., Heine, V., and Kelly, M.J. *Electronic structure based on the local atomic environment for tight-binding bands. II*. Journal of Physics C: Solid State Physics, **8**(16), 2591–2605 (1975)

[197] Soler, J.M., Artacho, E., Gale, J.D., García, A., Junquera, J., Ordejón, P., and Sánchez-Portal, D. *The SIESTA method for ab initio order-n materials simulation*. Journal of Physics: Condensed Matter, **14**(11), 2745–2779 (2002)

[198] Troullier, N. and Martins, J.L. *Efficient pseudopotentials for plane-wave calculations*. Phys. Rev. B, **43**, 1993–2006 (1991)

[199] Kleinman, L. and Bylander, D.M. *Efficacious form for model pseudopotentials*. Phys. Rev. Lett., **48**, 1425–1428 (1982)

[200] Perdew, J.P. and Zunger, A. *Self-interaction correction to density-functional approximations for many-electron systems*. Phys. Rev. B, **23**, 5048–5079 (1981)

[201] Harris, J. *Simplified method for calculating the energy of weakly interacting fragments*. Phys. Rev. B, **31**, 1770–1779 (1985)

[202] Zaremba, E. *Extremal properties of the harris energy functional*. Journal of Physics: Condensed Matter, **2**(10), 2479–2486 (1990)

[203] Atta-Fynn, R., Biswas, P., Ordejón, P., and Drabold, D.A. *Systematic study of electron localization in an amorphous semiconductor*. Phys. Rev. B, **69**, 085207 (2004)

[204] Fuoss, P.H., Eisenberger, P., Warburton, W.K., and Bienenstock, A. *Application of differential anomalous X-ray scattering to structural studies of amorphous materials*. Phys. Rev. Lett., **46**(23), 1537–1540 (1981)

[205] Thorpe, M.F. and Tichy, L. *Properties and Applications of Amorphous Materials*, (Springer, Netherlands2012)

[206] Elliott, S.R., Zallen, R., and Moorjani, K. *Physics of Amorphous Materials and The Physics of Amorphous Solids*. Physics Today, **40**(8), 69 (2008)

[207] Wadell, H. *Volume, shape, and roundness of quartz particles*. The Journal of Geology, **43**(3), 250–280 (1935)

[208] Beyer, W. *Hydrogen effusion: a probe for surface desorption and diffusion*. Physica B: Condensed Matter, **170**(1), 105 – 114 (1991)

[209] Beyer, W. *Diffusion and evolution of hydrogen in hydrogenated amorphous and microcrystalline silicon*. Solar Energy Materials and Solar Cells, **78**(1), 235 – 267 (2003)